6-9-2016

Enhanced Laminar Convective Heat Transfer using Microstructured Superhydrophobic Surfaces

Andrew Williams

Andrew D. Williams
Candidate

Mechanical Engineering
Department

This dissertation is approved, and it is acceptable in quality and form for publication:

Approved by the Dissertation Committee:

Dr. Peter Vorobieff, Chairperson

Dr. Andrea Mammoli

Dr. C. Randall Truman

Dr. Dimiter Petsev

Dr. Frank van Swol

ENHANCED LAMINAR CONVECTIVE HEAT TRANSFER USING MICROSTRUCTURED SUPERHYDROPHOBIC SURFACES

by

ANDREW D. WILLIAMS

B.S., Mechanical Engineering, Texas A&M University, 2002
M.S., Aerospace Engineering Sciences, University of Colorado at Boulder, 2005

DISSERTATION

Submitted in Partial Fulfillment of the
Requirements for the Degree of

Doctor of Philosophy
Engineering

The University of New Mexico
Albuquerque, New Mexico

May 2016

Dedication

To my wife Gina for her love and support without it this endeavor would have been impossible. Any recognition given me is equally given to her.

To my children AJ and Zoe who joined this adventure in process and have been an eternal source of excitement, joy, and oftentimes a welcome distraction.

"Everything is awesome" – Emmet

Acknowledgements

I would like to acknowledge Dr. Peter Vorobieff, my advisor and dissertation chair, for giving me the freedom to pursue this endeavor at my own pace and for providing support when I needed it. I would also like to thank my committee members from the University of New Mexico for their support and dedication: Drs. Andrea Mammoli, Randy Truman, Dimiter Petsev, and Frank van Swol.

As with most large endeavors, this research was enabled by the help of a wide range of people. Most importantly, I have to thank Mitch Hoesign for his countless hours of support trouble shooting various bugs in the experiment design to get quality data out at the end. I also have to thank Marty Wyse, Mike Sanchez, Lee Underwood, Dr. David Chapman, and Neil Vaughn for their help acquiring and fabricating the test apparatus and test samples, which were the biggest hurdles of this entire project.

I would like to thank all of my friends and colleagues at the Air Force Research Laboratory that provided support and encouragement to me during this undertaking and especially to Dr. Jeremy Banik, Brent Taft, Joy Stein, Dr. Derek Doyle, and Dr. Brandon Arritt for shouldering the workload while I played in the lab. Together we have done some amazing things over the years.

Finally, I would like to thank Mr. Steve Buckley and Dr. Jeff Welsh who mentored me early in my career sharing with me the traits and qualities that a true leader strives for both professionally and personally and for giving me the last shove that started me down this wild ride.

ENHANCED LAMINAR CONVECTIVE HEAT TRANSFER USING MICROTEXTURED SUPERHYDROPHOBIC SURFACES

by

Andrew D. Williams

B.S., Mechanical Engineering, Texas A&M University, 2002
M.S., Aerospace Engineering Sciences, University of Colorado Boulder, 2005
Ph.D., Engineering, University of New Mexico, 2016

Abstract

For many centuries, researchers have investigated the complex interactions between a solid surface and a fluid in motion relative to the surface. For many cases, the classical no slip boundary condition holds true. However, there are a subset of situations where this assumption is not valid, and slip between the surface and fluid must be considered. One such example is a micropatterned, superhydrophobic surface, which has been shown to enable slip resulting in a decrease in drag and pressure loss for both laminar and turbulent flow. The hydrodynamic effects of these surfaces have been studied in depth, but the effects on heat transfer are largely unknown. The primary goal of this research effort was to explore the effects of slip flow on laminar convective heat transfer resulting from micropatterned, superhydrophobic surfaces.

The first step toward achieving the research goal was to develop a model to study first order effects, predict the effect of slip flow on heat transfer, and design the experimental setup. The general momentum equation for Poiseuille flow was solved using modified

boundary conditions consistent with slip flow, and the resulting velocity profile was input into the thermal balance equation which was numerically solved. The model assumed hydrodynamic slip but not thermal slip nor a temperature jump at the boundary, and as a result, it predicted a net increase in heat transfer performance.

For the experimental portion of the study, laminar Poiseuille flow in a parallel plate configuration with a constant temperature boundary condition at 273 K using an ice bath was studied. Four sets of copper sample plates measuring 15 cm by 3.8 cm were fabricated with different surface condition: 1) uncoated smooth, 2) hydrophobic coated smooth, 3) uncoated micropatterned, and 4) hydrophobic coated micropatterned. The micropattern was a laser machined array of 25 μm x 25 μm microridges oriented in the streamwise direction. Contact angle measurements were made on all of the test samples to ensure the coated plates were hydrophobic and the uncoated plates were not.

From the experimental results, several observations and conclusions were made. First, only the micropatterned, superhydrophobic coated sample achieved a slip state with an average slip length of 0.3 mm. Second, hydrodynamic slip was observed without the accompaniment of thermal slip since the heat transfer performance for the superhydrophobic sample was as good as or better than the baseline sample for all flow rates tested. Finally, it was concluded that micropatterned superhydrophobic surfaces reduce pressure loss and improve heat transfer as seen by the improved efficiency factor, which is the ratio between the Nusselt number and the friction loss.

Contents

List of Figures

List of Tables

Glossary

Glossary

A_H	=	Hamaker constant
A_w	=	wetted area
a	=	contact area of a droplet on a surface
C	=	integration constant
C'	=	Lennard-Jones potential coefficient
c	=	specific heat capacity
D	=	diffusion coefficient
d	=	diameter
E	=	interfacial energy
F	=	efficiency factor
f	=	force
f	=	friction factor
g	=	gravity acceleration
H	=	channel height
h	=	feature height
$\bar{h}$	=	average convective heat transfer coefficient
K	=	non-dimensional surface slip behavior
k	=	thermal conductivity
k_B	=	Boltzman's constant
Kn	=	Knudsen number
l	=	length
M	=	number of x nodes
m	=	mass
Nu	=	number of y nodes
Nu	=	Nusselt number
P	=	pressure

Pe	=	Peclet number
Pr	=	Prandtl number
p	=	perimeter
p_{DC}	=	percentage of diffusive collisions
q	=	distance between features
R	=	radius of curvature
r	=	radius
r_s	=	surface roughness
Re	=	Reynolds number
s	=	feature pitch
St	=	structure factor of first molecular layer
T	=	temperature
t	=	thickness
t	=	time
u	=	velocity
V	=	volume
w	=	width
x	=	streamwise direction
y	=	surface normal direction

Greek

α	=	angle at which droplet will move
α_0	=	dimensionless geometrical parameter of order one
β	=	sliding coefficient
ϕ	=	composite surface solid fraction
γ	=	surface tension
$\dot{\gamma}$	=	shear rate
κ	=	capillary length
λ	=	slip length
$\bar{\lambda}$	=	dimensionless slip length
μ	=	dynamic viscosity

θ	=	contact angle
ρ	=	density
σ	=	molecular length scale
σ_m	=	tangential accommodation coefficient
τ	=	wall shear stress
ψ	=	thermal-hydrodynamic efficiency ratio

Subscripts

0	=	bulk
a	=	advancing
C	=	critical
c	=	contact line
CB	=	Cassie-Baxter
E	=	equilibrium
fd	=	fully developed
g	=	gas
H	=	hydraulic
L	=	length
l	=	liquid
lam	=	laminar
LV	=	liquid-vapor
m	=	mean
mol	=	molecular
NS	=	no slip
p	=	constant pressure
r	=	receding
S	=	surface
s	=	slip
SL	=	solid-liquid
SV	=	solid-vapor
T	=	temperature

th	=	thermal
W	=	Wenzel
w	=	wall
x	=	x-direction
Y	=	Young's
y	=	y-direction

Symbols

*	=	apparent
—	=	average
||	=	collective

Abbreviations

1-HDT	=	1-hexadecanethiol
ADSA	=	axisymmetric drop shape analysis
CAH	=	contact angle hysteresis
CNT	=	carbon nanotube
DI	=	deionized
LIF	=	laser induced fluorescence
MSDS	=	material safety data sheet
NSBC	=	no-slip boundary condition
PDMS	=	polydimethylsiloxane
PIV	=	particle image velocimetry
PTFE	=	polytetrafluoroethylene
SEM	=	scanning electron microscope
TIFA	=	theoretical image fitting analysis

Chapter 1

Introduction

1.1 Motivation

As components and systems continue to shrink in size and volume, the ability to control fluid dynamics and heat transfer at smaller and smaller scales becomes increasingly important. Small and microscale systems are rapidly proliferating into many sectors including telecommunications, medical, energy, automotive, and aerospace addressing critical applications such as cooling computer processors, servers, power amplifiers, and RF systems; lab on a chip for biological and medical testing; and additive manufacturing. The ability to understand and control fluid and thermal effects at milli-, micro-, and nanoscale lengths is becoming increasingly important.

Recent developments in microfabrication techniques, nanotechnology, and surface chemistry have provided scientists and engineers with the ability to manipulate and control solid, fluid, and vapor interactions at two- and three-phase interfaces. Surfaces can be tuned for various surface characteristics ranging from fully wetting to

superhydrophobic using microscale surface patterning, nanoscale roughness, and specially tailored chemical surface treatments [1], [2]. These new surfaces provide engineers the ability to control many parameters to dial in specific traits of the surface, including low drag, stain-free, self-cleaning, anti-icing, anti-dew, heat transfer enhancing, and advanced wicking [3]. The design of many of these surfaces mimics natural biological systems such as the leaves on the lotus plant or the legs of a water strider [4], [5], [6], [7], [8], [9], [10], [11], [12], [13], [14], [15], [16], [17], [18], [19], [20]. Of specific interest in the research community are superhydrophobic surfaces and their effects on drag, boiling, condensation, evaporation, and single-phase convection.

Many researchers have explored a wide array of potential applications for super-hydrophobic surfaces and have shown modest improvements in drag reduction in fluid channels, over hydrofoils, and around ship hulls for laminar flow and significant improvement as high as 60% for turbulent flow [21], [22], [23] [24], [25] [26] [27] [28] [29] [30] [31] [32], [33], [34], [35], [36], [37], [38], [39]. In addition, there have been a number of efforts that have investigated the boiling, dropwise condensation, and evaporation performance of these surfaces, and many researchers have demonstrated system level improvements across the board for these cases [40], [41], [42], [43], [44], [45], [46], [47], [48], [49], [50], [51], [52], [53], [54], [55], [56]. Some researchers have used superhydrophobic surfaces in combination with superhydrophilic surfaces to create one-way heat transfer devices where liquid evaporates on the hydrophilic surface, condenses on the hydrophobic surface, and is then propelled, or jumps, from the hydrophobic

surface to the hydrophilic surface because of the energy difference between the two surfaces [57], [58]. Heat transfer does not occur in the opposite direction because a drop that condenses on the hydrophilic surface will not jump to the hydrophobic surface. The ability for engineers to design and control surface structures and properties provides a wealth of potential uses and applications that are beginning to be explored.

1.2 Research Goals and Objectives

There is a large body of work investigating the role and effects of superhydrophobic surfaces in heat transfer applications, but single-phase internal flow has received limited attention from the research community. When this project was originally started, there was one conference paper that discussed the potential for heat transfer enhancement of superhydrophobic surfaces for a constant flux boundary condition [59]. Since the initiation of this project, there have been many subsequent papers that analytically and numerically explored the topic for surfaces with longitudinal ridges, transverse ridges, pillars, and holes [60], [61], [62], [63], [64], [65], [66], [67]. However, there have been no studies that have reported experimental results for superhydrophobic surfaces.

The overall goal of this work was to explore and develop a greater understanding of heat transfer effects from micropatterned, superhydrophobic surfaces for laminar internal flow and to improve understanding of the effects of hydrodynamic slip and potentially thermal slip at the three-phase interface boundary for relevant heat transfer surfaces. This goal can be broken down into three major objectives

Objective 1: Develop and fabricate micro-patterned superhydrophobic surfaces using copper, aluminum, or other relevant heat transfer surfaces

One of the first challenges that had to be considered was fabricating the micro-patterned surface texture using a method and form factor suitable for experimental study. For synthetic hydrophobic surfaces, the wetting states are fairly well known [68], [2], [69], [70], [71], [72], [73], [74]. For surfaces with microscale roughness, droplets will either rest on top of the surface texture in the highly mobile Cassie state, or the droplet will fully penetrate into the receded parts of the surface and will pin to the surface in the Wenzel state [75], [76], [77], [78]. However, the key to superhydrophobicity in biological systems is two-tier surface roughness at the micro- and nanoscales. Achieving this multi-scale roughness can be challenging in a form factor that lends itself to experimental testing. Macroscale testing is easier to instrument but requires larger samples to be fabricated which limits possible fabrication techniques; whereas, microscale testing allows for smaller samples and more fabrication techniques, but creates significant challenges for instrumentation and measurements. In addition, while some microfluidic applications might benefit from microscale implementation, the greater challenge is to achieve a noticeable effect on the macroscale. The trade-off between these issues was a major challenge for the research project.

One of the specific goals for this research effort was to explore materials and concepts that would be relevant to a real-world application upon successful completion. This

objective greatly reduced the number of potential substrate options and created multiple challenges fabricating test substrates. Copper and aluminum are two of the most used materials for thermal systems because of their high thermal conductivity, but their use for superhydrophobic surfaces presented two major challenges: 1) fabricating microscale patterns with nanoscale roughness and 2) achieving good adhesion between the hydrophobic coating and the substrate. Understanding the interplay of these issues and finding workable solutions was a major part of this research effort.

Objective 2: Investigate the effect of hydrophobicity and superhydrophobicity on friction loss and heat transfer performance for laminar flow

There were two key parts to this objective. The first was to fully characterize the critical parameters for the hydrophobic and superhydrophobic surfaces. Many researchers have investigated the general properties of hydrophobic surfaces such as surface wetting and contact angle, but few measure and report key environmental parameters such as temperature and humidity and contact angle hysteresis [79], [57], [80], [81], [82], [83], [84], [85], [86]. The contact angle on copper substrates is highly sensitive to temperature with values ranging from 9° to 70° for temperatures ranging from 20 to 100 °C [87]. An effort was made during this project to measure and report the environmental parameters during these measurements such as ambient temperature and relative humidity.

The second was to experimentally measure the friction loss and heat transfer effects of the hydrophobic and superhydrophobic samples compared to uncoated and un-patterned surfaces. As noted previously, this was especially challenging because of the trade-off of measuring what are likely micro- and nanoscale impacts at macroscale levels that are more easily instrumented and measured. Since the initiation of this project, there has been a large body of work to analytically and numerically predict the behavior for slip at the wall caused either by pure slip or caused specifically by patterned superhydrophobic surfaces. Very few efforts have attempted to experimentally measure the heat transfer effects; most experimental studies have focused solely on drag effects. This objective was an effort to gain experimental insight into thermal effects.

Objective 3: Determine and calculate hydrodynamic and thermal slip on a superhydrophobic surface and compare that to existing analytical and numerical models

Using the pressure loss and heat transfer results from the experimental measurements, hydrodynamic slip and thermal slip lengths were calculated at the boundary for the various hydrophobic and superhydrophobic surfaces through and indirect method that compared the measured values to those of the uncoated, smooth surface. Since it is very challenging to directly measure these effects without interfering with the flow, indirect measurements were used. These results were then compared to

existing predictive models to help determine and quantify the hydrodynamic and thermal slip lengths.

1.3 Organization

Chapter 2 provides background information discussing the slip boundary condition, factors that affect slip with a more in-depth discussion of surface wettability, and finally a review of hydrophobic and superhydrophobic surface concepts. Key characteristics of superhydrophobic surfaces such as contact angles, wetting states, and surface structures are introduced, and important surface patterning characteristics are assimilated and reported for achieving superhydrophobicity. Chapter 3 is a literature review that summarizes and discusses the results by other authors for drag reduction in both laminar and turbulent flow regimes, as well as the multiple analytical and numerical studies exploring the thermal effects of slip caused by superhydrophobic surfaces. These models will be compared to the experimental data in Chapter 7.

Chapter 4 presents a thermal model that predicts thermal performance based purely on a hydrodynamic slip boundary condition at the wall using a Crank-Nicolson numerical modeling approach [88]. It does not account for the possibility of thermal slip, nor does it consider interface heat transfer resistance effects caused by the micro-patterned, superhydrophobic surface. It was primarily used for first-order analysis to understand the potential effects and to help design the experimental apparatus to maximize the measured temperature difference between slip and no-slip boundary conditions. The

paper describing these findings was presented at the 2012 AIAA Aerospace Sciences Conference [89]. However, the last section does introduce new material developed after the presentation of the material at the conference.

Chapters 5, 6, and 7 present the experimental work. Chapter 5 describes the sample fabrication techniques for the five different sample cases that were developed and tested and the microfabrication technique developed and tested in conjunction with the hydrophobic coating. Hydraulic and thermal testing was only conducted on one coating because of adhesion issues with the other coating. In Chapter 6, a discussion of contact angle and contact angle hysteresis measurement techniques is presented along with the results and example images for each of the surfaces. The ambient temperature and relative humidity are also presented for each of the measurements. Chapter 7 describes the experimental setup for the hydraulic and thermal testing, the results for each of the samples tested, and a comparison to the control sample as well as to the model predictions from the literature review in Chapter 3. Estimates for the hydraulic and thermal slip are also provided. Finally, Chapter 8 contains concluding remarks and suggestions for future work.

Chapter 2

Slip Boundary Condition Background

Until recently, virtually all undergraduate engineering students and most professional engineers accepted that the only boundary condition realized for fluid flow over a solid surface was no-slip. Accordingly, the fluid must have zero relative velocity to the boundary at the solid-liquid interface for Newtonian, macroscale flow. The no-slip boundary condition manifests because of the force imbalance between the adhesion force at the surface-liquid interface and the cohesion force at the liquid-liquid interface. For most fluids and scenarios, the adhesion force is greater than the cohesion force thereby resulting in a zero relative motion at the solid-liquid interface, and generally, this assumption provides adequate accuracy for the significant simplicity it provides to many modern day calculations. However, as technology continues to shrink in size and engineers improve technology to observe and control materials at smaller and smaller length scales, understanding the physical effects at small length scales becomes increasingly important.

The no-slip boundary condition has generally gained acceptance amongst scientist and engineers. However, this was not always the case, and the solid-liquid interface behavior was a highly debated topic during the 18th and 19th century. A review of the history of this discussion was provided by Goldstein [90]. The no-slip boundary condition was first proposed by Daniel Bernoulli in 1738 [91] to account for errors between his calculations for a perfect fluid and experimental results. In the 19th century, three hypotheses were put forward: 1) Coulomb stated that the fluid velocity at the boundary of a solid is the same as that of the solid and changes continuously in the fluid, 2) Girard believed that there was a stagnant layer between the solid and the bulk fluid and that at the interface between the stagnant layer and the bulk fluid slip occurred, and 3) Navier believed that slip occurs at the boundary and that slip is resisted by a force proportional to the relative velocity. Using his equations of motion for a viscous fluid, he deduced that the boundary condition should be:

$$u_s = \lambda \frac{\partial u_x}{\partial y} \tag{2-1}$$

where, u_s is the slip velocity, λ is the slip length, u_x is the fluid velocity in the primary flow direction, and the differentiation with respect to the y-direction, which is normal to the wall. If the slip length is zero, then Equation 2-1 reduces to the no-slip boundary condition. Figure 2-1 shows depictions of the no-slip and slip boundary conditions described by Equation 2-1.

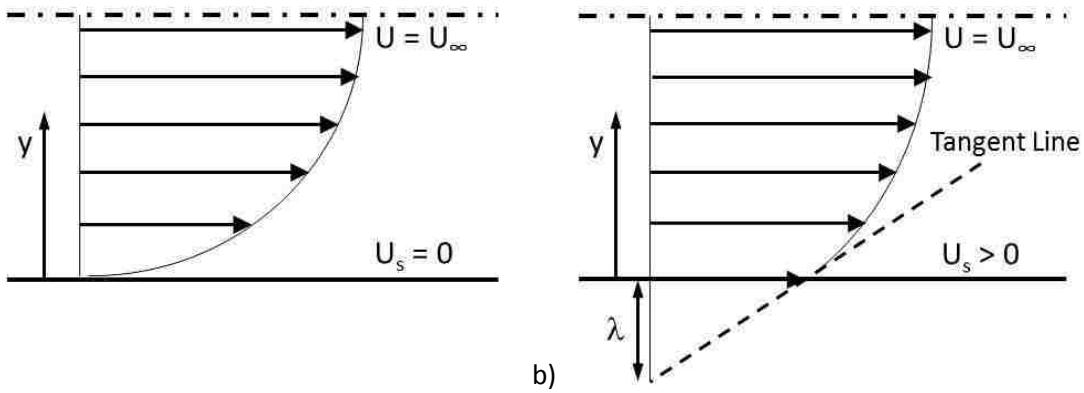

Figure 2-1: Depiction of the a) no-slip and b) slip boundary conditions defined by Equation 2-1

Over many years the boundary condition at the solid-liquid interface was discussed by many of the great historical names in science and engineering: Poisson, Poiseuille, Darcy, Helmholtz, Maxwell, and Stokes. Poiseuille noted that the velocity of blood in a tube decreases from a maximum at the center to a small value at the walls while Maxwell was the first to predict and quantify the slip length as being on the order of the mean free path of the fluid [b=O(1 nm)], but it was the hypothesis suggested by Stokes that would gain acceptance. Stokes suggested that there is no-slip at the boundary and that properties in the fluid are uniform. Ultimately, the Stokes's hypothesis for the no-slip boundary condition was accepted in part because it could not be disproven by measurement devices of the time.

Only many decades later experimental techniques advanced far enough to observe and probe the solid-liquid boundary phenomena with sufficient accuracy to answer the question. In 1952, Tolstoi [92] proved Maxwell's theory that slip length is on the order of the mean free path of the fluid, and then Blake in 1990 [93] validated this theory [94]. In

1956, Schnell [95] produced the first experimental evidence suggesting that slip occurs at the solid-liquid interface by measuring the flow rate of water in glass capillaries treated to be hydrophobic. Finally, Thompson and Troian [96] were the first to demonstrate that surface hydrophobicity can produce slip lengths larger than the mean free path using molecular dynamic simulations. Today understanding and controlling the solid-liquid boundary condition using superhydrophobic surfaces is still an area of active investigation. Ultimately, over time, Navier's hypothesis that slip occurs at the interface has been shown to be correct and that Bernoulli's no-slip boundary condition is an acceptable approximation without loss of accuracy for most cases.

2.1 Slip Boundary Condition

The designation of a slip boundary condition is a broad and general term that encompasses a wide range of physical phenomena and effects and refers to any situation in fluid dynamics where the tangential velocity component immediately in contact with the solid surface is non-zero. Slip is further categorized and defined dependent on the context and mechanism for slip. Molecular, or intrinsic, slip refers to using hydrodynamics to force molecular slip using large forces [97]. Molecular slip will occur when the intermolecular interactions are balanced by the viscous forces such that:

$$\mu\sigma^2\dot{\gamma} \approx \frac{A_H}{\sigma} \tag{2-2}$$

where, μ is the viscosity of the liquid, σ is the molecular length scale, $\dot{\gamma}$ is the shear rate, and A_H is the Hamaker constant for intermolecular forces. Using water as an example where viscosity is 10^{-3} Pa-s and typical values of the Hamaker constant of 10^{-19} J and molecular length scale of 0.3 nm, results in a shear rate on the order 10^{12} s^{-1} [94].

Two examples where molecular slip occurs are gas flow and contact line motion. For gas flow, devices with dimensions on the order of the mean free path of the gas have shown significant slip [98]. Maxwell first introduced the possibility of gas slip by considering that some wall collisions were specular and some were diffusive which allows the exchange of momentum between the gas and wall with a slip length given in Equation (2-3) [94]:

$$\lambda\left(\sqrt{2}\pi\sigma^2\rho_g\right) = \frac{2(2-p_{DC})}{3p_{DC}} \tag{2-3}$$

where, ρ is the gas density and p_{DC} is the fraction of diffusive collisions. Generally, the Knudsen number, defined as the ratio between the mean free path and the system size, is used to characterize the boundary condition for gas flow with slip being important when the Knudsen number is greater than 0.1 [99]. The second example for molecular slip is contact line motion, for which molecular slip was used to remove singularities in the motion of the contact lines and were reviewed by de Gennes [100] and Dussan [101].

Apparent slip occurs when the no-slip condition holds at very small length scales, but it appears that the no-slip condition is invalid at large length scales. Examples of apparent

slip include flows of non-Newtonian flows such as polymer solutions, electrokinetics, acoustic streaming, and liquid flowing over a gas layer. Apparent slip occurs when there is a steeper velocity gradient closer to the surface than in the bulk fluid, which translates to the perception of a slip length. This can be caused by density, viscosity, or other changes in the boundary layer near the surface. The apparent slip region can be very thin as noted by de Gennes who observed slip effects are explainable by a gas layer only 1 or 2 atoms thick [102].

Finally, effective slip is defined as estimating the molecular or apparent slip by averaging an appropriate measurement of the length scale of the experiment, device, or system [94]. Effective slip is the calculated or estimated Navier-like slip using macroscale measurements, techniques, or approaches. Effective slip does not capture the actual surface interaction phenomenology or boundary condition behavior, but rather provides an approximation of the boundary condition and boundary layer effect on the macroscale based on an equivalent no-slip boundary condition. The utility of effective slip is in its commonality for reporting and comparing results in the literature.

Over the last few decades, investigating slip phenomenology has been an active and growing area of research. With advances in precision measurement equipment, advanced testing techniques, nano- and microscale material tailoring, and molecular dynamic simulations, researchers have been able to probe the solid-liquid interface under a wide range of conditions in an attempt to better understand slip phenomenology. There

have been numerous studies indirectly and directly measuring slip under a wide range of conditions.

Indirect studies assume that the velocity tangent to the surface is proportional to the shear rate at the surface. Most approaches compare measurements taken for slip behavior to no-slip control conditions. For example, one approach is to measure pressure drop versus flow rate such that a constant pressure differential is established for various test conditions and the resulting flow rate is measured. Under these conditions, slip flow will provide higher flow rates for a set pressure differential than no-slip flow [94]. The inverse approach where flow rate is maintained as a constant and the pressure head losses caused by the slip or no-slip condition are measured has also been used [33]. Other indirect measurement approaches include measuring drainage versus viscous force using either a surface force apparatus [103], [104], [105], [106] or an atomic force microscope [107], [108], sedimentation speed under gravity [109], and streaming potential using an electrolyte solution [110]. The drawback with all of these approaches is that they measure the effective slip and do not directly measure local slip at the boundary.

Direct measurement techniques unlike indirect approaches attempt to directly measure the local slip at the boundary usually through tracer particles or fluorescent probes. Particle image velocimetry uses an optical system to measure the velocity profile of passive tracer particles in either Couette or Poiseuille flow and compare the particle velocity profile to the ideal flow condition [34], [36], [111], [112], [113]. The flow profile

is also used to determine the flow velocity at the surface. Approaches using fluorescent probes include near-field laser velocimetry fluorescent recovery [114], [115], [116] and fluorescence cross-correlation [117] and are generally only effective on very small length scales on the order of 1 μm. While these techniques attempt to observe and directly measure the local velocity field at the boundary, the addition of measurement particles to the flow impacts flow dynamics and must be carefully designed and analyzed to eliminate external contributions. Lauga, Brenner, and Stone [94] provide a detailed discussion of the various indirect and direct measurement approaches as well as detailed tables summarizing the experimental approaches and results from the literature for each technique.

2.2 Factors Affecting Slip

Because of the high interest for understanding slip boundary conditions for diverse applications including polymer processing, gas dynamics, drag reduction, and micro-fluidics, there is a large amount of existing research investigating the various physical parameters that affect slip. The following sections will summarize the existing literature for each parameter.

2.2.1 Shear Rate

Navier's hypothesis, which remains the primary means to define and characterize slip at the boundary, assumes a constant slip length. However, molecular dynamic simulations and experimental evidence indicate that slip is rate dependent and that there

is a critical shear rate that must be satisfied before slip can occur [118], [119], [120]. Zhu and Granick [105] indirectly studied rate dependent slip of highly wetting Newtonian fluids on molecularly smooth surfaces for three different fluid-solid configurations by measuring the hydrodynamic forces and found that 1) after a critical shear rate was reached the hydrodynamic force reduced two to four orders of magnitude less than predicted by no-slip and 2) slip increased with contact angle. They followed this study by investigating the limits of the no-slip boundary condition and the effects of intermolecular interactions and surface roughness. The advancing and receding contact angles that they studied ranged between 12° and 121° and surface roughness between 0.5 and 6 nm. They observed that the critical shear stress and shear rate for deviation from no-slip predictions increased nearly exponentially with increasing roughness and diverged at 6 nm rms roughness. They concluded that intermolecular interactions dominated for smooth surfaces and surface roughness dominated for all other cases [106].

Thompson and Troian [96] first predicted the concept of critical shear rate for slip through their molecular dynamic simulations. Using molecular dynamic simulations of a Leonard-Jones fluid, Ngayama and Cheng [121] identified the importance of surface wettability in determining interfacial hydrodynamic resistance which resulted in lower interfacial resistance for hydrophobic surfaces and a plug flow velocity profile shape. They also predicted that the boundary condition is determined by the relationship between the interfacial resistance (surface wettability) and the external driving force (shear rate) with slip occurring when the external driving force overcomes the interfacial resistance. Using

a similar approach, Priezjev and Troian [122] predicted that for a weak solid-fluid interaction the slip length increases non-linearly with shear rate following a power law function; whereas, a strong solid-fluid interaction led to a linear rate-dependence of the slip length. Experimental results by Wu and Cheng [123], Zhu and Granick [106], and Choi et al. [21] support the idea of a critical shear rate required for slip to occur on a surface with values ranging from 10,000 to 50,000 1/s.

2.2.2 Gas Layer

Slip has been observed experimentally to depend on the type and quantity of dissolved gas, and the existence of a gas layer has been attributed to the most likely reason for apparent slip to occur. It was reported in sedimentation studies that slip only occurred when the liquid sample was in contact with air and that the no-slip condition held under vacuum conditions [124]. Slip results in non-wetting systems have been found to depend strongly on the fluid, solid, contamination, and the ambient environment under which the experimental procedures were performed. For very clean, smooth hydrophobic surfaces boundary slip on the order of 20 nm was measured, which was in good agreement with theory and numerical simulations for smooth non-wetting surfaces [125]. Cottin et al. [125] also noted that the very large slip lengths reported in the literature were likely caused by nanoscale hydrophobic contamination particles that "act as nucleation sites for vapor bubbles," which they claim is supported by the results of Tretheway et al. [126] and the change in Cottin et al.'s results testing hydrophobic coatings in a clean room environment compared to an ambient lab environment. This

claim was also supported by the reporting of Lin and Granick [127] who reported the presence of platinum nanoparticles on the smooth mica surfaces tested by Zhu and Granick [106].

The concept of a gas layer was first mentioned by Ruckenstein and Rajora [128] and detailed theoretical consideration has shown it is a favorable condition for water between two hydrophobic surfaces to vaporize forming a gas layer [129]. The boundary condition requirements for a liquid-vapor interface are very different from a solid-liquid interface and requires the stress to be continuous at the liquid-vapor interface, thereby leading to apparent slip. The apparent slip length for a vapor-water interface can be found using:

$$\frac{\lambda}{H} = \frac{\mu_{water}}{\mu_{vapor}} - 1 \tag{2-4}$$

For a vapor-water interface, the viscosity ratio is on the order of 50. The actual vapor formation at the surface is important because a vapor layer behaves differently from vapor bubbles [94]:

1. The gas in bubbles recirculates, which decreases the previous estimate for slip length by a factor of four.
2. The no-slip region located between the bubbles will significantly decrease the apparent slip lengths.
3. Bubbles in general are not flat, which decreases the slip length further with an effect similar to roughness on a shear flow.

When the gas layer is in the Knudsen regime, the shear stress in the liquid is balanced by a thermal stress in the gas which leads to an apparent slip length given by:

$$\lambda \sim \frac{\mu}{\rho_g u_{th}} \tag{2-5}$$

where u_{th} is the thermal velocity, is independent of the height, and can be at the micronscale [94]. The concept of using a gas layer to create apparent slip has been exploited extensively in the use of superhydrophobic surfaces in the Cassie state to drastically reduce drag in laminar and turbulent flow as shown in Figure 2-2. The concepts of superhydrophobicity, wetting states, and drag reduction in slip flow will be discussed further in Section 2.3 and 2.4 and in Chapter 3.

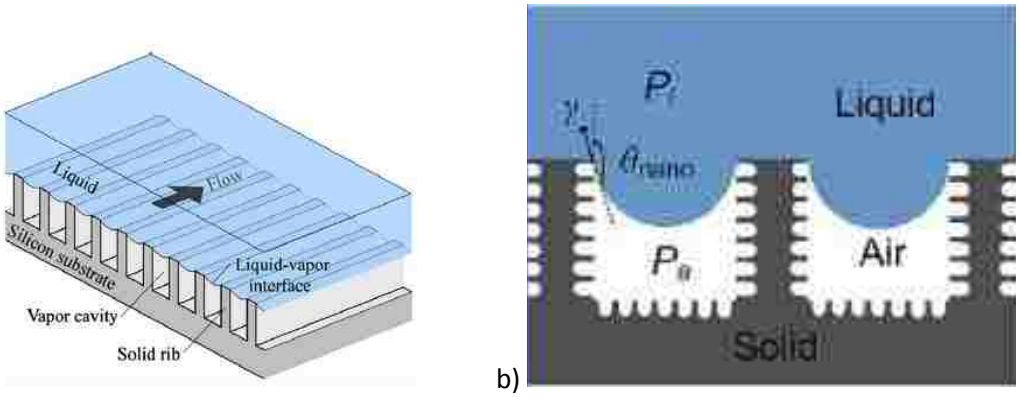

Figure 2-2: a) Fluid flow over a superhydrophobic surface and the three-phase (solid-liquid-vapor) interfaces [130] b) schematic of microfeatures with nanoscale roughness to enhance the gas fraction before wetting occurs [28].

2.2.3 Pressure

The effect of pressure on slip is largely tied to the previous section and the concept of a gas gap providing the means for slip to occur at the interface. The PIV experiments of

Tretheway, Stone, and Meinhart [126] found the measured slip length decreased with increases in absolute pressure, and for water, the no-slip boundary condition held above 6 atm. The effect of pressure gradients on slip was discussed by Ruckenstein and Rajora [128]. Based on equilibrium thermodynamics, they proposed that the chemical potential of a liquid molecule depends on pressure, and a pressure gradient leads to a chemical potential with a net force on the liquid and a net surface velocity with a slip length on the order of:

$$\lambda \sim \frac{\mu D_S}{\rho_{mol} D_H k_B T} \tag{2-6}$$

where μ is the viscosity, D_S is the diffusion coefficient of the molecules close to the surface, ρ_{mol} is the molecule density, D_H is the hydraulic diameter, k_B is Boltzman's constant, and T is temperature. For water, the results for the above equation lead to molecular size slip lengths and indicate that for large slip lengths, slip over a gas gap is required [94].

2.2.4 Surface Roughness

The influence of surface roughness on slip is still heavily debated and is not purely an independent variable but is strongly tied to surface wettability and other surface effects. Molecular size, larger scale roughness, and geometrical features influence behavior at the solid-liquid interface by creating ambiguity to the exact location of the surface, thereby impacting the dynamics of the nearby fluid leading to both increasing and decreasing friction with roughness depending on the situation [94]. From a physical perspective the

idea of roughness decreasing slip is straightforward in that on the roughness inhibits flow and dissipates mechanical energy that resists motion [94]. However, surface roughness also greatly impacts the wettability and the contact angle of the solid-liquid-vapor interactions and is not easily decoupled from these effects.

2.2.5 Wetting

Early researchers recognized that friction at the solid-liquid boundary should be a function of the physiochemical nature of both the solid and the liquid and that wetting properties should play and important role [90]. Wetting effects between solids and liquid are reviewed extensively by de Gennes [100], [131] and are quantified by the spreading coefficient, $S = \gamma_S - \gamma_L - \gamma_{LS}$, which is the difference between the solid, liquid, and combined liquid-solid interfacial energies [94]. When S is positive, the solid is completely wetted by the liquid, and when S is negative the solid is partially wetted with a small droplet taking the shape of a spherical cap. Slip has been measured in systems in complete wetting and partial wetting, and slip has usually been found to increase with contact angle. Lauga et al. [94] summarized and provided a number of references regarding wetting studies on slip.

For the case of molecular or intrinsic slip, Tolstoi [92] was the first to try to capture slip at the molecular level using concepts from thermodynamics to relate surface energy and molecular mobility. In the case of complete wetting, the Tolstoi [92] model leads to the no-slip boundary condition within the scope of Maxwell's theory of the mean free

path of the fluid, but in the case of partial wetting, molecules near the surface have larger mobility leading to a slip length on the order of [94]:

$$\frac{\lambda}{\sigma} \sim exp\left(\frac{\alpha_0 \sigma^2 \gamma_L (1 - \cos\theta_E)}{k_B T}\right) - 1 \tag{2-7}$$

where α is a dimensionless geometrical parameter of order one and θ_E is the equilibrium contact angle. Based on the model, slip increases with increasing contact angle and can be orders of magnitude larger than the molecular length scale.

An alternative theory put forward by Barrat and Bocquet [132], uses the fluctuation-dissipation theorem and Green-Kubo relations to derive slip length from equilibrium thermodynamics and Onsager's hypothesis of linear regression fluctuations, which leads to slip length on the order of [94]:

$$\frac{\lambda}{\sigma} \sim \frac{D_{\|}}{D_O St C'_{SL} \rho_{ms} \sigma^3} \tag{2-8}$$

where $D_{\|}$ is the collective molecular diffusion coefficient, D_O is the bulk diffusivity, St is the structure factor for the first molecular layer, ρ_{ms} is the fluid density at the first molecular layer at the surface, and C'_{LS} is the dimensionless solid-liquid coefficient of the Lennard-Jones potential. For the case of complete wetting the slip length is essentially zero, but in non-wetting cases the slip length can be up to two orders of magnitude above the molecular size and increases with contact angle. Theoretical predictions were found to agree well with molecular dynamic simulations and experiments with polymer

solutions [94]. Because of the importance of surface wettability on slip, this topic is reviewed in greater depth in the following section.

2.3 Surface Wettability

As discussed in the previous section, surface wetting is believed to play an important role in slip, but the role it plays is unclear since slip has been observed for both partially wetted and fully wetted interfaces. It is clear that wettability is an important factor because it controls how liquids interact with solid surfaces. As a result, understanding the factors that impact wettability is an important step to understanding liquid-solid interface behavior during flow.

2.3.1 Young's Contact Angle

Wettability is simply the extent to which a liquid droplet will spread or recede on a solid surface and is the equilibrium state that balances surface tension forces within the droplet, surface tension forces within the surrounding vapor, surface energy forces for the solid surface, and external deforming forces such as gravity. The resulting state can be quantified by the contact angle the droplet makes with the solid surface and is defined as the angle formed by the intersection of the liquid-solid interface and the liquid-vapor interface geometrically acquired by applying a tangent line from the contact point along the liquid-vapor interface in the droplet profile [133]. A contact angle less than 90° indicates that wetting of the surface is favorable and will spread over a large area. Surface exhibiting this tendency are classified as hydrophilic, and those that approach contact

angles of 0° are considered superhydrophilic or fully wetting. When contact angles are greater than 90°, surface wetting is unfavorable and the liquid will minimize its contact with the surface and form a compact liquid droplet. Surfaces exhibiting this tendency are classified as hydrophobic, and surfaces with contact angles exceeding 150° are considered superhydrophobic. Ultimately, the state of the system is dependent on the interface where solid, liquid, and vapor co-exist in equilibrium, which is referred to as the three-phase contact line. Theoretically, the contact angle is a characteristic for a given solid-liquid system in a specific environment [134].

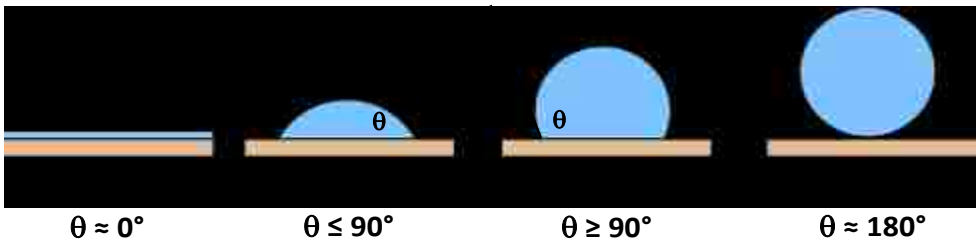

Figure 2-3: Illustration of the contact angle formed by a liquid drop on a smooth, homogeneous solid surface ranging from total wetting with an approximate contact angle of 0° to no wetting with an approximate contact angle for 180°[1].

It was Thomas Young in 1805 [135] that determined that the spreading or receding of a liquid drop placed on a smooth surface was controlled by the net force per unit length of the solid-liquid (γ_{SL}), solid-vapor (γ_{SV}), and liquid-vapor (γ_{LV}) surface tensions acting on the contact line. The drop will reach equilibrium when it reaches the point where the sum of the horizontal components of the surface tension equal zero:

[1] By PMarmottant (Own work) [CC BY-SA 3.0 (http://creativecommons.org/licenses/by-sa/3.0) or GFDL (http://www.gnu.org/copyleft/fdl.html)], via Wikimedia Commons

$$\gamma_{LV} \cos\theta_\gamma + \gamma_{SL} - \gamma_{SV} = 0 \quad (2\text{-}9)$$

Solving for the contact angle, θ_γ, yields what is known as Young's equation:

$$\cos\theta_\gamma = \frac{\gamma_{SL} - \gamma_{SV}}{\gamma_{LV}} \quad (2\text{-}10)$$

Surface tension typically ranges from 50 to 200 mN/m for pure liquids and solids.

As noted previously, the three surface tensions at the contact line must also balance with external forces such as gravity. The effect of gravity is the reason why puddles are flat rather than spherical caps similar to droplets on a surface. To accurately measure contact angles, it is important to minimize the effect of gravity on the shape of the droplet. The effect of surface tension scales as $F_\gamma \sim \gamma l$ while gravity scales as $F_g \sim \rho g l^3$, where l is the size of the drop, ρ is density, and g is gravity. Therefore, the critical length scale, κ^{-1} is given by:

$$\kappa^{-1} \sim \sqrt{\frac{\gamma}{\rho g}} \quad (2\text{-}11)$$

which is known as the capillary length, which for water at room temperature is approximately 2.7 mm [136]. The effects of gravity can be ignored for droplets smaller than the capillary length.

The above factor yields multiple important characteristics of the system. The first is if the volume of the droplet is known either through precise control during application or by calculating the volume of the spherical droplet prior to contact with the surface, then

the radius of curvature of the droplet in contact with the surface can be determined using the contact angle [137]:

$$R = \sqrt[3]{\frac{3V}{\pi\left(1-\cos\theta_\gamma\right)^2\left(2+\cos\theta_\gamma\right)}} \tag{2-12}$$

where V is the volume of the drop. From there, the radius of curvature can be used to determine the contact radius of the drop using the relation $a = R\cos\theta_\gamma$, which in turn can be used to find the interfacial energy of the solid-liquid interface [134]:

$$E_{SL} = \pi a^2 \gamma_{SL} \tag{2-13}$$

The interfacial energy of the liquid-vapor interface is given by [134]:

$$E_{LV} = 2\pi R^2\left(1-\cos\theta_\gamma\right)\gamma_{LV} \tag{2-14}$$

Combining everything together in conjunction with Equation (2-10) yields the net change in the system's interfacial energy caused by the presence of the droplet [137].

$$\Delta \mathrm{E} = (\pi a^2 \gamma_{LV})\left(\frac{2\left(1-\cos\theta_\gamma\right)}{\cos^2\theta_\gamma} - \cos\theta_\gamma\right) \tag{2-15}$$

From Young's Equation (2-10), equilibrium for a smooth surface is reached when the difference between the solid-vapor and solid-liquid interface tensions balance with the product of the liquid-vapor surface tension and the cosine of the contact angle. From this relationship, two important case can be observed. The first is when the difference between the solid-vapor and solid-liquid surface tensions is greater than or equal to the liquid-vapor surface tension. For this case, the contact angle is approximately equal to

zero and the liquid will fully wet the surface. The case physically occurs for liquids with very low surface tension such as alkanes or oils or by using a solid with a very large surface energy such as clean glass [138]. On the other extreme, complete non-wetting occurs when the contact angle approaches 180° and requires that the solid-vapor and solid-liquid surface tensions is less than or equal to the liquid-vapor surface tension. For most hydrophobic coatings available today, such as Teflon®, the largest contact angle achieved (smooth surface, water in air) is on the order of 120° [139], [140]. To date, extreme hydrophobicity is chemically impossible for smooth surfaces.

2.3.2 Contact Angle Hysteresis

The contact angle provides the means to characterize the static behavior of a droplet on a smooth surface. To understand the dynamic behavior of a droplet on a surface, the dynamic imbalance that forms in the system caused by external forces must be characterized. Generally, when a very small external force is applied to a droplet such as changing the gravity vector, adding fluid, or removing fluid, the droplet will deform but remain pinned until a critical threshold is reached at which point the droplet will move. This deformation changes the contact angle as shown in Figure 2-4. The maximum contact angle before the droplet moves is the advancing contact angle, and the minimum angle before movement is the receding contact angle. It is the imbalance between the advancing and receding contact angles that influences droplet dynamics on a surface and is referred to as contact angle hysteresis. It is essentially a measure of the droplet's friction against the substrate caused by contact line pinning against surface features such

as surface roughness, defects, and contaminants. The force required to move a drop across a surface is then given by $F \sim \gamma_{LV}(\theta_a - \theta_r)$. The contact angle hysteresis provides insight into the mobility of a droplet on a surface. Droplets with small values are relatively mobile, and droplets with high values are considered "pinned" or "sticky" in that even when the surface is oriented vertically, the drop will not move. The interplay of surface roughness is a key attribute affecting contact angle hysteresis.

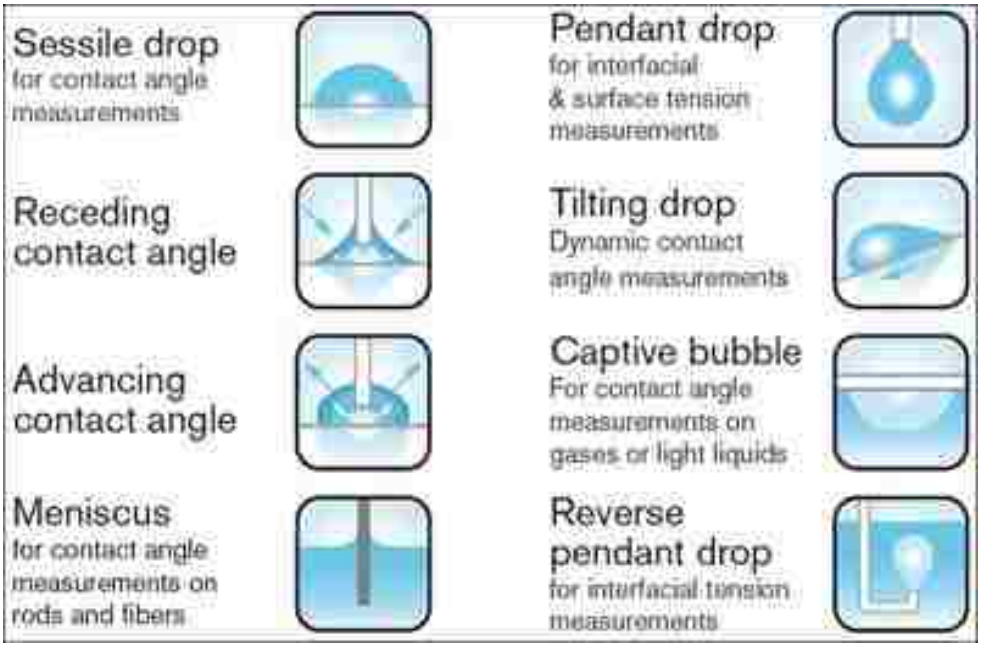

Figure 2-4: Illustrations of the effect of external forces on contact angle and drop shape[2].

2.3.3 Apparent Contact Angle

There are many examples of hydrophobic surfaces in nature, but one of the most well-known is the lotus leaf's ability to repel water. A comparison between the contact angles

[2] http://www.atascientific.com.au/surface-tension-contact-angle.html

for a lotus leaf and Teflon® are shown in Figure 2-5. It is clear from the images that lotus leaves achieve a true superhydrophobic state with very high contact angles unlike Teflon®, one of the most hydrophobic manmade materials, with a relatively modest contact angle of 120°. The reason for this is that lotus leaves are not smooth surfaces and exhibit micro- and nanoscale surface roughness. The texture of the surface plays an important role in the contact angle and can either increase or decrease the contact angle compared to Young's contact angle for a smooth surface. The reason for this is that the texture affects the interaction between all phases at the three phase contact line. The term apparent contact angle is used to characterize drops on surfaces where the wettability is influenced by the surface chemistry and the surface roughness. This concept was introduced by Wenzel in 1936 [77], [78] and followed by Cassie in 1944 [75], [76].

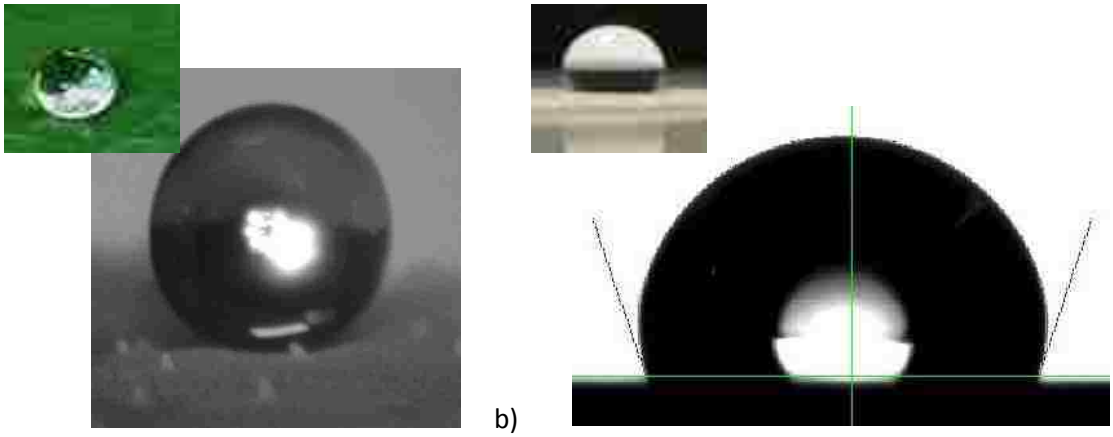

a) b)

Figure 2-5: Photographs of a water drops comparing contact angles between a) a lotus leaf with a contact angle of 170° and b) Teflon® with a contact angle of 120° [141][3,4,5].

[3] https://www.assignmentexpert.com/blog/wp-content/uploads/2014/08/Lotus-Leaf.jpg
[4] http://www.mdtmag.com/article/2009/08/use-expanded-ptfe-membranes-medical-filtration
[5] http://www.ramehart.com/newsletters/2010-09_news.htm

Wenzel noted that surface roughness does not change the values for the three surface tensions and thus does not change the contact angle. However, surface roughness does affect how the three phases interact with each other and thus how the surface tensions dynamically equilibrate, which is shown in Figure 2-6. Wenzel surmised that the values for γ_{SL}, γ_{SV}, and γ_{LV} do not change with surface roughness but the interfacial area affecting the solid-liquid and solid-vapor surface tensions is modified by a dimensionless surface roughness parameter, which is the ratio between the actual surface area to the projected surface area of the textured substrate [77]. This ratio will always be greater than or equal to one. The surface roughness parameter for a uniform array of square ridges of width, w, height, h, and center to center spacing, s, is given by:

$$\mathrm{r}_s = 1 + \frac{2h}{s} \tag{2-16}$$

When the surface roughness length scale is significantly smaller than the droplet size, the directionality of the solid-liquid and solid-gas surface tensions is parallel to the substrate.

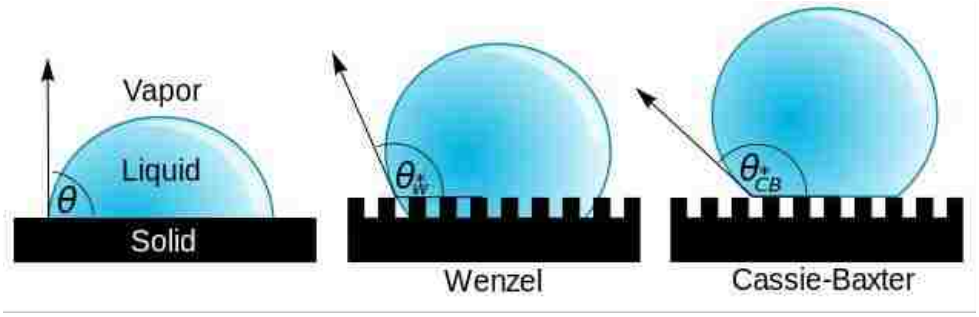

Figure 2-6: Diagram of the various contact models: Young's model for smooth surfaces (left), Wenzel model for rough surfaces (center), and Cassie-Baxter model for rough surfaces (right)[6].

[6] "Contact angle microstates" by Vladsinger - Own work. Based on File:Microstruct superhydrophobic.png, by Acannon2. Licensed under CC BY-SA 3.0 via Commons https://commons.wikimedia.org

The apparent contact angle of a liquid droplet wetting a roughened surface can be calculated by considering the change in energy required for the drop to spread an incremental distance over the surface and solving for the new equilibrium state. The energy balance yields [134]:

$$\mathrm{dE} = \gamma_{LV} dx \cos\theta^* + r_s(\gamma_{SL} - \gamma_{SV})dx = 0 \qquad (2\text{-}17)$$

where, θ^* is the apparent contact angle. Solving the equation for the apparent contact angle and substituting Young's contact angle equation yields the Wenzel equation:

$$\cos\theta^* = r_s \cos\theta_\gamma \qquad (2\text{-}18)$$

The Wenzel equation is plotted in Figure 2-7 and shows that increasing surface roughness will increase the intrinsic wetting characteristics of the surface; in that, if the surface is naturally hydrophilic, increasing the surface roughness will decrease the apparent contact angle. In contrast, increasing the surface roughness of a hydrophobic surface will increase the apparent contact angle. It is by roughening a hydrophobic surface that apparent contact angles exceeding the natural contact angle chemical limit of 120° have been achieved. Thus, to achieve a superhydrophobic surface state, the combination of a hydrophobic surface and adequate surface roughness to increase the contact angle above 150° is required. Apparent contact angles as large as 177° have been achieved in the literature [23].

Despite significantly increasing the apparent contact angle to values larger than 150°, Wenzel drops do not satisfy the requirements for superhydrophobicity. The reason for

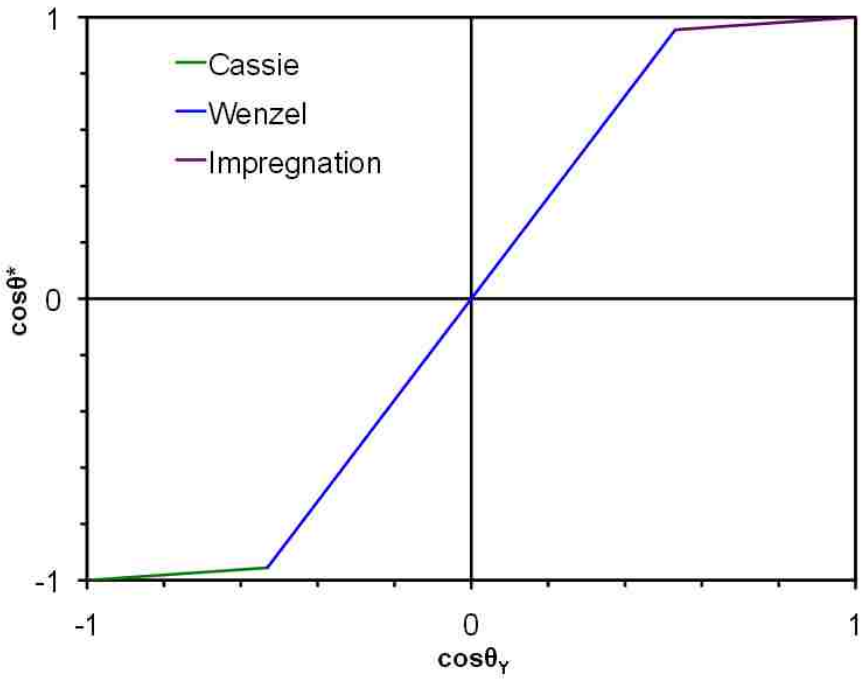

Figure 2-7: Plot of the apparent contact angle and Young's contact angle for a micropost roughened surface (f = 0.095, r = 1.8) showing how surface roughness increases hydrophobicity for intrinsically hydrophobic surfaces and increases hydrophilicity for intrinsically hydrophilic surfaces. The green, blue, and purple lines represent the stable Cassie, Wenzel, and impregnation regimes, respectively [134].

this is that Wenzel drops tend to have very high contact angle hysteresis, which leads to droplet pinning and a loss of superhydrophobicity. This clearly does not solve the lotus leaf problem. The problem was solved by Cassie in 1944 [75], [76] who theorized that as surface roughness increases there is a critical point where the liquid-vapor surface tension is high enough to keep the fluid from penetrating into the solid surface roughness and the continuous solid-liquid interface is replaced by a mixed solid-liquid and liquid-vapor interface as shown on the right in Figure 2-6. The portion of the Cassie drop in contact with the surface is the solid fraction, ϕ, and in the case of a uniform array of ridges is:

$$\phi = 1 - \frac{w}{s} \tag{2-19}$$

Summing the energy required for a Cassie drop to spread on a surface and solving for the equilibrium state yields [134]:

$$\mathrm{dE} = \gamma_{LV} dx \cos\theta^* + \phi(\gamma_{SL} - \gamma_{SV})dx + (1-\phi)\gamma_{LV} dx = 0 \tag{2-20}$$

where the second term captures the new solid-liquid interface, and the third term captures the energy of the liquid-gas interface suspended above the cavities. Solving for the apparent contact angle and substituting Young's equation yields the Cassie equation:

$$\cos\theta^* = \phi\left(1 + \cos\theta_\gamma\right) - 1 \tag{2-21}$$

The Cassie model replaces the continuous wetted perimeter of the Wenzel model with an array corresponding to the geometry of the solid fraction. As the solid fraction approaches zero, the system approximates the perfect non-wetting case of a drop fully suspended in air. Unlike the Wenzel state, the Cassie state usually corresponds to a state where the contact angle hysteresis is very small, which results in highly mobile droplets and superhydrophobicity.

For a rough surface, both the Wenzel and Cassie states are possible. The state that is more energetically favorable depends on Young's contact angle, surface roughness, and the solid fraction. Plotting the Wenzel equation and the Cassie equation shows an intersecting point defined as the critical contact angle, θ_c, where the two states are energetically equivalent with the same apparent contact angle. Setting the Wenzel and Cassie equations equal to each other yields:

$$r_s \cos\theta_c = \phi(1 + \cos\theta_c) - 1 \quad (2\text{-}22)$$

which reduces to:

$$\cos\theta_c = (\phi - 1)(r_s - \phi) \quad (2\text{-}23)$$

Thus, the Wenzel state is the stable energy state when Young's contact angle is less than the critical contact angle, and the Cassie state is more stable when Young's contact angle is greater than the critical contact angle.

In addition to the above, the contact state also depends on the formation of the droplet on the surface [142]. By way of example, a surface with θ_Y = 118°, r = 1.3, and ϕ = 0.05 yields a critical contact angle of 139°, thus the Wenzel state is the preferred energy state. However, if a droplet is gently deposited on the surface, the Cassie state is exhibited until pressure is applied, thereby forcing fluid into the solid and the system permanently changes to the preferred Wenzel state [143]. The presence of the meta-stable Cassie state occurs because of an energy barrier between the two states [79], [144], [145], [146]. In the meta-stable Cassie state, transition requires fluid sliding down surface roughness while initially maintaining the liquid-vapor menisci which is a net increase in surface energy, thereby requiring energy input to initiate transition. Figure 2-8 shows the relationship between the Wenzel, Cassie, and meta-stable Cassie states in the Wenzel regime. Analytical expressions calculating the energy barriers between the Cassie and Wenzel states were first provided by He et al. [147] and Ishino et al. [148]. Thus, how the

droplet is formed or placed on the surface also plays an important role in droplet-surface interactions, especially for pressurized systems.

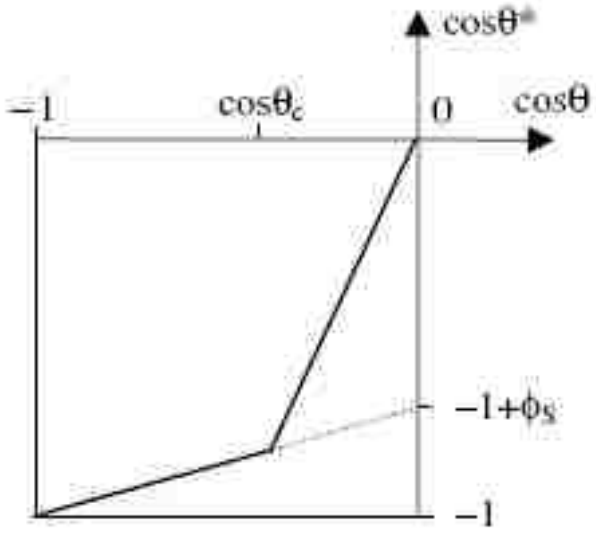

Figure 2-8: Relationship for the Wenzel, Cassie, and metastable Cassie states within the Wenzel regime [142].

2.4 Superhydrophobic Surfaces

It is clear that contact angle, contact angle hysteresis, and surface roughness all play an important role for engineering superhydrophobic surfaces. The interplay of these parameters has been an important area of recent research, the results of which will be summarized in the following sections. The end goal is to develop a set of design requirements that will maximize hydrophobicity and ensure the design of a superhydrophobic surface.

2.4.1 Hierarchical Surface Roughness

To better understand superhydrophobic surfaces, many researchers have explored the numerous examples of superhydrophobic surfaces in nature. As mentioned previously, the lotus leaf is one of the most well-known examples, but Neinhuis and Barthlott [5], [16] studied nearly 200 plants with similar characteristics. They found that nearly all of the hydrophobic plants studied exhibited three general characteristics. The first was a hydrophobic wax coating or small crystal-like wax protein masses on the surface. The second was a microscopic surface texture on the order of 10 μm. These were commonly in the form of bumps or small mounds. Finally, there was a smaller, second-tier surface texturing on the order of 1 μm. The smaller surface texture was a different morphology from the first and usually consisted of small hairs covering the larger surface texturing [5], [16], [17].

The same authors replicated the microstructure of various plant leaves on silicon substrates to decouple the effects of the wax coating, the larger microtexture, and the smaller microtexture [9]. They replicated three different leaf structures (Alocasia macrorrhiza, Rosa landora, and Nelumbo nucifera or lotus plant); however, they were not able to replicate the 200 nm crystal-like wax features on the lotus leaf. The authors also studied the various effects of pillar size and spacing on contact angle and surface wettability. The silicon Alocasia and Rosa samples demonstrated superhydrophobic qualities where droplets formed on the surface and cleaned contaminates from the surface. The simulated lotus plant did not. Water drops coalesced on the surface forming

a film despite the hydrophobic nature of the coating. Based on these results and other surfaces using various micropost spacing led the authors to conclude that surface features less than 5 μm in spacing or size were required to achieve superhydrophobic conditions on patterned surfaces simulating plant structures [9].

Other examples of superhydrophobic surfaces in nature include water striders, butterfly wings, water fowl feathers, various flying insects, and Namibian beetles to name a few. Gao and Jiang [10] reported that water strider legs are composed of microscale hairs that are covered in nanogrooves, and that the hierarchical structure enables the supporting force that allows water striders to walk on water. Similarly, water fowl feathers consist of a branching two-tier roughness consisting of microscale barbs and nanoscale barbules [6], [15]. Many researchers have investigated various superhydrophobic surfaces in nature, and all cases yield similar results in that there is a two-tier hierarchical structure to the surface. One tier consists of surface features on the order of microns to tens of microns, and a smaller tier that consists of features on the order of hundreds of nanometers to microns [4], [7], [11], [18], [19], [20].

Many synthetic superhydrophobic surfaces using hierarchical structures have been investigated over the past two decades. Gogte et al. [25] and Truesdell et al. [36] explored randomly distributed micro-structured surfaces that were coated with a hydrophobic aerogel coating. As nano- and microscale surface fabrication techniques have improved, so has the ability of researchers to investigate the effect of hierarchical structures on

superhydrophobicity including the microridge periodic array structures explored by Turesdell et al. [36]. Others, such as Cheng et al. [8], used thermal annealing to remove the nanoscale hairs from lotus leaves and found that the apparent contact angle for annealed leaves having microscale features only was approximately 20° less than the unadulterated leaves with a hierarchical surface structure. Li et al. [14] fabricated surfaces with a moderate surface roughness of 1.5 using microposts. The micropost surface resulted in a meta-stable Cassie state; however, adding silica nanoparticles to the pillar surface dramatically lowered the contact angle hysteresis and formed a stable Cassie state. Kwon et al. [13] used gas phase isotropic etching to add nanoscale roughness to silicon microposts and found that the two-tier surface had a higher apparent contact angle and a lower contact angle hysteresis than either the microscale or nanoscale only surfaces. Finally, Koch et al. [12] fabricated a hierarchical lotus structure into a silicon master and thermally evaporated lotus wax into self-assembled tubules to provide nanoscale roughness. The results are shown in Table 2-1, and clearly show that the two-tier roughness provides the best performance.

Table 2-1: Apparent contact angle and contact angle hysteresis for microscale only, nanoscale only, and two-tier hierarchical structural for silicon lotus leaf replicas [12].

Sample	*Apparent Contact Angle [◦]*	*Contact Angle Hysteresis [◦]*
Microscale roughness only	156	29
Nanoscale roughness only	167	6
Two-tier roughness	171	2

The previous studies indicate that two-tier roughness is critical to achieving an optimal superhydrophobic state; however, there are some studies that indicate similar performance can be achieved with nanoscale roughness only [42]. Cha et al. [149] measured the contact angles for surfaces with pillar-based roughness. The apparent contact angle for the micropost roughness, nanopillar roughness, and two-tier roughness were 143°, 149°, and 150°, respectively. Boreyko et al. [57] performed a similar study measuring the apparent contact angle for microscale, nanoscale, and two-tier surface roughness for various mixture concentrations of water and ethanol. Their results were similar to Cha et al. for very low concentrations of ethanol. All three papers were able to achieve similar performance between nanoscale only and two-tier surface roughness, which indicates that microscale roughness is much less important than nanoscale roughness for superhydrophobicity with respect to achieving high apparent contact angles.

In addition to apparent contact angle, Cha et al. and Boreyko et al. evaluated the wetting and dewetting transitions for various surfaces and found that microscale roughness played an important role in superhydrophobic stability and transitioning from the Cassie state to the Wenzel state and back to the Cassie state. One-tier roughness surfaces were much more likely to transition to the Wenzel state and not return to the Cassie state after wetting occurred. However, the two-tier roughness surfaces were more stable in the Cassie state and resisted wetting. In addition, the two-tier surfaces dewet from the Wenzel state to the Cassie state as long as both tiers of roughness were not fully

wetted. The one-tier surfaces were not able to dewet after partial impalement into the surface [57]. The two-tier surface also had a higher calculated Laplace pressure at transition than the one-tier surfaces and was ~30% higher than the microscale only and ~50% higher than the nanoscale only surfaces [57]. It is important to note that the microscale only surface had a higher resistance pressure than the nanoscale only surface. Thus, two-tier roughness is important for a stable Cassie state under pressure.

2.4.2 Water Droplet Studies

To better design superhydrophobic surfaces, several investigators have explored the various effects micropatterned surfaces and hydrophobic coatings have on droplet behavior. Oner and McCarthy [150] investigated the effects on hydrophobicity of various micropost parameters including pillar height, geometry, silanizing agent, pillar cross-sectional area, and pitch using water droplets. For each of the test samples, the advancing and receding contact angles (θ_a and θ_r, respectively) were measured using a goniometer, and the wettability was determined based on the minimum tilt angle at which a droplet moved, α, using [151]:

$$mg \sin \alpha = w\gamma_{LV}(\cos \theta_r - \cos \theta_a) \quad (2\text{-}24)$$

where m is the mass, g is the force of gravity, w is the width of the droplet horizontal to the direction of motion, and γ_{LV} is the surface tension. From this, it is important to note that the contact angle hysteresis is the critical parameter and not the contact angle for

determining the effective slip that can be expected for a surface. From their measurements, Oner and McCarthy [150] observed that:

1) Surfaces consisting of square posts with X-Y dimensions between 2 and 32 μm with similar spacing between posts exhibited superhydrophobic behavior
2) Surfaces with X-Y dimensions between 64 and 128 μm exhibited liquid intrusion between posts and subsequently droplet pinning
3) Increasing the perimeter-to-area ratio for the cross-section of the post diminishes the hydrophobic behavior of the surface
4) Hydrophobicity was independent of pillar height and silanizing agent

From these observations, they concluded that the key issue for enhancing hydrophobicity and thus increasing surface slip was the structure of the three phase (solid-liquid-vapor) contact line including shape, length, continuity of contact, and amount of contact.

Yoshimitsu et al. [86] furthered the understanding of droplet behavior on superhydrophobic surfaces by investigating the sliding behavior of water droplet size on various pillar and ridge structures. Small droplets measuring 1 mg were used to determine the contact angle, and larger droplets measuring between 7 and 35 mg were used to evaluate the effect of droplet size on the sliding behavior [86]. Photographs of the 1 mg droplets on the micropost structure as well as the contact angle, roughness

factor from Wenzel's equation, and the pillar height are presented on Figure 2-10. Roughness factors for Wenzel's equation were calculated by [86]:

$$r_s = \frac{(w+q)^2 + 4wh}{(w+q)^2} \tag{2-25}$$

where w is the post width, q is the distance between posts, and h is the post height.

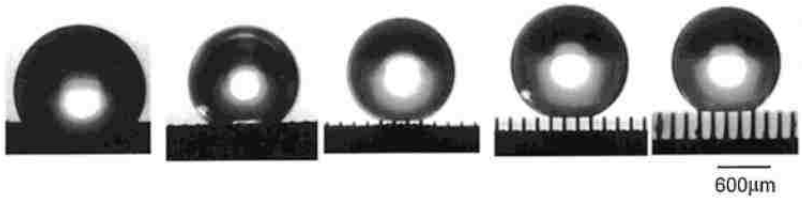

Contact angle of water θ' [deg]	114	138	155	151	153
Roughness factor r	1.0	1.1	1.2	2.0	3.1
Pillar height c [μm]	0	10	36	148	282

Figure 2-9: Photographs of the 1 mg droplets on various micropost heights [86].

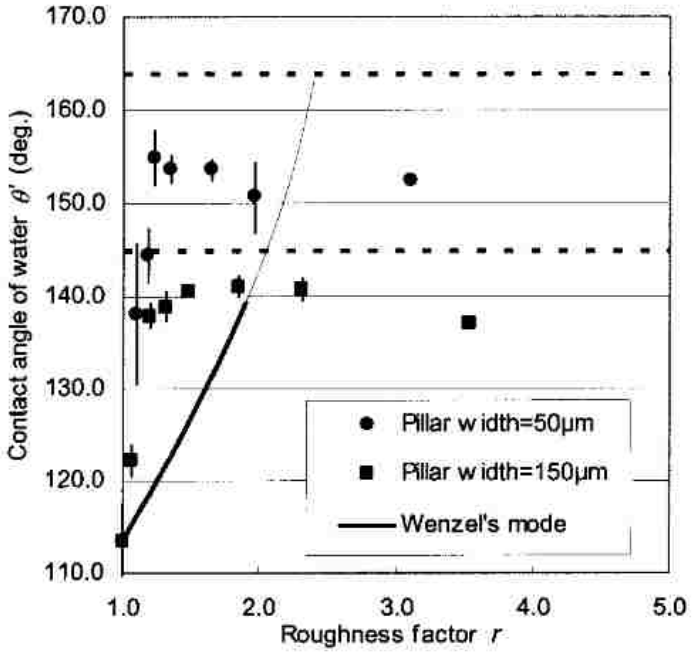

Figure 2-10: Effect of roughness factor on contact angle for 50 μm and 150 μm post spacing [86].

It can be concluded from Figure 2-10 that the Wenzel state exists for roughness less than 1.10 and the Cassie state for roughness greater than 1.23 at which point the contact angle becomes constant. The change in contact angle for both 50 μm and 150 μm post spacings are shown in Figure 2-10. The dashed lines in the figure indicate the theoretical values assuming a pure Cassie state where the fluid contacts the top of the pillars only. The experimental data were less than these theoretical maximums indicating fluid intrusion into the asperities. According to simulations performed by Johnson and Dettre [152] using an assumed sinusoidal surface structure, the dominate hydrophobicity mode continuously switches between Wenzel and Cassie states based surface roughness [86]. However, the discrepancy between experimental and theoretical values indicated that additional factors affected the measured contact angles and were most likely attributed to surface preparation.

Finally, Yoshimitsu et al. [86] compared the sliding behavior for micropost and microridge geometries. The pillar width, groove width, and pillar height were 96, 49, and 160 μm, respectively. The roughness factors were 3.9 and 3.2 for the respective geometries, thus both should be in the Cassie state. The geometry providing the lowest sliding angle were the microridges oriented parallel to the flow direction followed by the microposts and then the microridges orthogonal to the flow. This supports observations that sliding behavior depends on the length and continuity of the three-phase interface line where a continuous, short three-phase contact line is preferred. Therefore, it is oftentimes more beneficial to optimize the geometry of the surface with respect to the

three-phase contact line than to increase the contact angle to minimize the solid-liquid interface.

Whereas the work of Yoshimitsu et al. focused on superhydrophobic surfaces with periodic microstructure arrays, Gogte et al. [25] investigated the dynamic behavior of droplets on superhydrophobic surfaces with randomly distributed microstructures. In their tests, they used a 20 cm long self-leveling incline and a syringe pump to dispense drops and measured the time and position of the drop moving down the incline. They compared this data to the ideal situations of a droplet rolling or perfectly slipping down an incline. They compared a smooth surface with two different grit sandpaper: one with 8 μm texture and one with 15 μm texture. All three surfaces were coated with a hydrophobic coating "prepared by a variation of the low temperature/pressure aerogel thin film process wherein tetraethylorthosilicate was replaced with a 1.0:0.3 molar ratio of tetramethylorthosilicate:trifluoropropyltrimethoxysilane" [25].

The results from Gogte et al. [25] showed that the dynamic behavior of a droplet on a shallow incline (1° to 3°) was highly dependent on both the hydrophobic coating and the surface texture. The hydrophobic coated smooth surface produced droplet dynamics that inhibited the motion of the droplet down the incline. Initially, the droplet moved down the smooth surface following pure rolling behavior. After approximately 0.6 s, the motion was slowed and droplet moved slower than the pure rolling case. As for the textured surface, the combination of the hydrophobic coating and the sandpaper

textured surface allowed the droplet to move faster than the pure rolling case. The results for the 15 μm texture samples reside between the pure rolling and pure slip cases. The results for the 8 μm texture samples were significantly better and more closely approximated pure slip until approximately 0.8 s. The ensemble average of the time versus position results for the three surface compared to the case for pure rolling and pure slipping are plotted on Figure 2-11a. The results from Gogte et al. [25] clearly indicate that textured superhydrophobic surfaces are required to achieve a true slip condition compared to superhydrophobic surfaces only. They theorized that the no slip boundary condition holds where the fluid is in direct contact with the solid and that a shear free layer with high slip velocity exists at the fluid-vapor interface as shown on Figure 2-11b, which is supported by their experimental results [25].

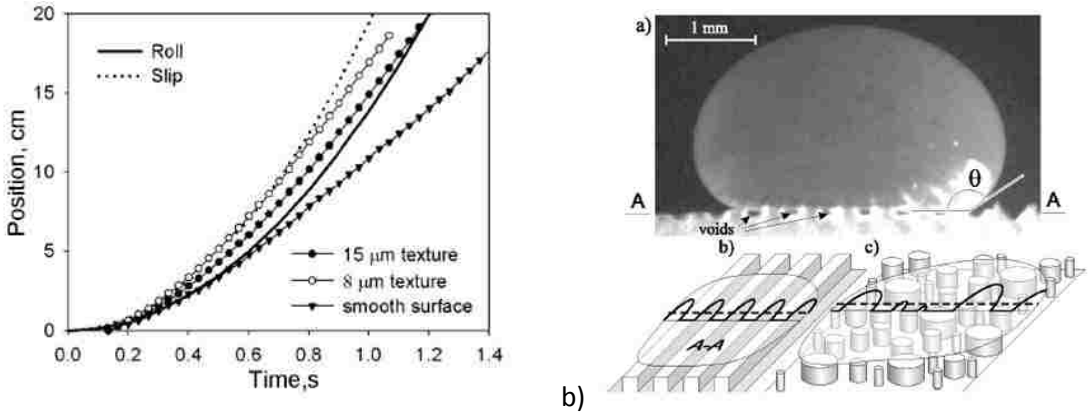

Figure 2-11: a) Ensemble-averaged position of drop dynamics on a slightly incline plane for smooth and textured hydrohphobic surfaces compared to the cases of pure rolling and pure slip. b) Schematic of fluid behavior near a superhydrophobic surface for both a patterned microridge surface and an idealized, randomly distributed textured surface [25].

2.5 Summary and Conclusions

Based on the previous discussions, the requirements for a stable superhydrophobic surface at ambient atmospheric conditions can be summarized as:

1) Apparent contact angle exceeding 150°
2) Contact angle hysteresis less than 5°
3) Nanoscale roughness less than 5 μm
4) Microscale roughness greater than 5 μm but less than 60 μm

Items 3 and 4 are general guidelines and not design requirements because the ability of the surface to support the fluid in the Cassie state depends on multiple factors that have not been fully explored. For example in section 3.1.2, it will be shown that carefully designed and fabricated microridges can maintain a pure Cassie state up to 200 μm for smooth microridges and up to 430 μm for microridges with nanotexturing [28]. The limit for microposts was shown to be 60 μm, hence the parameter in item 4 [27].

Because of their high slip tendency and an increasing ability to fabricate micro- and nanoscale features, superhydrophobic surfaces have received great attention in the recent years for studying slip effects on fluid dynamics and heat transfer. The next chapter will review the current literature on slip effects in laminar and turbulent fluid flow and heat transfer.

Chapter 3

Slip Flow Review

It is clear from previous researchers that superhydrophobic surfaces combining hydrophobic coatings, micropatterning, and nanoscale surface features achieve slip at the wall for typical Newtonian fluids. Recently, researchers have worked to understand these effects and the microscale and macroscale levels for friction loss, drag reductions, and heat transfer effects. This chapter will review the current state of literature for drag reduction studies and heat transfer effects.

3.1 Drag Reduction in Laminar Flow

3.1.1 Drag Reduction Studies

Investigating superhydrophobicity on droplet dynamics helps to understand the basic physics underlying the interactions, but an understanding of the drag reduction and the merits of slip flow must also be investigated for a useful system to be developed. For the laminar regime, two different research thrust were pursued. The first focused on

understanding and evaluating the drag reduction provided by superhydrophobic surfaces. The second look toward quantifying and maximizing the slip length for pressurized flows.

Watanabe et al. [37] were among the first to evaluate the laminar drag reduction of superhydrophobic surfaces using coaxial rotating cylinders by measuring the torque on the cylinders to determine the shear flow. They used this setup because of the simplicity of the analytical solution. For their experiments, they varied the rotation rate of the moving cylinder, the radius ratio between the cylinders, and the glycerin mixture from 60% to 80%. In addition, they used two surface treatments: 1) fine particles of polytetrafluoroethylene (PTFE) bonded to the wall and 2) a mixture of fluorine-alkane-modified acrylic resin and hydrophobic silica [37]. In their analysis, they assumed a slip condition for which, the shear stress at the wall followed Navier's condition, $\tau = \lambda u_s$, where τ is the wall shear stress, λ is the sliding coefficient, and u_s is the slip velocity at the wall. Figure 3-1 presents the results for the baseline stainless steel wall, wall 1 (left), and wall 2 (right) where it can clearly be seen that no-slip held for wall 1 and slip occurred for wall 2, when compared to the baseline surface. Even though wall 1 was superhydrophobic the no-slip boundary condition held. It was postulated that air or vapor trapped in the cracks inherent in the surface provided the means for slip for wall 2. These results underscore the importance of the air layer interaction in achieving slip at the boundary [37].

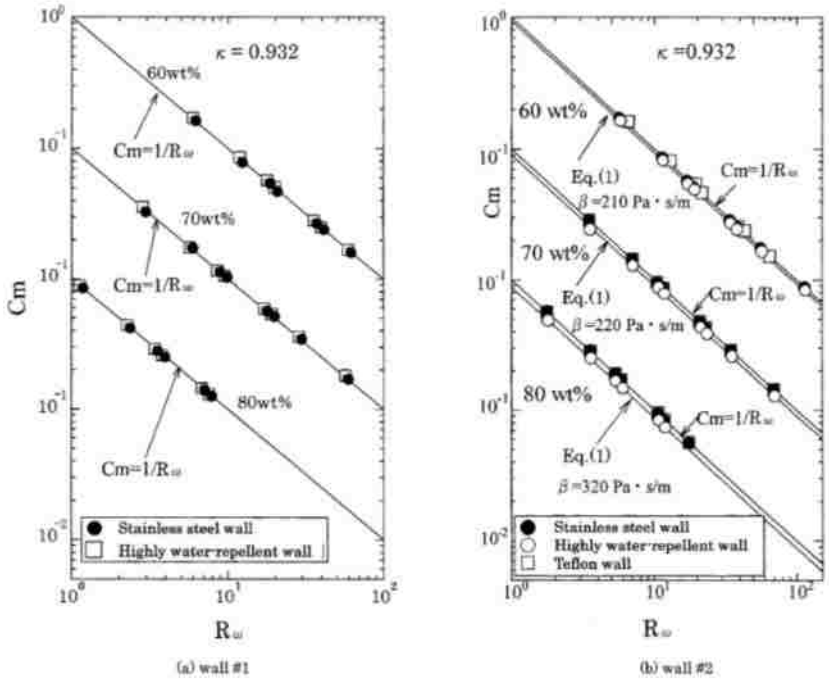

Figure 3-1: Toque coefficient for the stainless steel, Teflon, and fluorine-alkane-modified acrylic resin and hydrophobic silica walls [37].

Truesdell et al. [36] followed a similar approach to Watanbe et al. using coaxial rotating cylinders to measure the drag reduction effect for superhydrophobic surfaces. However, unlike the previous effort, they fabricated microridge structures on the surface. As a result, they measured a maximum increase in drag reduction of 20%. They also reported slip lengths an order of magnitude larger than the groove size [36]. Mohaven et al. [32] used a rotating disc approach to measure the drag reduction of a superhydrophobic surface consisting of 7075 aluminum that was sandblasted for 30 seconds using 0.2 μm SiC sphere to create surface roughness and was then sol-gel coated using TiO_2 particles. Their reported results measured a drag reduction of 30% for laminar flow and 15% for turbulent flow [32].

Ou, Perot, and Rothstein [33] followed a similar course and investigated laminar drag reduction using superhydrophobic surfaces with well-defined micron-sized pillars to enhance surface roughness. Using standard photolithography techniques, they produced posts with precisely controlled size, height, spacing, and geometry onto silicon wafers, which were then silanized for superhydrophobicity. The surfaces were placed in an experimental flow cell, and the pressure drop as a function of flow rate was measured. Figure 3-2 shows the optical micrograph of the smooth hydrophobic surface and the superhydrophobic surface with d = 30 μm and w = 30 μm posts as well as the pressure drop results for the various conditions tested [33].

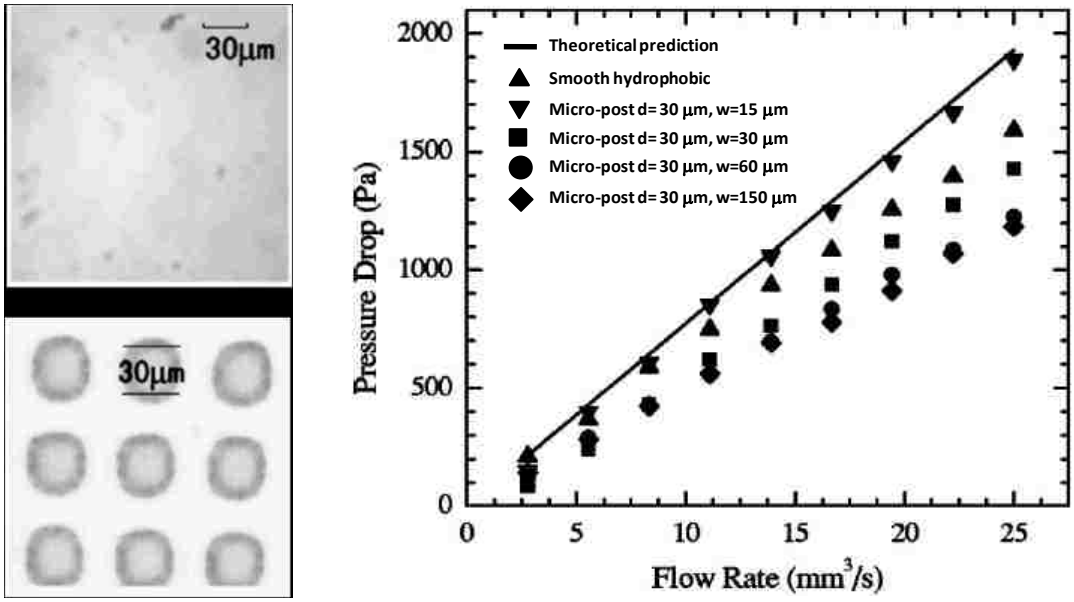

Figure 3-2: SEM photographs of the smooth and micropost surfaces (left) and the pressure drop comparison for the various geometries studied (right) [33].

The results in Figure 3-2 show that the pressure drop increased linearly with flow rate and monotonically decreased with increasing post spacing. In addition, pressure drop

was found to increase linearly with increasing channel height by varying the height from 76.2 μm to 254 μm while holding the aspect ratio fixed to minimize edge effects in the channel. Because of these observations, it was hypothesized that the reduction in pressure drop was attributed to a shear-free liquid-vapor interface between posts supported by the surface tension of the water as a result of the combination of patterned microscale roughness and hydrophobic surface treatment. The shear-free interface resulted in a pressure drop reduction of greater than 40% and apparent slide lengths exceeding 20 μm [33]. The existence of this interface was verified with a confocal surface metrology system by measuring the profile of the interface.

Ou and Rothstein [34] followed this work by investigating the drag reduction on microridge superhydrophobic surfaces by measuring the velocity profile through the channel with a μ-PIV system. They then compared their measurements to the analytical solution presented by Philip [153] and their Computational Fluid Dynamic (CFD) predictions from the commercial code Fluent™ (Fluent Inc., New Hampshire, USA) for both the velocity profile in the channel and the pressure drop reduction. Those results are presented in Figure 3-3, which shows good agreement for the velocity profile within the bounds of the experimental error. As for the pressure drop reduction, both the analytical and the numerical solutions provide good qualitative agreement with the experimental results; however, quantitatively they under predicted for all cases.

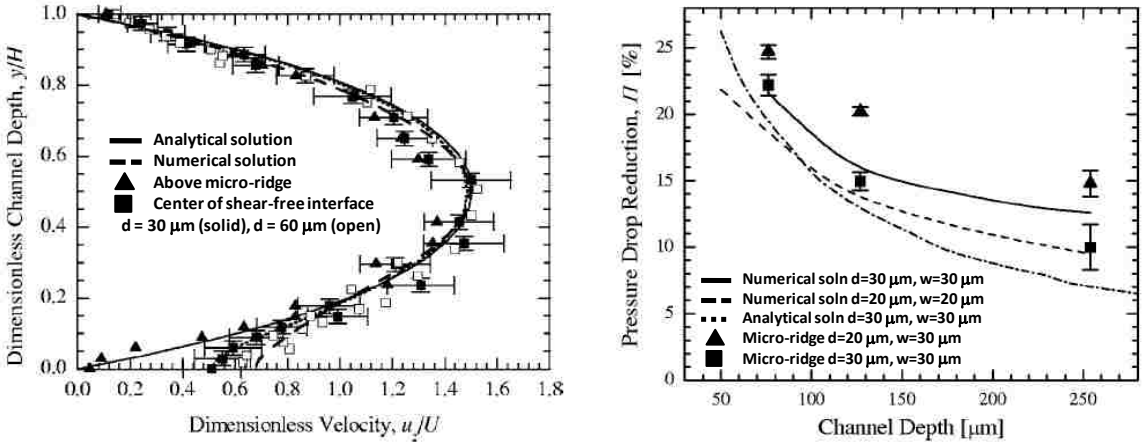

Figure 3-3: The velocity profile (left) and pressure drop reduction (right) for a superhydrophobic surface exhibiting slip compared to Philip's analytical solution and Ou's numerical solution [34].

Previous results by Ou et al. had good agreement with Philip's analytical solution for velocity but not pressure loss. Woolford et al. [38] enhanced the analytical solutions of Philip [153] and Lauga and Stone [146] by developing predictive correlation expressions for the Poiseuille number, the product of the friction factor and the Reynolds number, in terms of the governing variables for laminar flow, which are presented in Table 3-1 for the transverse and longitudinal flow configurations in the Wenzel and Cassie states.

Table 3-1: Analytical relations for the Poiseuille number for Cassie and Wenzel states [38].

fRe	State	Rib/cavity configuration	Limitations
$\frac{96}{1+\frac{3w}{\pi D_h}\ln[\sec(F_c\pi/2.53)]}$	Wetting	Transverse	$Re \to 0$ $Z_c > 0.25$
$\frac{96}{1+\frac{6w}{\pi D_h}\ln[\sec(F_c\pi/2)]\left[c_1+\frac{c_2}{\left((Re_w+c_3)^2+c_4\right)}\right]}$	Superhydrophobic	Transverse	$Z_c > 0.25$ $W_m < 1.0$
$\frac{96}{1+\frac{7.23w}{\pi D_h}\ln[\sec(F_c\pi/2.53)]\left(1-e^{-5.41Z_c/F_c}\right)+\hat{Q}_c'}$	Wetting	Longitudinal	None[1]
$\frac{96}{1+\frac{12w}{\pi D_h}\ln[\sec(F_c\pi/2)]\left(1-e^{-5(Z_c/F_c)^{3/4}}\right)}$	Superhydrophobic	Longitudinal	$W_m < 1.0$

These correlation expressions were then compared to experimental data collected by Woolford et al. [38]. Overall the expressions captured the overall trend of the data; however, significant excursions were observed for some conditions. These were primarily attributed to partial wetting for which a full Wenzel or Cassie state could not be achieved. Figure 3-4 compares the experimental Poiseuille number to the correlation value for the normalized pressure based on the Laplace pressure. From the plot, it is apparent that the correlation expression more accurately predicts the transverse value than the longitudinal value. The authors attribute this to the instability of the Cassie state in the longitudinal configuration [38].

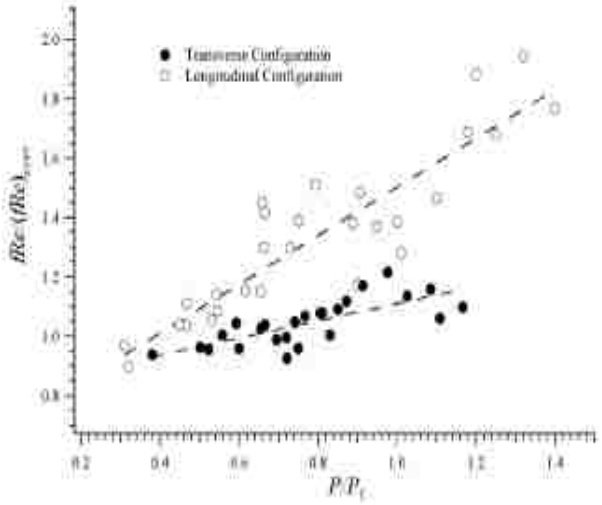

Figure 3-4: A comparison of the experimental Poiseuille number to the correlations presented by Woolford et al. [39].

3.1.2 Slip Length Studies

Many of the previous efforts confirmed the existence of liquid slip using structured hydrophobic surfaces, but they focused on droplet-surface interaction and low pressure

flow over the surface. Choi and Kim [22] presented one of the first efforts to focus on engineering the surface to maximize liquid slip under higher pressure (1 atm) flow by minimizing the liquid-solid contact area. To that end, they produced "nanoturf" on a silicon wafer consisting of 1 – 2 μm tall needle structures with a pitch between 0.5 and 1 μm. They then treated both smooth and nanoturf surfaces to be hydrophobic by spin coating Teflon® AF (DuPont) on the surface. The slip length for each surface was then measured using a cone-and-plate rheometer. Because of the low sensitivity of the apparatus, only the hydrophobic nanoturf sample provided a measureable slip length of ~50 μm for a 30% glycerin solution, which was "a much larger slip (i.e. at least 2 orders of magnitude higher) than what we [Choi and Kim] may expect from all other surfaces" investigated at that time [22].

Choi et al. [154] continued this line of investigation but turned their focus to microridge geometries in place of the nanoturf structure. They measured the slip and drag reduction for arrays of 50 nm wide by 3, 5, or 11 μm tall nanogratings spaced 150 nm apart under pressurized flow. For the 2 cm by 2 cm test samples, they measured slip lengths between 100 and 200 nm and drag reduction between 20 and 30% for flow parallel to the gratings [154]. It should be noted that these values are lower than those reported by Ou, Perot, and Rothstein [33], [34]. The difference between the two studies is that Ou, Perot, and Rothstein conducted their experiments at relatively low pressures, less than 5 kPa; whereas, Choi et al., conducted theirs at higher pressures, ~100 kPa. The

pressure difference necessitated the use of closely spaced ridges to maintain the Cassie state, thereby reducing the overall performance of the system.

Recently, Lee, Choi, and Kim [27] investigated the effects gas fraction and surface feature pitch have on the slip length and found that slip on structured surfaces increased exponentially with gas fraction and linearly with pitch. They calculated the slip length by measuring the pressure drop through superhydrophobic channels at different flow rates compared to the expected pressure drop for a no-slip boundary condition. They found that by precisely fabricating a near defect-free micropattern structure they were able to achieve results approaching the "theoretical thermodynamic limits for a dewetting surface condition and demonstrated unprecedentedly large slips, up to 185 μm" [27]. They confirmed that both gas fraction and large pitch are key parameters for achieving a superhydrophobic Cassie-Baxter state and thus a maximum slip effect. The results for gas fraction and pitch with respect to pitch length are shown on Figure 3-5.

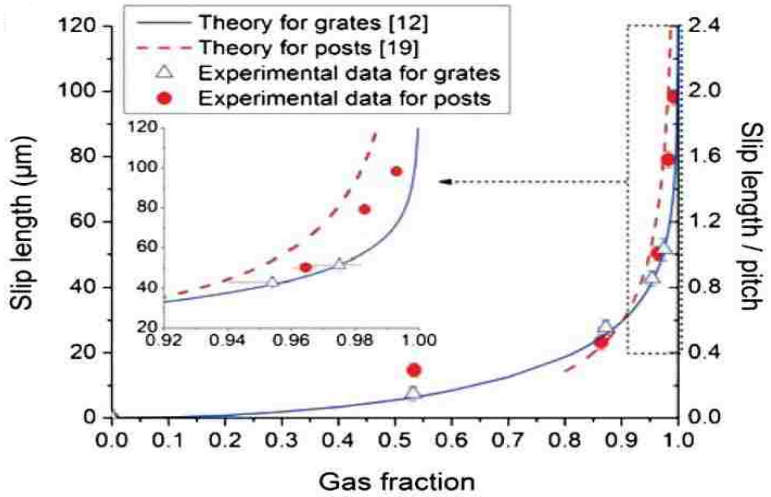

Figure 3-5: The effect of gas fraction on the slip length with the pitch fixed at 50 μm [27].

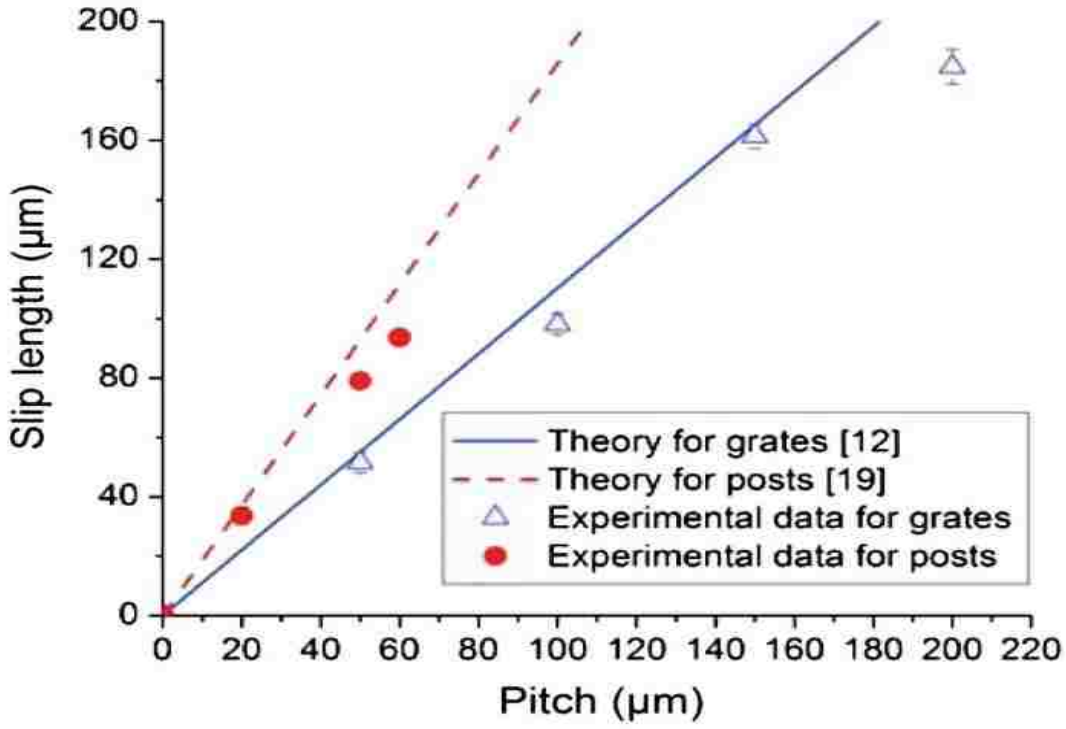

Figure 3-6: The effect of pitch on the slip length with the gas fraction fixed at 98% [27].

Lee and Kim [28] followed their previous work and combined hydrophobic surface coatings, microscale patterning, and nanoscale roughness on the microscale structures to develop "well-defined micro-nano hierarchical structures" with the highest slip length achieved at that time for micropost and microridge structures. The nanoscale roughness as shown in Figure 3-7 helps to stabilize the Cassie state for higher gas fractions and higher pressures than the micro-smooth structures previously tested. The extension of a stable Cassie state allowed for a large pitch to be used thereby minimizing the three phase contact line. As a result, they achieved slip lengths of 140 μm for micropillars and 400 μm for microridges. These results are nearly an order of magnitude greater than those

previously reported by other authors and 2x greater than reported in their previous article [28].

a) 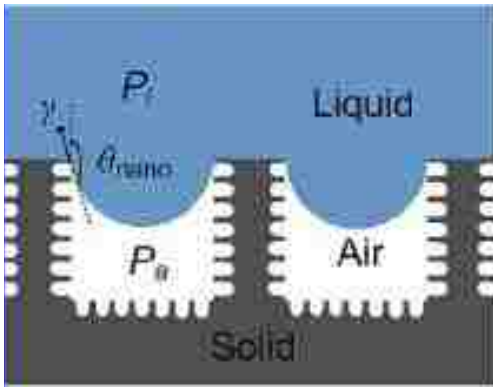

b) 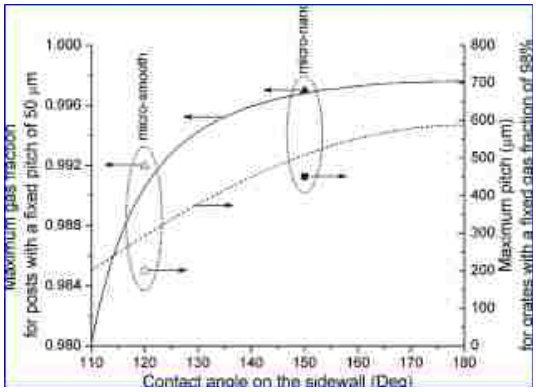

Figure 3-7: a) Schematic of the microscale features with nanoscale roughness and b) predicted maximum gas fraction and pitch before asperity wetting commences for the microscale only and combined microscale structure with nanoscale roughness [28].

Finally, in 2011, Lee and Kim [29] reported that increasing gas fraction improves slip as long as the additional features do not permit liquid intrusion below the surface of the feature. This is an important component of achieving maximum slip performance because increasing the gas fraction and nanoscale features beyond the ability of the surface to resist liquid intrusion can greatly decrease the slip length. The geometry of the top surface is key. Lee and Kim reported that the rounded features on molded polymer microstructures such as PDMS adversely affected slip and yielded lower slip lengths compared to silicon micro-structures with sharp corners that do not allow "downward sliding of the triple line" [29]. Their findings provide guidance on the roles and limitations of nanoscale roughness on hierarchical superhydrophobic surfaces.

Most experimental investigations have used photolithography to fabricate patterned surfaces on silicon wafers which lends itself to microfluidic applications but is less appealing for larger scale applications. Joseph et al. [26] used plasma enhanced chemical vapor deposition to produce densely spaced carbon nanotube (CNT) forest in the place of microposts. Using μ-PIV, they measured slip lengths between 1 and 6 μm. These values are much lower than those reported for the silicon wafer substrates, which is attributed to the less than optimal geometry provided by the CNT forest. However, their approach was the first major attempt to transition the concept to a more usable form for macroscopic applications [26].

3.2 Drag Reduction in Turbulent Flow

The majority of the work relating to the effect of superhydrophobic surfaces in turbulent flow has been to determine the drag reduction rather than the effective slip length of the surface. The first effort to investigate turbulent flow over patterned superhydrophobic surfaces was presented by Gogte et al. [25] where they measured the percent drag reduction for a Joukovsky hydrofoil. They found the percent drag reduction to be a maximum of 18% for a Reynolds number of 2000 and 8 μm microridge spacing and decreasing with increasing Reynolds number. However, Rothstein notes that "only the total drag was reported, and the individual contribution of friction and from drag was not deconvoluted" [35]. These results are also similar to those reported by Balasubramanian et al. [155] for flow over an ellipsoid model.

More recently, Martell et al. [30] used numerical simulation to determine the effect of superhydrophobic surfaces on turbulent flow. They studied both micropost and microridge geometries and applied a no-slip boundary condition to the top surface and a no-shear condition to the vapor-fluid interface. Their results predict increasing drag reduction with increasing feature spacing, which is consistent with reducing the three phase contact line length. However, they also found that post geometries provide higher slip velocities and larger shear stress reductions than ridge geometries for a given d/w, which is contrary to the results for laminar flow [30]. In addition, according to Rothstein, Martell et al. numerical simulations also predict that "unlike laminar flows, in turbulent flows, increasing the flow rate and Reynolds number results in an increase in the superhydrophobic drag reductions" [35]. This is also inconsistent with the results presented by Gogte et al [25]. However, these predictions are consistent with results presented by Daniello et al. [156] which are shown in Figure 3-8 where the friction coefficient decreased with increasing Reynolds number until reaching a maximum of ~50% at which point it leveled off. From these results, they hypothesized that the proper scaling dimension was the viscous sub-layer thickness and that the onset of drag reduction occurs when the viscous sub-layer thickness approached the microscale feature size [156]. Finally, these results also qualitatively agree with those from Woolford et al [39]. The friction factor they measured was constant above a Reynolds number of 4800; however, their measured reduction was 11%, which is significantly less than Daniello's results.

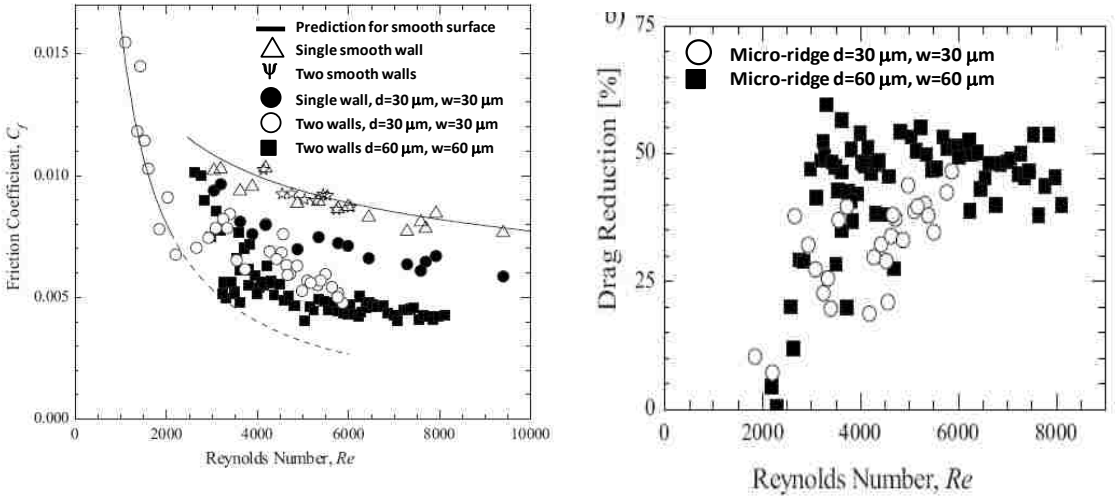

Figure 3-8: Friction coefficient (left) and drag reduction (right) for turbulent flow over superhydrophobic surfaces [156].

Many of the experimental results measuring drag reduction in turbulent flow, as well as a detailed literature review on the subject, were summarized by Aljallis et al. [157] and are reproduced here for convenience. The experimental research performed by Aljallis et al. extended the effects of superhydrophobic coatings on turbulent drag beyond those previous discussed into the range of $10^5 < Re_L < 10^7$ testing plates in flow speeds up to 30 ft/s. They found that for Reynolds numbers less than 10^6 up to 30% drag reduction was achieved. However, they also found that for Reynolds numbers greater than 10^6 increased drag was observed, which was "ascribed to the morphology of the surface air layer and its depletion by high shear flow" [157]. These results further support the requirement of a stable air layer to achieve an apparent slip condition and drag reductions as well as emphasize the importance of a stable vapor layer, which could have significant

implications across different surface textures, wetting states, length scales, and flow conditions.

Table 3-2: Summary of experimental results for superhydrophobic surface slip effects on turbulent flow [157].

Author [Ref. No.]	Flow type	Sample size (order of magnitude)[a] (m)	Reynolds number (Re) range	Surface pattern		Max. drag reduction and associated Reynolds number[b]
				Scale	Regularity	
Daniello *et al.* [30]	Internal (channel)	10^{-2}	2.0×10^3 - 9.5×10^3	Micro	Ordered	50% at $Re_D = 5.3 \times 10^3$
Woolford *et al.* [31]	Internal (channel)	10^{-2}	4.8×10^3 - 1.0×10^4	Micro	Ordered	11% throughout
Balasubramanian *et al.* [32]	External (blunt body)	10^0	1.0×10^5 - 6.0×10^5	Micro	Random	10% at $Re_C = 5.4 \times 10^5$
Zhao *et al.* [33]	External (flat plate)	10^{-1}	1.0×10^4 - 5.0×10^6	Micro	Random	9% at $Re_L = 2.0 \times 10^4$
Henoch *et al.* [34]	External (flat plate)	10^{-1}	1.2×10^5 - 5.8×10^5	Nano	Ordered	50% at $Re_L = 3.7 \times 10^5$

[a]For internal flow, it represents a hydraulic diameter. For blunt body, it represents a chord length. For flat plate, it represents the effective plate length tested for flow experiment.
[b]For internal flow, $Re_D = V_{ave} D/\nu$, where V_{ave}, D, and ν represent an average velocity, a hydraulic diameter, and kinematic viscosity, respectively. For blunt body, $Re_C = V_\infty C/\nu$, where V_∞ and C represent a free stream velocity and a chord length, respectively. For flat plate, $Re_L = V_\infty L/\nu$, where L represents the effective plate length wetted by liquid.

3.3 Thermal Effects of Slip Flow

The thermal effects of slip flow have been examined for a number of cases and applications including gas flow through ducts and in rarefied regimes as well as in liquids and gases in microchannels. Many of the cases analyzed consider conditions where temperature jump at the wall plays an important role or where the Knudsen number is much less than one. The Knudsen number is the dimensionless ratio between the molecular mean free path and the characteristic physical length scale of the system and

is used to determine whether continuum mechanics or statistical mechanics approaches should be used. For micro- and nanochannel flow problems where continuum methods are not applicable, slip flow has been shown to increase heat transfer performance. Shojaeian and Kosar [67] studied the effects of a slip boundary condition on convective heat transfer for non-Newtonian fluid flow between parallel-plates and found that an increase in the slip coefficient leads to an increase in the Nusselt and Bejan numbers and a decrease in global entropy generation.

One of the first studies to investigate the effects of pressure driven flow was completed by Nagayama and Cheng [121] where they studied a Lennard-Jones fluid in a nanochannel using molecular dynamics. Their results show that a gas gap forms between the liquid and the solid resulting in a low friction surface causing slip at the interface and a plug flow velocity profile with non-uniform temperature and pressure profiles near the walls. Wu and Cheng [123] experimentally studied the effect of contact angle on heat transfer in microchannels by investigating flow inside silicon (hydrophobic) and silicon dioxide (hydrophilic) microchannels and showed a decrease in pressure drop and the Nusselt number on the order of 10% for the silicon channels compared to the silicon dioxide channels.

This work was followed by Rosengarten, Cooper-White, and Metcalf [158] who experimentally and analytical explored the effect of contact angle on liquid convective heat transfer in microchannels. They showed experimentally that the pressure drop

decreases relative to no-slip theory for flow above a crucial shear rate of approximately 10,000 s^{-1} and that this decrease is dependent on the contact angle [158]. They propose that the reduction in pressure loss decouples the fluid from the wall and results in a higher interfacial thermal resistance. This resulted in a decrease in convective heat transfer up to 10% that was more pronounced for the hydrophobic surface compared to laminar no-slip theory and the hydrophilic surfaces tested [158].

Other recent efforts have investigated the effect of slip flow in the laminar continuum mechanics region resulting from hydrophobic surfaces. Martin and Boyd [159] modeled a laminar boundary layer using slip boundary conditions for flow over a flat plate. Their model considers boundary layer effects for both rarefied gas flows and liquid flows approaching the continuum limit using a non-dimensional parameter that describes the behavior at the surface based on the slip velocity, K. For gas flow approaching the continuum limit, K is based on the Maxwell slip condition and is given by [159]:

$$\mathrm{K} = \frac{2 - \sigma_m}{\sigma_m} Kn_x Re_x^{1/2} \tag{3-1}$$

where σ_m is the tangential accommodation coefficient and Kn_x and Re_x are the Knudsen and Reynolds numbers based on flow direction x. For liquid flows that approach the continuum limit, K is based on the slip length and is given by [159]:

$$\mathrm{K} = \frac{\lambda}{x} Re_x^{1/2} \tag{3-2}$$

where, λ is the slip length. Using the non-dimensional surface behavior coefficient, the average Nusselt number can be calculated from [159]:

$$\overline{Nu_L} = 2Re_L^{1/2} K \int_{K(L)}^{\infty} \frac{dT'(0)}{K^2} dK \tag{3-3}$$

Plotting the results of Equation (3-3) and comparing them to the results for the no-slip value of the Nusselt number shows that the average heat transfer over a flat plate increases with slip. Using their modeling approach, they found that the slip conditions changes the boundary layer structure for a self-similar profile to a two-dimensional structure that generally leads to decreased overall drag, local increases in skin friction, thinner boundary layers, delayed transition to turbulence, and increased heat transfer at the wall when a thermal jump condition does not exist [159].

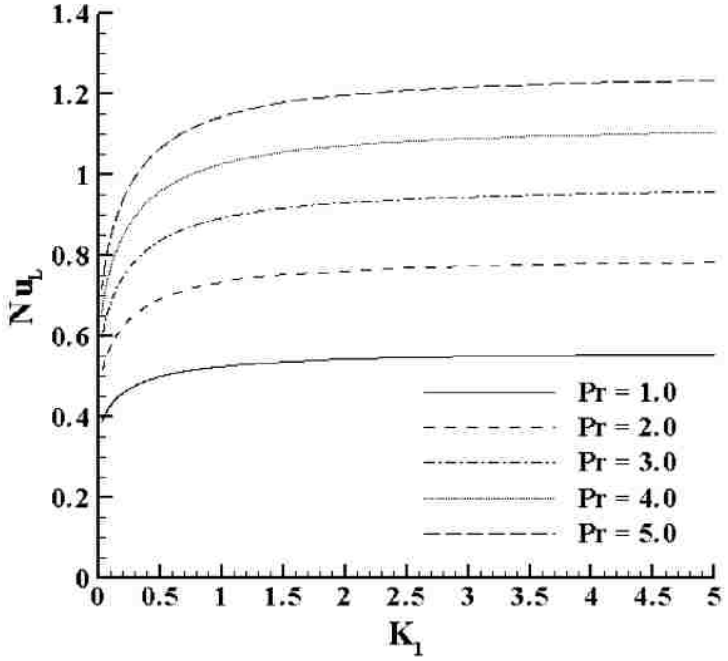

Figure 3-9: Average Nusselt number as a function of non-equilibrium for liquid flows [159].

Previous results focused on slip length and hydrophobic surfaces, Maynes et al. [63] were among the first to model the thermal transport in microchannels with superhydrophobic microridges. They used the commercial CFD code Fluent to evaluate the effects of cavity and ridge spacing fractions, ridge height, and Reynolds number on heat transport for microridges perpendicular to the flow and for a constant temperature boundary condition. They assumed an alternating no-slip boundary condition on the ridge surface, a shear-stress free boundary condition above the cavity, and an idealized flat meniscus shape over the cavity.

In general, their model showed thermal transport through the cavity interface was several orders of magnitude lower than at the liquid-solid interface, and also that there was "a steep decay in the relative heat flux with streamwise position from the leading edge of the microrib, associated with the growth of a new thermal boundary layer on each rib" [63]. Maynes et al. concluded that increasing the cavity length and the relative cavity/ridge length decreased heat transfer; however, they also concluded that the relative reduction in frictional pressure drop offset the relative reduction in heat transfer by comparing the ratio between the Nusselt number and the frictional pressure resistance and comparing it to the classical ratio [63].

$$F = \frac{\psi}{\psi_{NS}} = \frac{Nu}{fRe}\left(\frac{fRe}{Nu}\right)_{NS} \tag{3-4}$$

Using this efficiency factor, they found that for many of the cases studied the reduction in frictional drag outweighed the reduction in heat transfer and examples for various cases are shown in Figure 3-10.

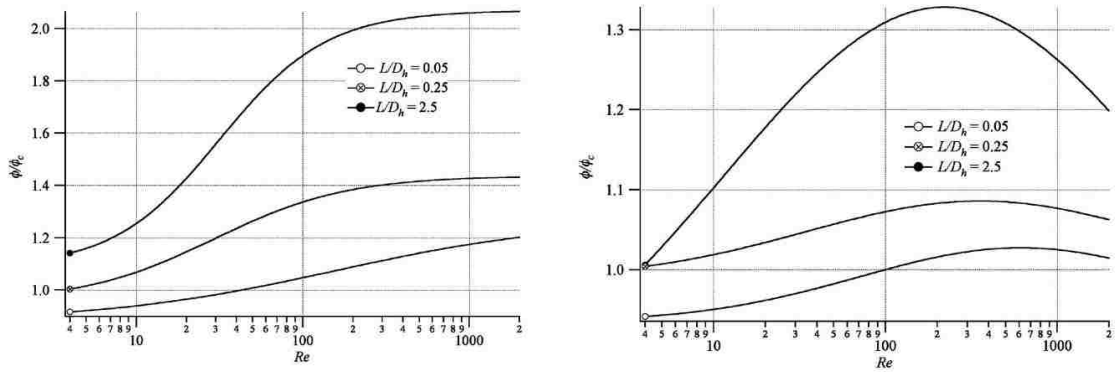

Figure 3-10: Variation of the hydrodynamic-thermal efficiency factor with Reynolds number for relatively cavity fractions of 0.98 (left) and 0.5 (right) for relative microridge/cavity lengths of and ridge height to width ratio of 2 [63].

Maynes et al. [64], [65] followed this work by examining the apparent temperature jump and thermal transport in channels for transverse and streamwise ridges with superhydrophobic walls under constant heat flux conditions. They presented a closed form solution using an infinite series expansion for the local Nusselt number and wall temperature. From their analysis they concluded [64], [65]:

1) Thermal transport through the vapor cavity is negligible compared to the metal surface because of the difference in thermal conductivity. In their example, they compare a metal surface with a thermal conductivity of 100 W/m-K, air with a thermal conductivity of 0.03 W/m-K, and a very small ridge fraction of 0.01. The result is a transport ratio on the order of 33, which clearly indicates that the metal ridges dominate thermal transport

2) The Nusselt number is strongly influenced by the cavity fraction, the periodicity of the cavity-ridge spacing with respect the channel hydraulic diameter, and the Peclet number

3) For transverse ridges:

    a. Increases in cavity fraction and the ridge/cavity length lead to decreases in the average Nusselt number

    b. Increases in the Peclet number increase the average Nusselt number

    c. For all parameters explored, the upper bound on the fully developed average Nusselt number corresponds to the limiting case scenario of classical laminar flow at constant heat flux.

4) For steramwise ridges:

    a. Higher cavity fractions lead to higher local heat transport above the ridges because of higher thermal gradients present, and conversely, the averaged Nusselt number over the cavity and ridge is reduced as a result of higher cavity fractions

    b. At small relative ridge/cavity size, the influence of the superhydrophobic surface goes to zero because the metal ridges dominate and approach the solid surface heat transport limit

    c. The thermal slip length is nearly identical to the hydrodynamic slip length.

Cowley, Maynes, and Crocket [61] furthered the analysis for the transverse ridge configuration under constant heat flux by examining the effective temperature jump length and the influence of axial conduction. They found that axial conduction is

significant especially for large relative channel widths, low Peclet numbers, and large cavity fractions. They define the temperature jump length as the ratio of the apparent temperature jump magnitude over the negative temperature gradient at the wall [61]:

$$\lambda_T = \frac{\Delta T_w}{\left(-\partial T/\partial y\right)} \tag{3-5}$$

Through multiple simulations, they found the thermal entry length to be consistent with the expression $(x_{fd,T}/D_h) \approx 0.05RePr$ [61]. Their results were consistent with the previous work by Maynes and Crocket in that they found that the local heat transfer above the ridge was increased compared to the classical Nusselt number but that the overall averaged value above the ridges and cavities was decreased. They also concluded that the effect of axial conduction was to smooth the local Nusselt number and the non-dimensional wall temperature profiles, which causes the averaged Nusselt number to approach the classical channel value [61].

In parallel to the work of Maynes et al., Enright et al. [59] evaluated friction factors and Nusselt numbers in microchannels with superhydrophobic walls under constant heat flux boundary conditions. They studied two possible boundary states: 1) single phase fluid flow following Navier's slip model at the wall and 2) fluid flow with a recirculating layer separating the fluid from the wall. For the first case, they analytically determined the Nusselt number for Navier slip at constant flux to be [59]:

$$Nu = \frac{140\left(1 + 6\frac{\lambda}{H}\right)^2}{\left(17 + 168\frac{\lambda}{H} + 420\left(\frac{\lambda}{H}\right)^2\right)} \tag{3-6}$$

where λ/H is the non-dimensional slip length. This expression provides the no-slip Nusselt number of 8.2353 for $\lambda = 0$ and approaches the plug flow Nusselt number of 12 as λ/h approaches infinity. For boundary interactions that are consistent with Navier slip, the Nusselt number increases with λ/H and approaches the plug flow condition.

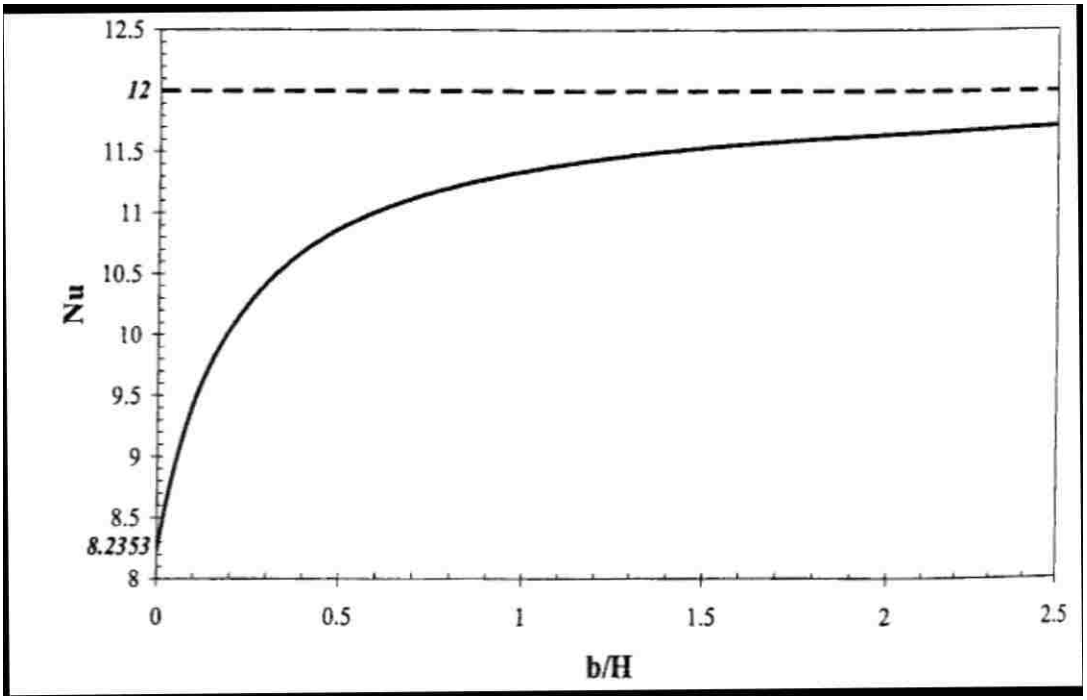

Figure 3-11: Nusselt number as a function of slip length to channel height for a constant heat flux wall condition [59].

For the second scenario that was studied, Enright et al. expanded the model to include a no-slip condition at the solid boundary interface, "while the no-slip condition and continuity of the tangential shear stress are assumed to hold at the air/water interface"

[59]. They also assumed that the flow in the air layer could be described by continuum mechanics; however, they do note that this was highly dependent on various conditions and that flow conditions should first be determined from the Knudsen number. Altering the boundary conditions for the Navier-Stokes equations to account for molecular slip, the derived the slip coefficient is [59]:

$$\lambda = \frac{\mathrm{t}_{air}\mu_{water}}{4\mu_{air}} \tag{3-7}$$

where, t_{air} is the thickness of the air layer and μ_{water} and μ_{air} are the viscosities of water and air, respectively. Substituting this slip definition, yields a relationship for the Poiseuille number [59]:

$$fRe = \frac{192\mu_{air}}{2\mu_{air} + 3\left(\frac{t}{H}\right)\mu_{air}} \tag{3-8}$$

This basic model accounts for the thickness of the air layer and the ratio between the air and water viscosities, but it excludes effects from surface roughness, feature spacing, thermal effects of the air layer, and the possibility for thermal jump conditions at the air/water interface.

Enright et al. [62] further enhanced their model to include temperature jump as well as hydrodynamic slip for the constant heat flux condition. Temperature jump is a known characteristic for rarefied gas flow and characterizes the process of incomplete thermal coupling between the fluid and the boundary surface and is captured by the temperature slip length defined as:

$$\bar{T}_{SL} - \bar{T}_w = \lambda_T \frac{dT}{dn}\Big|_{wall} \tag{3-9}$$

where, $\bar{T}_{SL}$ is the mean temperature of the solid-liquid portion of the composite interface, $\bar{T}_w$ is the mean temperature of the composite interface, and λ_T is the apparent temperature slip length. This effect is a Kapitsa resistance caused by the nature of molecular phenomenon that enable hydrodynamic slip at the composite boundary [62]. The reduction in solid-liquid interfacial area in conjunction with the introduction of a low viscosity, low thermal conductivity gas phase that enables hydrodynamic slip also enables thermal slip and a resulting reduction in heat transfer performance [62]. Solving the governing equations, yields the following results for the Poiseuille and Nusselt numbers [62]:

$$fRe = \frac{196\left(1 + 2\bar{\lambda}\right)}{1 + 8\bar{\lambda} + 12\bar{\lambda}^2} \tag{3-10}$$

$$Nu = \frac{140(1 + 6\lambda)^2}{17 + 168\bar{\lambda} + 420\bar{\lambda}^2 + 70\bar{\lambda}_T + 840\bar{\lambda}_T\bar{\lambda} + 2520\bar{\lambda}_T\bar{\lambda}^2} \tag{3-11}$$

where, $\bar{\lambda}$ is the dimensionless slip length, λ/H. Equation (3-11) indicates that heat transfer increases with hydrodynamic slip but decreases with thermal slip and is consistent with previous observations of molecular slip flow heat transfer [62].

For flow rates near the composite interface, the flow approached Stokes flow and the creeping limit as the Peclet number approaches zero, which indicates the local heat transport was largely diffusive. Enright et al. [62] considered the effect of a point heat source in Stokes flow, by satisfying the Laplace equation, they found that the thermal slip

length was on the same order as the hydrodynamic slip length. In addition, since heat transfer was diffusion dominated, there was a thermal spreading resistance at the solid-liquid interface that was connected to the slip phenomenon. For flow over streamwise ridges, this connection indicated that the hydrodynamic slip length was mathematically equivalent to the thermal spreading resistance subject to a Dirchlet boundary conditions because the pressure gradient was orthogonal to the velocity gradients such that the Stokes equation could be separated into the Laplace equation and a constant pressure term [62]. Using the thermal spreading resistance obtained by Vezirouglu and Chandra [160] and the hydrodynamic slip length derived from Philip [153], [161], an expression for the thermal slip length for isothermal wall condition with streamwise ridges was derived [62]:

$$\frac{\lambda_T}{s} = \frac{1}{\pi} \ln \left[\sec \left(\frac{\pi}{2} (1 - \phi_s) \right) \right] \tag{3-12}$$

where ϕ_s is the composite interface solid fraction and s is the pitch spacing. For a Neumann boundary condition the thermal slip was [62]:

$$\frac{\lambda_T}{s} = \frac{1}{\pi^3 \phi^2} \sum_{n=1}^{\infty} \frac{\sin^2(n\pi\phi)}{n^3} \tag{3-13}$$

From their numerical model, Enright et al. found that for streamwise ridges with a thermal slip length 1.05 times the hydrodynamic slip length, the efficiency factor defined by Maynes et al. increased monotonically to a value of 1.39 at large hydrodynamic slip lengths. They also noted the maximum performance improvement of 17% for streamwise

ridges over posts occurred when the slip length was 0.132, and the efficiency factor was 1.26. The relationship of the efficiency factor to the thermal hydrodynamic slip lengths indicate that larger enhancements were possible by independently reducing the thermal slip length [62]. The relationships between the hydrodynamic slip length, thermal slip length, Nusselt number, and efficiency factor are shown on the figures below.

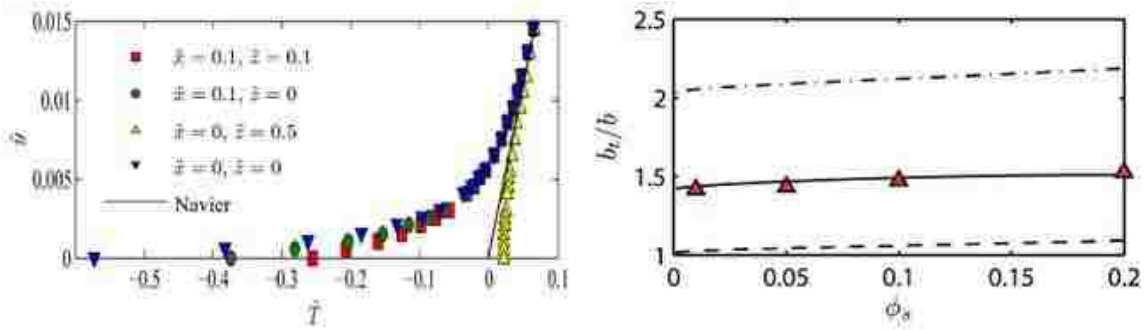

Figure 3-12: The dimensionless temperature profile for a solid fraction of 0.01 magnified near the surface (left) and the relationship between the thermal and hydraulic slip lengths (right) where the numerical data (triangles) are compared to the analytical prediction for pillars (solid line), streamwise ridges (dashed line), and transverse ridges (dashed-dotted line) [62].

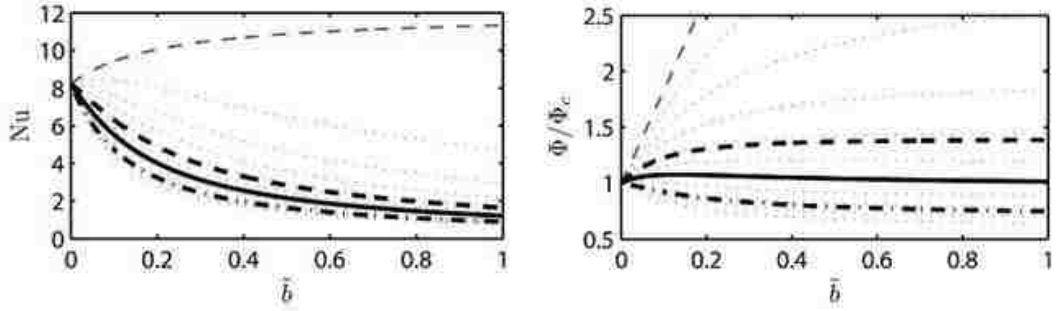

Figure 3-13: The influence of hydraulic slip on the Nusselt number (left) and efficiency factor (right) for pillars (solid curve - b_T=1.5b), streamwise ridges (dashed curve – b_T=1.05b), transverse ridges (dotted-dashed curve – b_T=2.1b) for Stokes flow. Also shown are the limit of bT=0 (blue dashed curve and the range of thermal slip between 0 and 2.5b in increments of 0.25b_T (light dotted curves) [62].

Finally, Enright et al. [62] determined that streamwise ridges provide the best performance in terms of efficiency factor because of the small ratio between the hydrodynamic slip and thermal slip ($b_T/b \approx 1$). Transverse ridges have the worst performance because the hydrodynamic slip length for transverse ridges half the slip length of streamwise ridges in the Stokes flow limit, which results in a slip ratio closer to 2. The performance of microposts is in the middle with a slip ratio of 1.5 [62].

More recently, Cheng, Xu, and Sui [60] performed a detailed numerical study for drag reduction and heat transfer enhancement in microchannels with superhydrophobic surfaces that included no-slip at the solid boundary, shear free at the vapor boundary, cavity fraction, and periodic surface patterning (square posts, square holes, longitudinal ridges, and horizontal ridges. However unlike the work of Maynes et al. and Enright et al., their work did not consider thermal slip at the boundary. For their approach, the governing equations were discretized using a finite volume method. A central difference scheme and a stability-guaranteed second order difference scheme were used for the diffusion and convective terms, respectively [60]. The numerical model was validated against the classical parallel-plate, no-slip values for the Poiseuille and Nusselt numbers for constant temperature boundary condition as well as the previous analytical work for frictional performance by Philip [153], [161] and Teo and Khoo [162] with good agreement [60].

Using their validated numerical model, they explored the frictional and thermal performance of the four patterned surface cases noted above at Reynolds's numbers from 1 to 1000. First, they investigate frictional performance and the effects of the shear-free fractions of the various surface patterns and found that the longitudinal ridges had the lowest frictional performance and was essentially constant over the range of Reynolds number evaluated. They attributed this to the fact that the longitudinal ridges were the only pattern that did not "experience the periodic acceleration and deceleration at the trailing edge and leading edge of no-slip walls" [60]. This was true for all cases studied except for very high cavity fractions on the order of 0.95 and Reynolds numbers less than 100 at which point the square post pattern provided the best results. The influence of cavity fraction on Poiseuille number at a Reynolds number of 100 as well as the influence of Reynolds number on the Poiseuille number for cavity fractions of 0.5 and 0.95 are shown in Figure 3-14. The other item of note is that for Reynolds numbers less than 20, the flow inside the microchannels can be regarded as viscous Stokes flow where viscous effects dominate inertial effects and the Poiseuille number is constant [60].

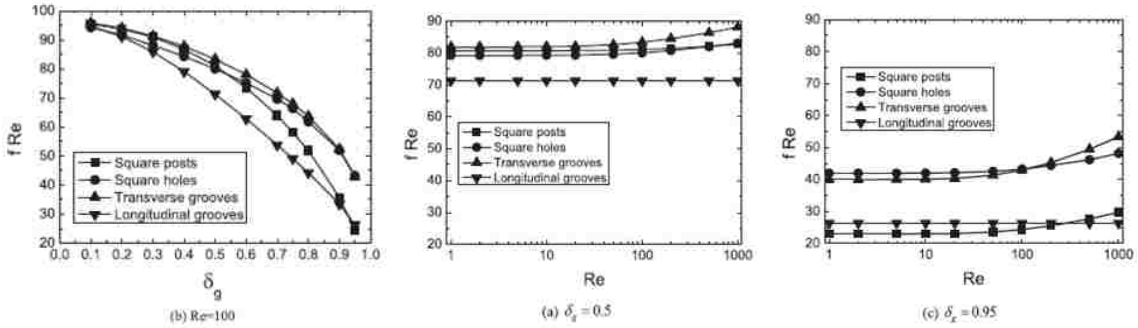

Figure 3-14: Influence of cavity fraction on Poiseuille number (left) and the influence of Reynolds number on Poiseuille number at cavity fractions of 0.5 (center) and 0.95 (right) [60].

As for heat transfer performance, Cheng et al. [60] found that the Nusselt number decreased with increasing cavity fraction with a larger impact at larger cavity fractions. This was likely because of the drastic reduction in liquid-solid contact area. Their model also predicted that for all cases the Nusselt number was less than the classical solution with all but the longitudinal grooves approaching the classical value at higher Reynolds numbers. The longitudinal grooves were the worst performing pattern. The lack of accelerating-decelerating flow in the shear-free sections was attributed to the poor performance. In general, Cheng et al. reported the Nusselt number generally increases with Reynolds number with a change is slope from viscous Stokes flow to inertial flow. The exception was the longitudinal ridges, which remained constant above Re = 20. These results were attributed to a thinning of the boundary layer, which increased the thermal gradient. The relationships between the Nusselt number, cavity fraction, and Reynolds number are shown in Figure 3-15 [60].

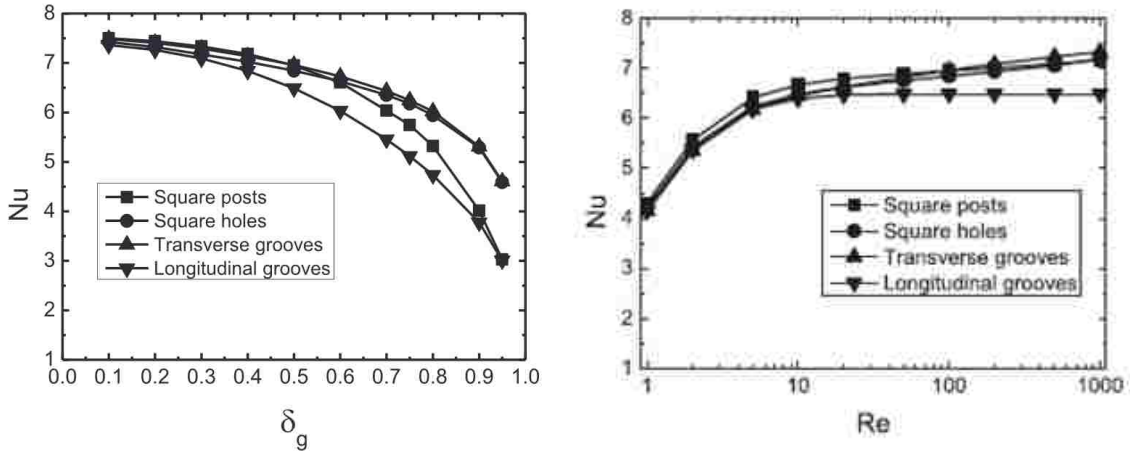

Figure 3-15: The influence of cavity fraction (left) and Reynolds number (right) on the Nusselt number for various micropattern geometries [60].

Finally, Cheng et al. followed a similar path as Maynes et al. and examined the combined hydrodynamic and thermal effects and found that despite the overall reduction in Nusselt number for all cases examined the improvement in Poiseuille number outweighed this reduction and the combined efficiency factor increased for all cases compared to classical laminar flow behavior at Reynolds number equal to 100 and 1000. At Reynolds number of 100, the longitudinal ridges outperformed the other three patterns, and the results for the effect of cavity fraction and Reynolds number are shown in Figure 3-16 [60].

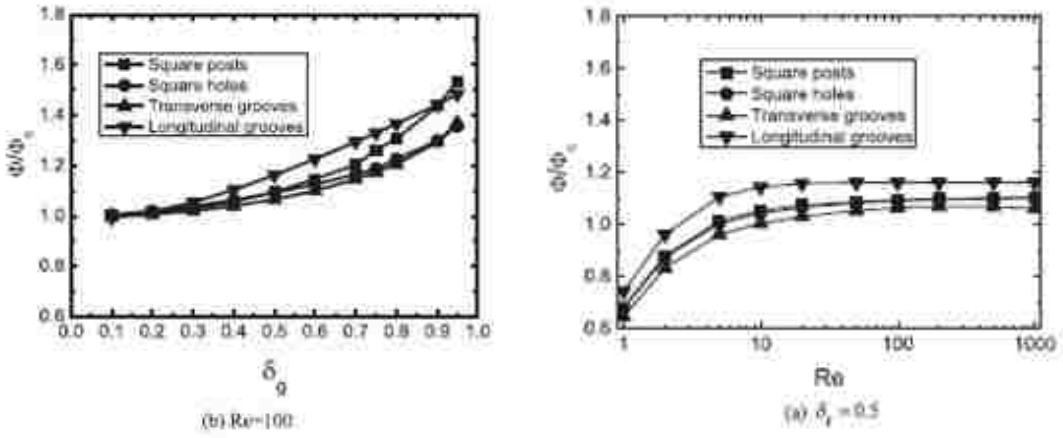

Figure 3-16: Influence of cavity fraction (left) and Reynolds number (right) on the hydrodynamic-thermal efficiency factor [60].

Moreira and Bandaru [66] studied the effect of substrate thermal conductivity for flow in microchannels with transverse ridges using an effective medium approach to model the reduced conductivity caused the by the air interface as well as the substrate. Their model accounts for hydrodynamic slip, conductivity of the air layer, and cavity ratio, but it does not consider thermal slip at the boundary. From their analysis, they conclude that

the Nusselt number initially increases with slip; however, they note a subtle interplay in that the temperature difference between the mean temperature and the wall decreases on the order of 20%, but the temperature gradient decreases approximately 10% leading to an increase in the Nusselt number [60]. More importantly, Moreira and Bandaru showed that the conductivity of the substrate has a significant impact on the overall thermal transport of the system and that low thermal conductivity substrates have a dramatic reduction in the overall heat transfer performance regardless of air fraction compared to high conductivity substrates [60].

Whereas Maynes et al., Enright et al., Cheng et al., and Moreira et al. studied slip effects for Poiseuille flow, Lam et al. [163] extensively studied the effects of hydrodynamic and thermal slip on the Nusselt number for thermally developing Couette flow. They argue that "molecular slip in rarefied gasses and apparent slip on superhydrophobic surfaces are equivalent mathematically under many conditions… [and] the phenomenon of slip can be represented as a surface effect when the ratio of the pitch of the surface structure to the height of the channel is small" [164], [163]. They also point out that Sparrow and Lin [165] showed that hydrodynamic slip in gas flow increases the Nusselt number and thermal slip decreases it, but the total effect is a net reduction. Using the developed temperature and Nusselt number expression from Sestak and Rieger [166], they analyzed the entrance behavior for four sets of thermal boundary conditions for Couette flow in the presence of slip: no-slip at both surfaces, slip at the moving surface only, slip at the stationary surface only, and slip at both surfaces. Through their

mathematical analysis, they found that hydrodynamic slip has no mathematical implications on the moving surface and thus no impact on heat transfer. For the stationary surface, hydrodynamic slip plays a much bigger role by increasing heat transfer at the stationary surface, decreasing it at the moving surface, and causing a net increase in total heat transfer, which is different from Poiseuille flow conditions studied by Maynes et al. and Enright et al. Finally, Lam et al. state that for all cases studied the presence of thermal slip reduces the Nusselt number from the classical solution [163].

For the most part only analytical and numerical studies have been conducted to investigate the effects of slip, surface patterning, and superhydrophobic surfaces on heat transfer. Hsieh and Lin [167] conducted one of the few recent, detailed experimental studies of convective heat transfer in liquid microchannels with hydrophobic and hydrophilic surfaces using μPIV and micro laser-induced fluorescence (μLIF) for flow and temperature visualization. In their experiments, the test samples consisted of PDMS microchannels whose hydrophilicity and hydrophobicity was modified using energetic surface treatments including UV radiation and plasma exposure. The rectangular microchannels had an aspect ratio (H/w) of 0.56 and hydraulic diameter of 129 μm at Reynolds numbers between 5 and 240. Measurements were taken under isothermal (273K) and multiple isoflux conditions for DI water, methanol, and 50/50 mixture of methanol. The results from their experiments indicated that the hydrophobic microchannels average 8 - 10% reduction in friction factor and average heat transfer coefficient compared to the untreated and hydrophilic channels. They also concluded

that the constant wall temperature and wall heat flux heat transfer coefficients were constant and independent of the Peclet number and heat flux input (for the constant heat flux cases) [167]. The results of Hsieh and Lin are compared to the results of other experimental studies for microchannels with hydrophilic and hydrophobic channels in the table below.

Table 3-3: Summary of laminar thermally developed and developing correlations of the Nusselt number for microchannels with hydrophilic and hydrophobic surface coatings [167].

Reference	Parameters	Correlation	Condition and restrictions
W. Qu et al. [10]	D = 168.9 μm L = 30 mm	Laminar and thermally fully developed flow $\overline{Nu} = 1 \sim 2$ ($100 < Re < 400$), $\overline{Nu} = 2$ ($400 < Re < 1500$)	Silicon trapezoidal microchannel (hydrophobic)
Incropera and DeWitt [15]		$\overline{Nu} = 4.36$ (constant heat flux) $\overline{Nu} = 3.66$ (constant wall temperature)	Laminar and thermally fully developed (tube channel)
X.F. Peng et al. [16]	D = 133–367 μm L = 50 mm	Laminar and thermally fully developed flow $\overline{Nu} = C_{H,I} Re^{0.62} Pr^{0.33}$, $50 < Re < 4000$	$C_{H,I}$ depended on aspect ratio $0.01 < C_{H,I} < 0.058$
X.F. Peng et al. [17]	D = 133–343 μm L = 50 mm	Laminar and thermally fully developed flow $\overline{Nu} = 0.117\ (D/W_c)^{0.81}\ (H/W)^{-0.79} Re^{0.62}\ Pr^{0.33}$, $50 < Re < 4000$	W_c: center-to-center distance of microchannels
Wu and Cheng [18]	D = 110 μm L = 34 mm	Laminar and thermally fully developed flow $\overline{Nu} = 0.5 \sim 2.6$ (hydrophilic), $50 < Re < 600$ $\overline{Nu} = 0.5 \sim 2.3$ (hydrophobic), $50 < Re < 600$	Silicon trapezoidal microchannel with (hydrophilic)/ without (hydrophobic) SiO_2
L. Zhuo et al. [19]	D = 102 μm L = 30.5 mm	Laminar and thermally fully developed flow $\overline{Nu} = 0.8 \sim 2.35$, $25 < Re < 450$	Silicon trapezoidal microchannel (hydrophobic)
P. X. Jiang et al. [20]	W = 200 μm H = 600 μm D = 300 μm L = 20 mm	Laminar and thermally developing flow Without micro-porous: $Nu = 0.52\ (Gz^{-1})^{-0.62}$, $Gz^{-1} \leqslant 0.05$ $Nu = 2.02\ (Gz^{-1})^{-0.31}$, $Gz^{-1} > 0.05$ (thermally fully developed) With micro-porous: $Nu = 1.97\ (Gz^{-1})^{-0.72}$, $Gz^{-1} < 0.05$	Rectangular microchannel with/without micro-porous (one-sided heating)
S. Shen et al. [21]	W = 300 μm H = 800 μm L = 50 mm	Laminar and thermally developing flow $Nu = 0.505\ (Gz^{-1})^{-0.22}$, $0.0375 < Gz^{-1} < 0.14$ $Nu = 2.18$, $Gz^{-1} > 0.14$ (thermally fully developed)	Rectangular microchannel (one-sided heating)
Present study	W = 180 μm H = 100 μm D = 129 μm L = 20 mm Pe = 20 ~ 3300	Laminar and thermally fully developed flow Hydrophilic microchannel:constant heat flux: $\overline{Nu} = 2.62$ Constant wall temperature: $\overline{Nu} = 2.49$ Hydrophobic microchannel: constant heat flux: $\overline{Nu} = 2.42$ Laminar and thermally developing flow $Nu = 0.968\ (Gz^{-1})^{-0.36}$, $Gz^{-1} \leqslant 0.063$ $Nu = 2.62$, $Gz^{-1} > 0.063$ (thermally fully developed)	A rectangular microchannel array(hydrophilic and hydrophobic) Aspect ratio: 0.56

3.4 Summary and Conclusions

Superhydrophobic surfaces, those that combine hydrophobic coatings with patterned microscale features to achieve surface roughness, have been shown to achieve an effective slip at the boundary because of the shear-free vapor-fluid interface that forms

between the micro-features. This approach maximizes the contact angle while minimizing the contact angle hysteresis, which is the critical parameter for determine the dynamics of a droplet on a surface. The key to achieving this state is to ensure that the fluid maintains a pure Cassie state in that the fluid only contacts the top surface of the micro-features by properly balancing the surface tension with the feature spacing and the fluid pressure. In addition, the three-phase contact line must be optimized to minimize its length while maintaining the highest possible continuity in the flow direction to maximize the performance of the system. Using these parameters, drag reductions of 20% to 40% for laminar flow and 50% for turbulent flow have been achieved. In addition, effective slip lengths as large as 400 μm have been measured.

For the most part, the thermal effects of slip flow for superhydrophobic surfaces have only been considered from an analytical and numerical standpoint. Using various approaches and models, most authors agree that for cases where only hydrodynamic slip occurs at the wall, superhydrophobic surfaces should increase heat transfer. However, if both hydraulic and thermal slip occur at the wall, then heat transfer performance will be hindered. The degree to which superhydrophobic surfaces will help or hurt heat transfer in the various respective cases is still a point of disagreement and largely depends on the assumptions that went into the model. There is some limited experimental data for hydrophobic and hydrophilic surfaces, but there is no experimental data in the literature for superhydrophobic surfaces.

Chapter 4

Slip Flow Numerical Model

The majority of this chapter is based on the paper for the 2012 AIAA Aerospace Sciences conference and has been updated based on changes to the experimental setup and because of numerical stability issues with the original Crank-Nicolson approach under some flow and node configurations [89]. The original paper is included as Appendix A.

4.1 Numerical Analysis Method

The advantage of micropatterned superhydrophobic surfaces for fluid applications, especially microfluidic systems, is drag reduction and thus reduced pumping power required for these systems. However, the question that remains is the effect the slip boundary condition has on the convective heat transfer for cooling applications. The slip boundary condition should locally enhance heat transfer because the non-zero velocity at the interface enables both convection and fluid conduction near the surface such that heat is transported away from the surface in a more efficient manner. However, the

decoupling of the fluid and the solid surface resulting from slip could cause a temperature jump and thermal slip condition as seen in gas dynamics. In addition, micropatterning the surface reduces the solid-liquid contact area, which reduces heat transfer. Identifying if thermal slip occurs with hydrodynamic slip and whether or not slip effects are more dominant than contact area reduction is key to understanding the potential heat transfer enhancement that can be achieved using superhydrophobic coatings. This chapter seeks to take the first step by evaluating the effect that slip flow has on heat transfer for flow between parallel plates. The effect of heat transfer area reduction is not considered.

For flow between parallel plates, the velocity profile for the three possible boundary condition cases was determined analytically: 1) no-slip, 2) slip on one boundary only, and 3) slip on both boundaries. The input parameters and problem setup are shown in Figure 4-1. The test section consisted of an adiabatic entry region to provide hydrodynamically fully developed flow prior to entry into the heated section.

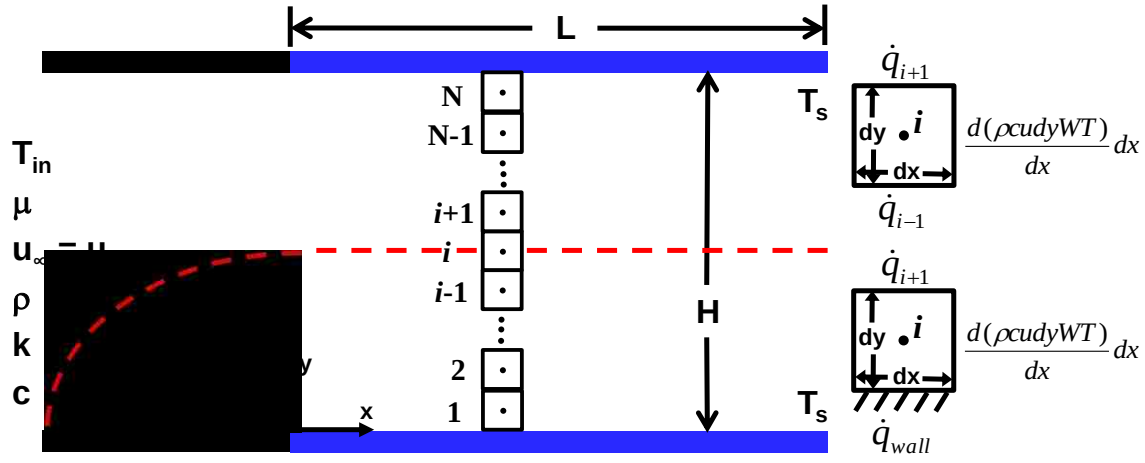

Figure 4-1: Parallel plates setup and inputs for the analytical analysis with an unheated entry section to allow for hydrodynamically, fully developed flow before entry into the heated length.

The general equation for conservation of momentum is:

$$\rho\left[\frac{\partial u}{\partial t}+u_x\frac{\partial u}{\partial x}+u_y\frac{\partial u}{\partial y}\right]=-\frac{dP}{dx}+\mu\left[\frac{\partial^2 u}{\partial y^2}+\frac{\partial^2 u}{\partial x^2}\right]+\rho g \tag{4-1}$$

where ρ is the density of the fluid, u_x is the velocity in the x-direction, u_y is the velocity in the y-direction, t is time, P is pressure, μ is the dynamic viscosity of the fluid, and g is the acceleration caused by gravity. Assuming steady state, horizontal, fully developed flow, constant cross section, and boundary layer simplifications, the conservation of momentum equation reduces to:

$$\left[\frac{\partial^2 u}{\partial y^2}\right]=\frac{1}{\mu}\frac{dP}{dx} \tag{4-2}$$

Integrating twice yields:

$$u=\frac{1}{2\mu}\frac{dP}{dx}y^2+C_1y+C_2 \tag{4-3}$$

Applying the boundary conditions for the three cases and solving for the constants yields the following equations:

Case 1: u = 0 at y = 0, y = H

$$u_{no\ slip}=6u_m\left[\frac{y}{H}-\left(\frac{y}{H}\right)^2\right] \tag{4-4}$$

Case 2: u = u_{slip} at y = 0; u = 0 at y = H

$$u_{slip\ BC1}=6u_m\left[\frac{y}{H}-\left(\frac{y}{H}\right)^2\right]-u_{slip}\left[4\left(\frac{y}{H}\right)-3\left(\frac{y}{H}\right)^2-1\right] \tag{4-5}$$

Case 3: u = u_s at y = 0, y = H

$$u_{slip\ BC2} = 6u_m\left[\frac{y}{H} - \left(\frac{y}{H}\right)^2\right] - 6u_{slip}\left[\frac{y}{H} - \left(\frac{y}{H}\right)^2\right] + u_{slip} \tag{4-6}$$

where u_m is the average velocity at x, H is the distance between the plates, and u_{slip} is the slip velocity at the boundary. For the special case of plug flow, Case 3 reduces to:

$$\mathrm{u}_{plug} = u_m \tag{4-7}$$

For each of the three boundary conditions, u_m is:

Case 1: u = 0 at y = 0, y = H

$$u_m = -\frac{\partial P}{\partial x}\frac{H^2}{12\mu} \tag{4-8}$$

Case 2: u = u_s at y = 0; u = 0 at y = H

$$u_m = -\frac{\partial P}{\partial x}\frac{H^2}{12\mu} + \frac{1}{2}u_{slip} \tag{4-9}$$

Case 3: u = u_s at y = 0, y = H

$$u_m = -\frac{\partial P}{\partial x}\frac{H^2}{12\mu} + u_{slip} \tag{4-10}$$

The general thermal energy balance equation is:

$$\rho c\left[\frac{\partial \mathrm{T}}{\partial \mathrm{t}} + \mathrm{u}\frac{\partial \mathrm{T}}{\partial \mathrm{x}} + \mathrm{v}\frac{\partial \mathrm{T}}{\partial \mathrm{y}}\right] = \mathrm{k}\left[\frac{\partial^2 \mathrm{T}}{\partial \mathrm{x}^2} + \frac{\partial^2 \mathrm{T}}{\partial \mathrm{y}^2}\right] + \dot{\mathrm{g}}_{\mathrm{v}}''' \tag{4-11}$$

where c is the specific heat, T is the temperature, k is the thermal conductivity, and $\dot{g}_v'''$ is:

$$\dot{g}_v''' = \mu\left[\left(\frac{\partial u}{\partial x}+\frac{\partial u}{\partial y}\right)^2 + 2\left[\left(\frac{\partial u}{\partial x}\right)^2 + \left(\frac{\partial u}{\partial y}\right)^2\right]\right] \quad (4\text{-}12)$$

Assuming steady state; hydrodynamically, fully developed flow; axial conduction is small compared to lateral conduction i.e. Peclet number is large; and viscous dissipation is small i.e Brinkman number is small, the thermal energy balance equation reduces to:

$$\rho c\left[u\frac{\partial T}{\partial x}\right] = k\left[\frac{\partial^2 T}{\partial y^2}\right] \quad (4\text{-}13)$$

To solve the temperature equation for a finite difference numerical approximation, the state equations are solved by assigning a control volume around each node. The size of the control volume is based on the node density in the y-direction, and the size of the control volume is differentially small in the x-direction (dx). The energy balance for each node is based on conduction through the fluid from adjacent nodes in the y-direction and the energy transported by the fluid entering a x and exiting at x + dx. Solving for the energy balance at each node yields the follow equations [88]:

Node 1 (bottom):

$$\frac{\partial T_1}{\partial x} = \frac{k}{\rho c u_1 \Delta y^2}(T_2 - 3T_1 + 2T_s) \quad (4\text{-}14)$$

Nodes 2 through N-1:

$$\frac{\partial T_i}{\partial x} = \frac{k}{\rho c u_i \Delta y^2}(T_{i-1} - 2T_i + T_{i+1}) \quad (4\text{-}15)$$

Node N (top):

$$\frac{\partial \mathrm{T_N}}{\partial \mathrm{x}} = \frac{\mathrm{k}}{\rho \mathrm{c} \mathrm{u_N} \Delta \mathrm{y}^2} (\mathrm{T_{N-1}} - 3\mathrm{T_N} + 2\mathrm{T_s}) \quad (4\text{-}16)$$

The Crank-Nicolson approach was selected because it is an implicit, second-order method that is unconditionally stable. The method solves each integration step using the rate of change estimate based on the average value at the beginning and end of each length step [88]. Since the approach is implicit, the formula for taking a step is [88]:

$$T_{1,j+1} = T_{i,j} + \left[\left(\frac{dT}{dx} \right)_{T=T_{i,j}, x=x_j} + \left(\frac{dT}{dx} \right)_{T=T_{i,j+1}, x=x_{j+1}} \right] \frac{\Delta x}{2} \text{ for } i = 1 \ldots N \quad (4\text{-}17)$$

Substituting Equations (4-14), (4-15), and (4-16) into Equation (4-17) yields the series of equations to be solved using the Crank-Nicolson approach [88]:

Node 1 (bottom): (4-18)

$$T_{1,j+1} = T_{1,j} + \frac{\mathrm{k}}{\rho \mathrm{c} \mathrm{u_1} \Delta \mathrm{y}^2} \left[\left(\mathrm{T_{2,j}} - 3\mathrm{T_{1,j}} + 2\mathrm{T_s} \right) + \left(\mathrm{T_{2,j+1}} - 3\mathrm{T_{1,j+1}} + 2\mathrm{T_s} \right) \right] \frac{\Delta x}{2}$$

Nodes 2 through N-1: (4-19)

$$T_{i,j+1} = T_{i,j} + \frac{\mathrm{k}}{\rho \mathrm{c} \mathrm{u_1} \Delta \mathrm{y}^2} \left[\left(\mathrm{T_{i+1,j}} - 2\mathrm{T_{i,j}} + \mathrm{T_{i-1,j}} \right) + \left(\mathrm{T_{i+1,j+1}} - 2\mathrm{T_{i,j+1}} + \mathrm{T_{i-1,j+1}} \right) \right] \frac{\Delta x}{2}$$

Node N (top): (4-20)

$$T_{N,j+1} = T_{N,j} + \frac{\mathrm{k}}{\rho \mathrm{c} \mathrm{u_1} \Delta \mathrm{y}^2} \left[\left(\mathrm{T_{N-1,j}} - 3\mathrm{T_{N,j}} + 2\mathrm{T_s} \right) + \left(\mathrm{T_{N-1,j+1}} - 3\mathrm{T_{N,j+1}} + 2\mathrm{T_s} \right) \right] \frac{\Delta x}{2}$$

The series of equations are then put into matrix form and solved. To accomplish this, a program was written in Matlab, which is included in Appendix B. There is one caution that must be considered when using the Crank-Nicolson approach and that is the solution at the wall can oscillate if the step size ratio is too large, thus it is important to balance the mesh density for an accurate solution with computation time [88]. The analysis configuration parameters are summarized in Table 4-1, and

Table 4-2 lists the parameters that were normalized in the analysis.

Table 4-1: Configuration for the Poiseuille flow parallel plate configuration.

Parameter	*Symbol*	*Value*	*Units*
Channel height	H	0.004	m
Heated channel length	l	0.152	m
Channel width	w	0.035	m
Inlet temperature	T_{in}	393.2	K
Wall temperature	T_w	273.15	K

Table 4-2: Normalized parameters.

Parameter	*Symbol*	*Equation*
Channel height	$\hat{h} = \frac{y}{H}$	(4-21)
Slip length	$\hat{\lambda} = \frac{2\lambda}{H}$	(4-22)
Flow velocity	$\hat{u} = \frac{u}{u_m}$	(4-23)
Meant temperature	$T_m = \frac{1}{Hu_m}\int_0^H uTdy$	(4-24)
Non-dimensional temperature	$\hat{\theta} = \frac{T - T_S}{T_m - T_S}$	(4-25)

To test the dependence of the accuracy of the solution with respect to node density, the Crank-Nicolson model was run at multiple node spacing in the y-direction, and the

temperature of the node closest to the wall was plotted. Node space in the y-direction was increased by increments of 50 while the x-direction node spacing was maintained at 100,000 nodes. The results are shown on Figure 4-2 and clearly show that a minimum of 101 nodes are required to achieve results with acceptable accuracy. It can also be seen in the figure that at 151 nodes, the first node starts to oscillate for the first few positions in the x-direction. As noted, this is a known problem with the Crank-Nicolson approach. Depending on the node density in the x-direction and y-direction, the temperature oscillation can extend significantly in the x-direction as shown in Figure 4-3 for a node density in the y-direction of 101 and an x-direction node density of 10,000.

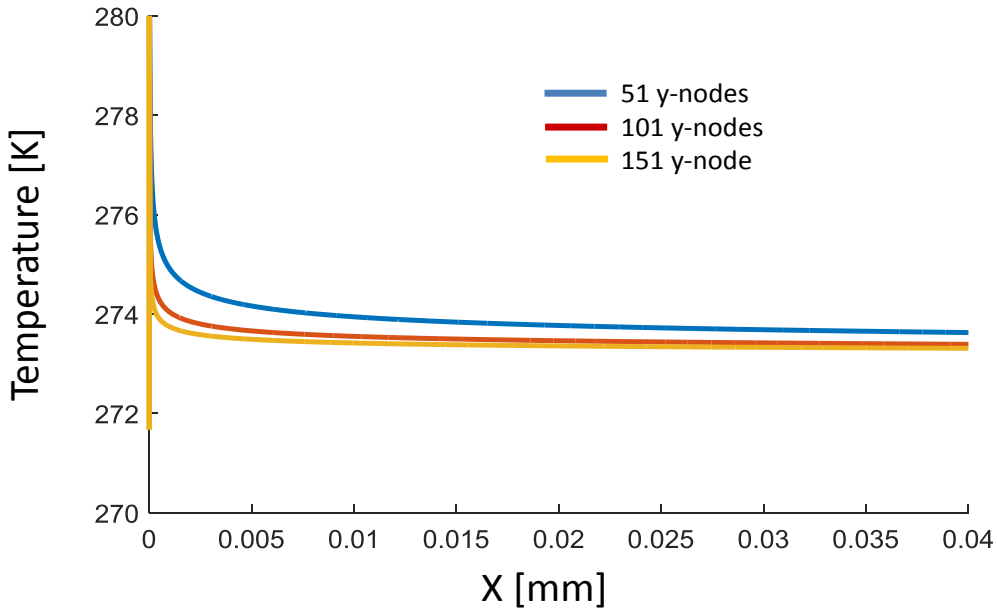

Figure 4-2: Plot of the effect of increasing node density in the y-direction on the first node closes to the wall using the Crank-Nicolson method. The node density in the x-direction was kept constant at 100,000 and the flow rate was 60 mL/min.

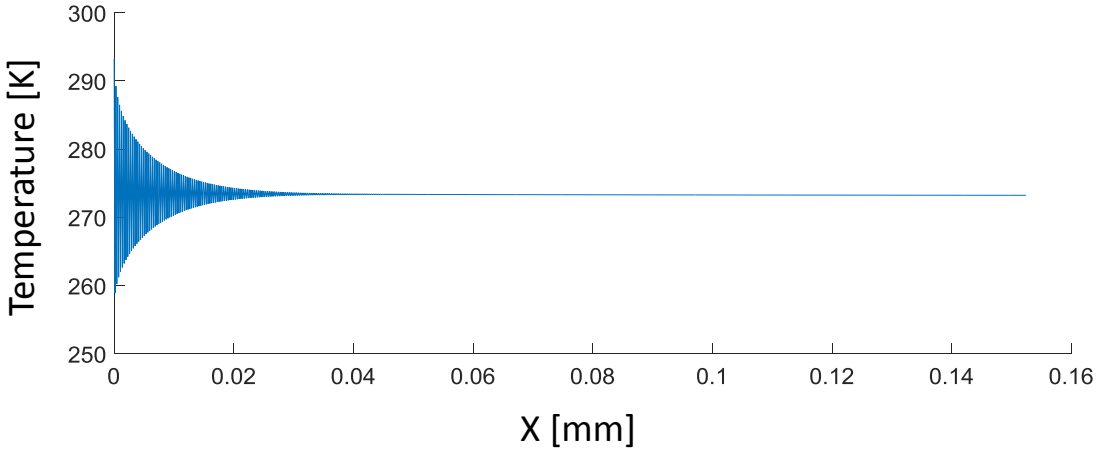

Figure 4-3: Example of temperature oscillation for the first node using the Crank-Nicolson approach with 101 nodes in the y-direction and 10,000 nodes in the x-direction at 60 mL/min.

To address this issue, the numerical approach was changed from a Crank-Nicolson approach to an approach using Matlab's built-in ODE45 solver, which uses a Runge-Kutta method with a variable time step for computational efficiency. The variable time step in the method also eliminates first node temperature oscillations because the node density is changed until a stable solution is achieved. As with the Crank-Nicolson method, the dependence of the accuracy on the nodal density nodal density was examined. The results are shown below, and as with the Crank-Nicolson approach 101 nodes are required for sufficient accuracy with 151 node providing slightly better results.

The trade-off between the Crank-Nicolson method and the ODE45 approach is computation time and memory requirements. The Crank-Nicolson method is very efficient for small node densities if temperature oscillation is avoided. In addition, the computation time and memory requirements are much more stable as they y-direction node density is increased. ODE45 provides a more consistent solution by eliminating

temperature oscillations, but it is much more computationally intensive with increasing node density. The computation time with increasing node density increases dramatically.

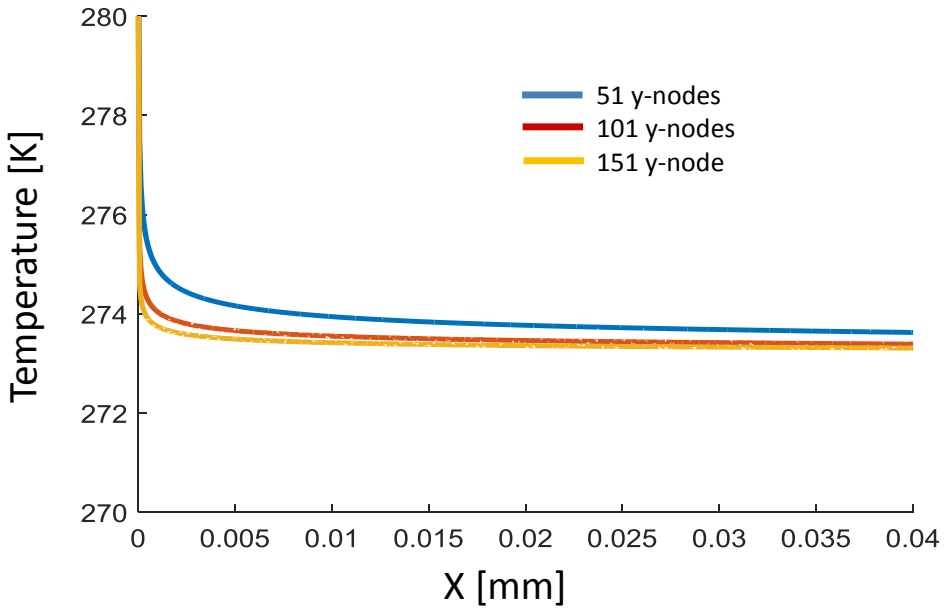

Figure 4-4: Plot of the effect of increasing node density in the y-direction on the first node closes to the wall using the Matlab's ODE45 function. The node density in the x-direction was kept constant at 100,000 and the flow rate was 60 mL/min.

One other draw back with the ODE45 approach is that the computation time is dependent on the flow rate with lower flow rates requiring higher node densities and more computation time. It should also be noted that the boundary condition plays a significant role on the computation speed of ODE45. For 151 nodes and above, the no slip boundary condition requires minutes to complete; whereas, cases with slip require less than 10 seconds to process.

A comparison between the Crank-Nicolson method for x-direction node densities of 10,000; 100,000; and 1,000,000 and for the ODE45 approach at flow rates of 60 mL/min and 200 mL/min for the no slip boundary condition are shown on Table 4-3. The values displayed in red represent conditions where temperature oscillation occurred, and MEM is a memory error that halted the program for the ODE45 approach prior to completion where the data files exceed 3.5 GB. Based on the results from the table, ODE45 with 151 nodes in the y-direction was chosen for the numerical analysis because of its high accuracy, stable temperature values, and relatively low computational requirements.

Table 4-3: Computation time comparison of the Crank-Nicolson method and Matlab's ODE45 approach for various node spacing and flow rates.

	51	*101*	*151*	*201*	*251*
CN_10,000	2.97	3.37	3.83	5.00	7.43
CN_100,000	28.92	32.79	37.57	49.56	74.34
CN_1,000,000	288.16	329.85	382.41	504.01	872.51
ODE45_60	2.11	15.95	66.02	301.74	MEM
ODE45_200	0.86	4.89	17.29	42.74	180.13

4.2 Thermal Analysis Results

Using the thermal model based on Matlab's ODE45 function, various aspects of the effect slip has on the hydrodynamic and thermal behavior of laminar flow between parallel plates were explored. As mentioned previously, the two goals of the numerical model were to predict the behavior of slip flow on heat transfer and to help design the experiment setup. To first get a better idea of the effect of slip on heat transfer, the axial

temperature distribution through the channel was plotted for various flow rates comparing the no slip and slip boundary conditions for a slip length of 0.5 mm. The results for two extremes are shown in Figure 4-5 and Figure 4-6. Figure 4-5 displays the results for a Reynolds number of 100 where the difference between outlet temperatures at the center of the channel was significant. Figure 4-6 show the results for a Reynolds number of 500 at which point the flow is too fast, and very little heat transfer occurred along the center line. The biggest temperature differences were near the wall near the inlet. As a result, there was little difference between the exit temperatures between the two cases. Thus, flow velocity and Reynolds number were very important to experiment design.

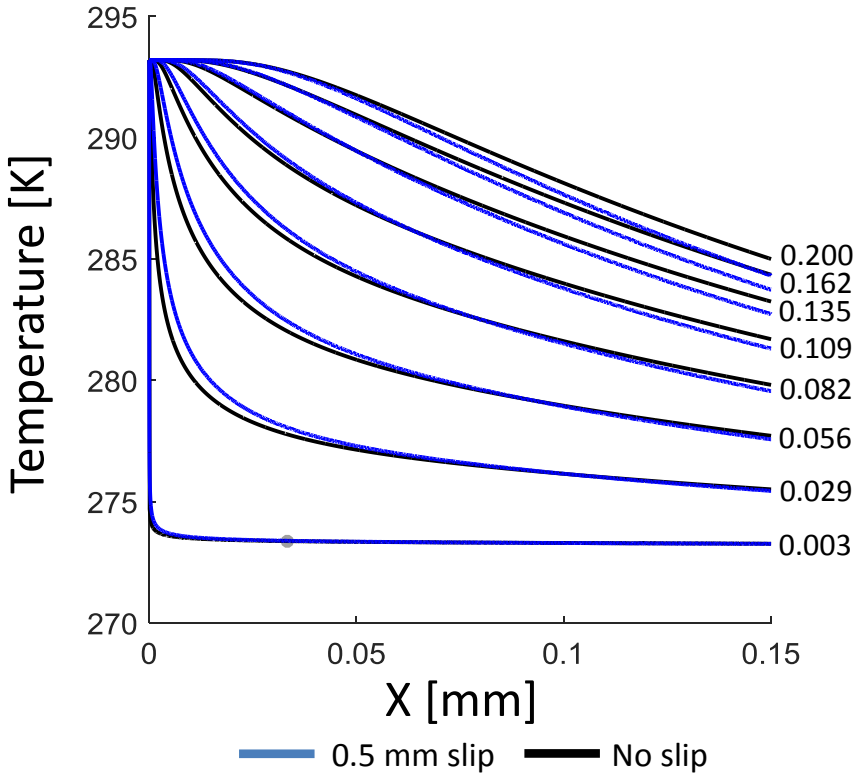

Figure 4-5: Axial temperature distribution through the channel for the no slip and slip boundary conditions with a slip length of 0.5 mm for an inlet Reynolds number of 100.

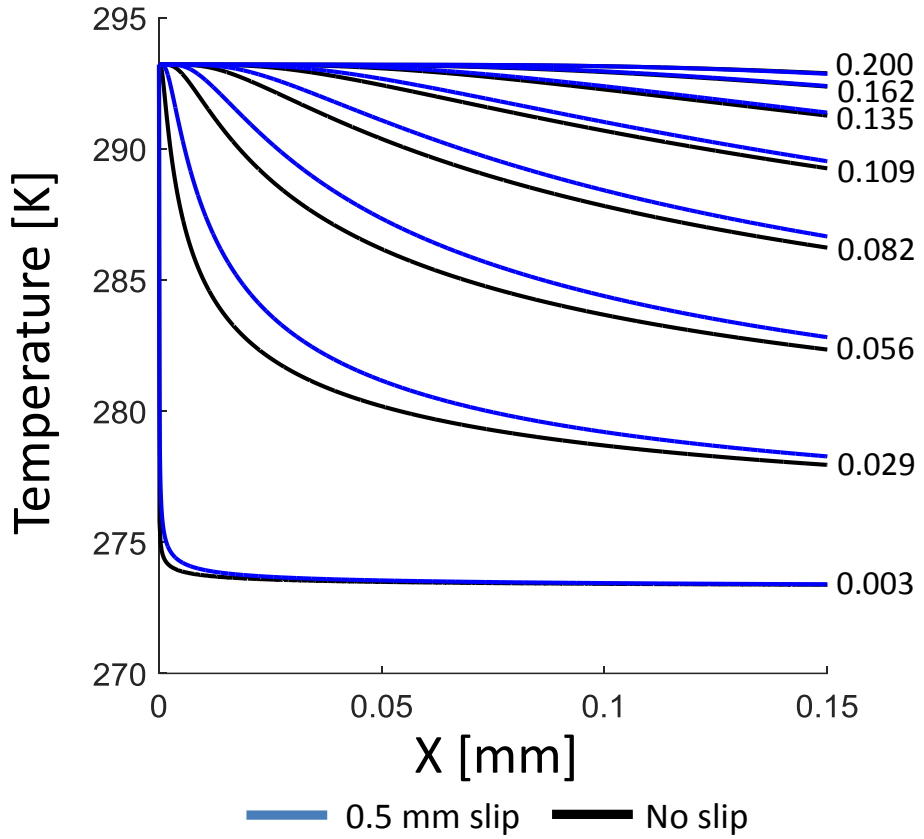

Figure 4-6: Axial temperature distribution through the channel for the no slip and slip boundary conditions with a slip length of 0.5 mm for an inlet Reynolds number of 500.

From these two plots, it is clear that outlet temperature profile is highly dependent on the flow rate and Reynolds number. Since the design of the experiment was to measure the temperature difference between the inlet and outlet of the channel to calculate the heat transfer performance, testing at flow rates that maximized the temperature difference was important to reduce the effect of measurement uncertainty on the results. Figure 4-7 compares the maximum temperature difference between the no slip and slip conditions for various normalized slip lengths, which was the slip length divided by half the channel height. The mean fluid temperature is the velocity weighted

average temperature at each node at the outlet and is determined from the temperature profile using (4-24).

From the plot, it is clear that target measurement range to maximize the differences between the no slip and slip cases is between Reynolds number of 100 to 200, which corresponds to flow rates of 120 and 230 mL/min. The maximum value occurs at a Reynolds number of 145, which corresponds to a flow rate of 170 mL/min. Based on these results a maximum temperature differences for slip range from 0.62 K to 1.97 K. However, this is based on the average temperature and larger values can be observed at specific locations in the flow profile where the temperature difference is larger. The location of the maximum temperature difference between the no slip and slip conditions depends on the flow rate and slip length and is at a different location for each case.

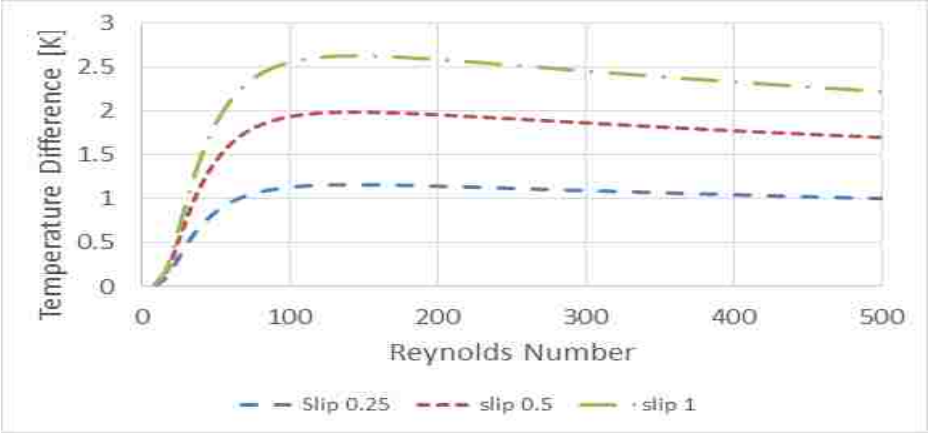

Figure 4-7: Comparison of the mean outlet temperature between the no slip and slip boundary condition for normalized slip lengths of 0.25, 0.5, and 1.

From Figure 4-7, the Reynolds number range that maximizes the temperature difference for the various slip lengths is from 50 to 200. The normalized velocity profile,

which is the velocity divided by the mean velocity, for no slip and normalized slip lengths of 0.25, 0.5, and 1 are shown on Figure 4-8, and the non-dimensional temperature profiles at the channel exit are shown on Figure 4-9. The non-dimensional temperature was defined above in (4-25) [60]. From the figures, it is clear that slip length has a stronger impact on the velocity profile than the exit temperature distribution and that the effect on temperature is not linear. In addition, it should be noted that since the flow is hydrodynamically fully developed in the test region, the velocity profile is constant across the range of Reynolds number as expected. However, from a thermal perspective, the flow is not fully developed, but despite this the non-dimensional outlet temperature distribution at Re = 50 is similar to Re = 200 with minor differences near the center line.

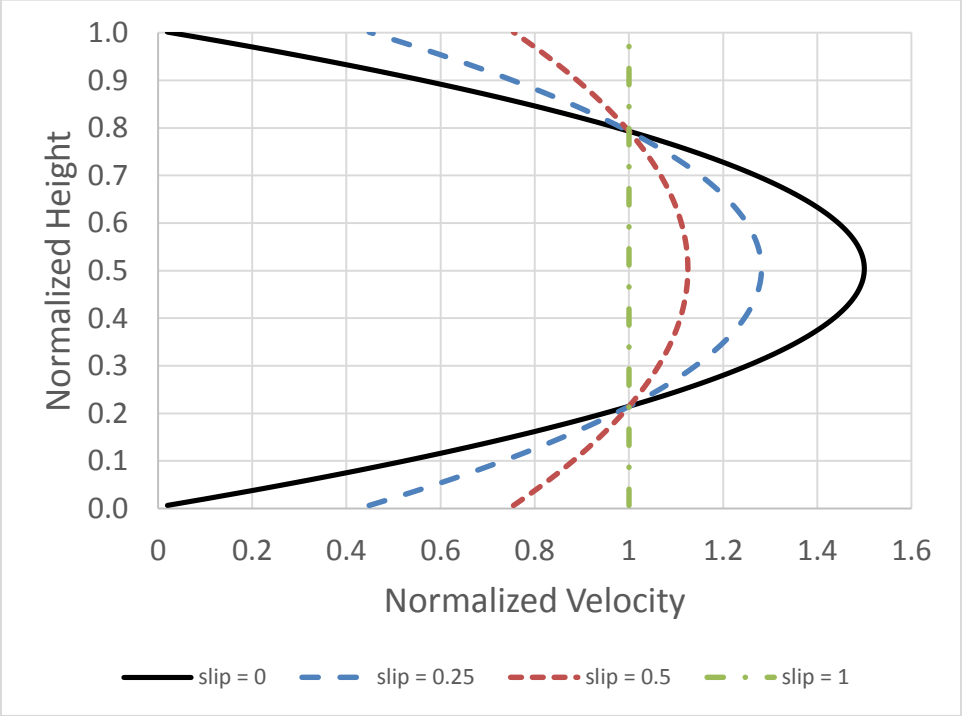

Figure 4-8: Normalized velocity profile with respect to y for parallel plates with channel height of 4 mm for slip lengths of 0.25, 0.5, and 1.

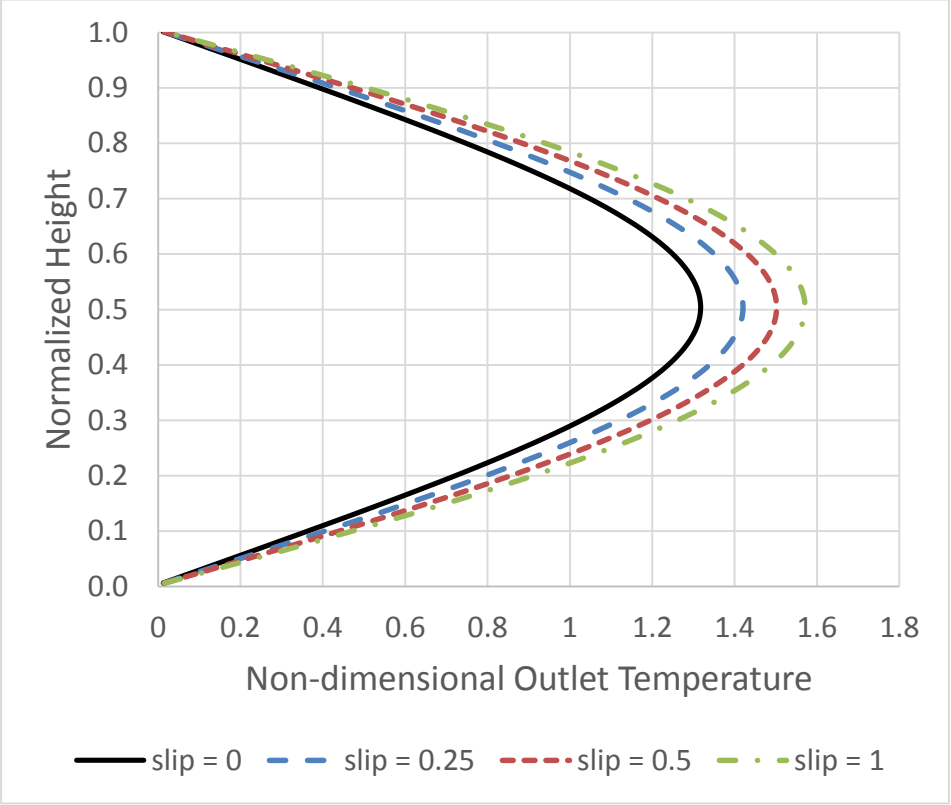

Figure 4-9: Non-dimensional temperature profile with respect to y for parallel plates with channel height of 4 mm for no slip and normalized slip lengths of 0.25, 0.5, and 1.

Finally, the heat transfer performance for the various cases and flow conditions were studied. Figure 4-10 displays the local Nusselt number in the axial direction for Re = 50, and Figure 4-11 shows the local Nusselt number for Re = 200. The figures clearly show that the no slip condition approaches the classical value for a constant temperature boundary condition, and the plug flow value for a normalized slip flow of 1. The increase in the Nusselt number at the outlet of the channels appears to increase linearly with the normalized slip length between the classical no slip and plug flow solutions. The case for Re = 50 appears to be nearly thermally developed

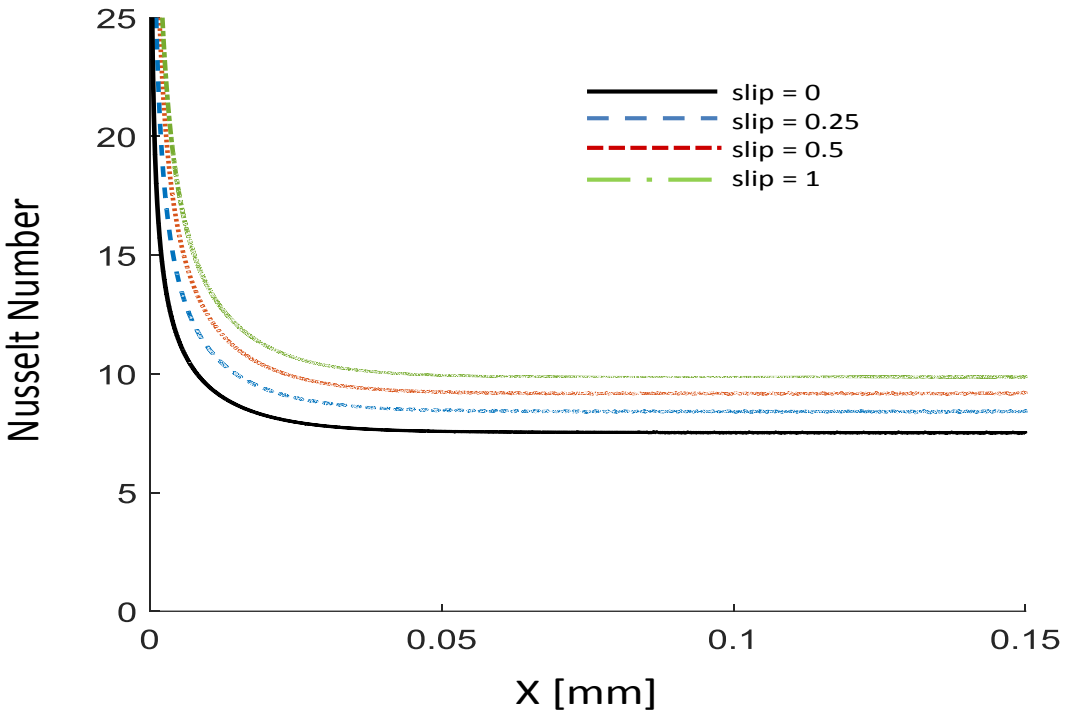

Figure 4-10: Local Nusselt number with respect to x for each normalized slip length at Re = 50.

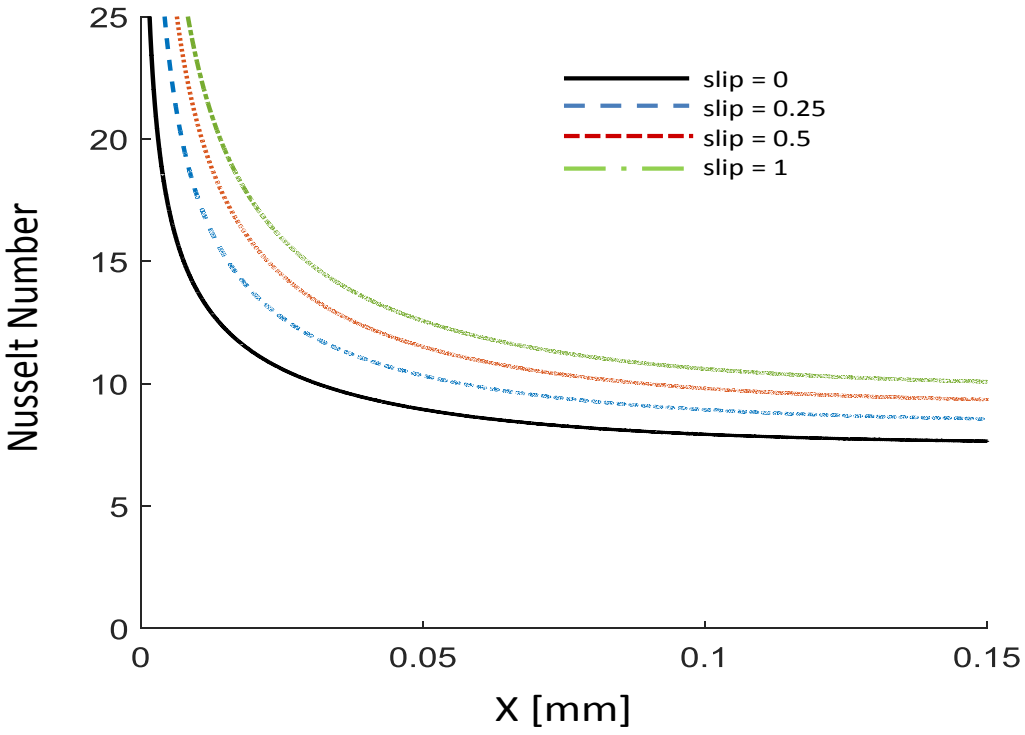

Figure 4-11: Local Nusselt number with respect to x for each normalized slip length at Re = 200.

4.3 Conclusions

This paper discussed the numerical analysis to evaluate the effect of the slip boundary condition on heat transfer using micro-patterned, superhydrophobic surfaces. The velocity profile was analytically solved and used to determine the thermal profile using numerical analysis approaches. Initially a Crank-Nicolson approach was used, but because of temperature oscillations near the wall for same cases, the model was transitioned to Matlab's ODE45 solver. The numerical results reveal that increasing the slip length improves heat transfer and that heat transfer increased asymptotically to the plug flow case for the parallel plates configuration analyzed. In addition, the temperature difference between the inlet and outlet temperature decays exponentially with respect to the Reynolds number, and a maximum mean outlet temperature difference of 2.63 K between the no-slip and 2 mm slip boundary conditions occurs between Reynolds number of 50 and 200 for this configuration. Finally, the heat transfer for the no slip condition approaches the classical value for no slip for the constant temperature boundary condition, and the plug flow value for a normalized slip flow of 1. The increase in the Nusslet number at the outlet appears to increase linearly with the normalized slip length between the classical no slip and plug flow solutions.

Chapter 5

Sample Fabrication

Sample fabrication was a significant challenge in the early stages of the research effort. Early on copper was selected as the preferred fabrication medium in part because its high thermal conductivity minimizes thermal gradients between the internal fluid flow and external constant temperature ice bath. Copper was also selected because of its common usage for thermal control systems including computer processor heat sinks, heat exchangers, and copper tubing in environmental control systems. Developing fabrication approaches that were compatible with copper increased the likelihood of transition of the technology beyond academic research.

As discussed previously, the key to achieving superhydrophobic surface conditions that promote slip conditions is the combination of micro- and nanoscale surface features and a hydrophobic coating to control the surface energy interactions at the three phase boundary line. The next sections will describe the micropattern fabrication approach as well as the hydrophobic surface treatments that were applied.

5.1 Micropattern Fabrication

The selection of the surface pattern and design was driven by two assumed and somewhat diverging requirements. The first was that maximizing the hydrodynamic slip boundary condition would minimize boundary layer resistance and increase heat transfer by moving convection effects closer to the boundary. Lee et al. demonstrated that for small pitches, micropost patterns provide higher hydrodynamic slip lengths than microridges for an equivalent pitch. They also showed that increasing pitch linearly increases slip length until the pitch is too large to support the fluid and the surface transitions from a Cassie to a Wenzel state [27], [28]. Coupled to this requirement is the requirement that the pattern must have sufficient surface roughness to ensure a stable Cassie state under pressure driven flow. This requirement places a limit on pitch since smaller pitches provide more stable fluid intrusion resistance than large pitches. The second assumed requirement was to maximize the solid-fluid contact area. Because the thermal conductivity of air is orders of magnitude less than copper, the primary conduction path into the fluid is the solid-fluid interface. Maximizing the solid-fluid interface maximizes the heat transfer into to the fluid. These requirements are divergent to each other.

The optimization of these diverging requirements depends on their relationship to heat transfer effects. From Figure 3-11, it is clear that the effect of slip length on the Nusselt number is exponential and rapidly approaches a point of diminishing returns. The

relationship between cavity fraction and Nusselt number in Figure 3-15 shows a similar relationship; however, the change in slope of the curve is much less than for slip length. Finally, Figure 3-14 shows there is a linear relationship between cavity fraction and the Poiseuille number for streamwise microridges. Taking all of these relationships into consideration, a cavity fraction of 0.5 was selected to emphasize Nusselt number enhancement and ensure a stable Cassie state. It should be noted if the design goal is to maximize the hydrodynamic-thermal efficiency factor, then the maximum stable cavity fraction should be selected based on Figure 3-16. However, that was not the goal of this effort. The goal of this effort was to maximize heat transfer enhancement.

To fabricate the micropattern structure on the surface of the copper substrates, laser machining was performed by Mound Lasers and Photonics Center, Inc. (MLPC) in Dayton, OH. The micropattern that MLPC machined on each sample consisted of lengthwise ridges with 25 μm width, 25 μm spacing between ridges, and 50 μm height. These dimensions satisfy the cavity requirement stated above, and also satisfy the design guidelines summarized in Section 2.5. An example of a microridge test plate is shown in Figure 5-1, and microscope images from the top and side are shown in Figure 5-2 through Figure 5-4. The side view image clearly shows that the width of the cut is not uniform through the depth and has much wider opening at the top compared to the bottom. The image also clearly shows that the ridges are not square cut but have rounded edges. The round edges likely did not produce as high a slip length as possible compared to square

cut edges based on the work of Lee [29]. However, they did adequately promote a hydrophobic state.

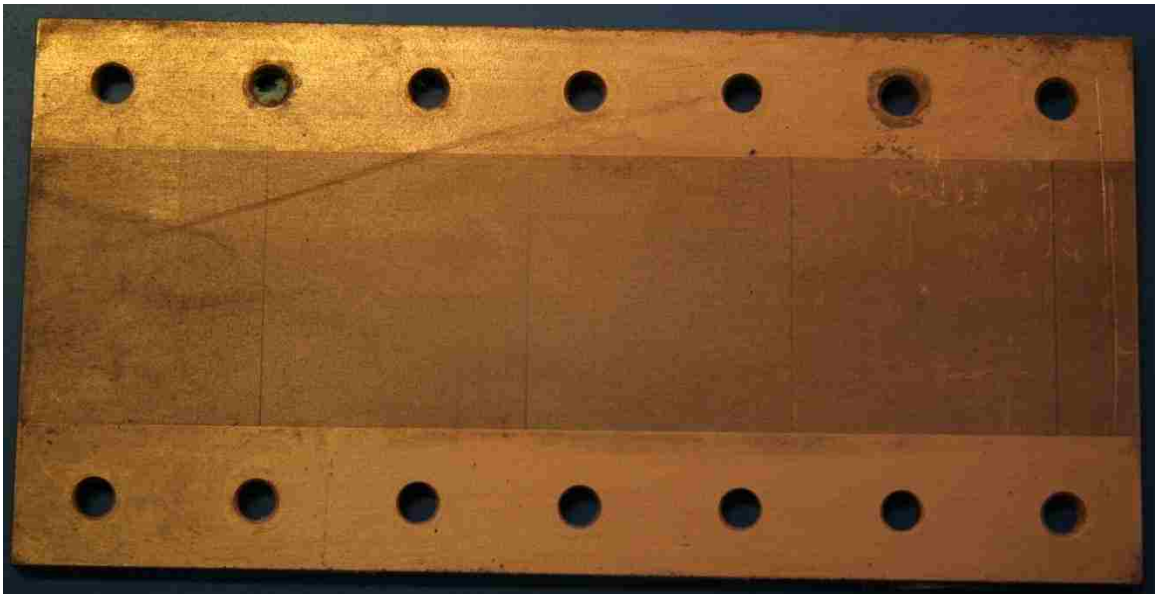

Figure 5-1: Photograph example of a microridge test sample made by MLPC, Inc.

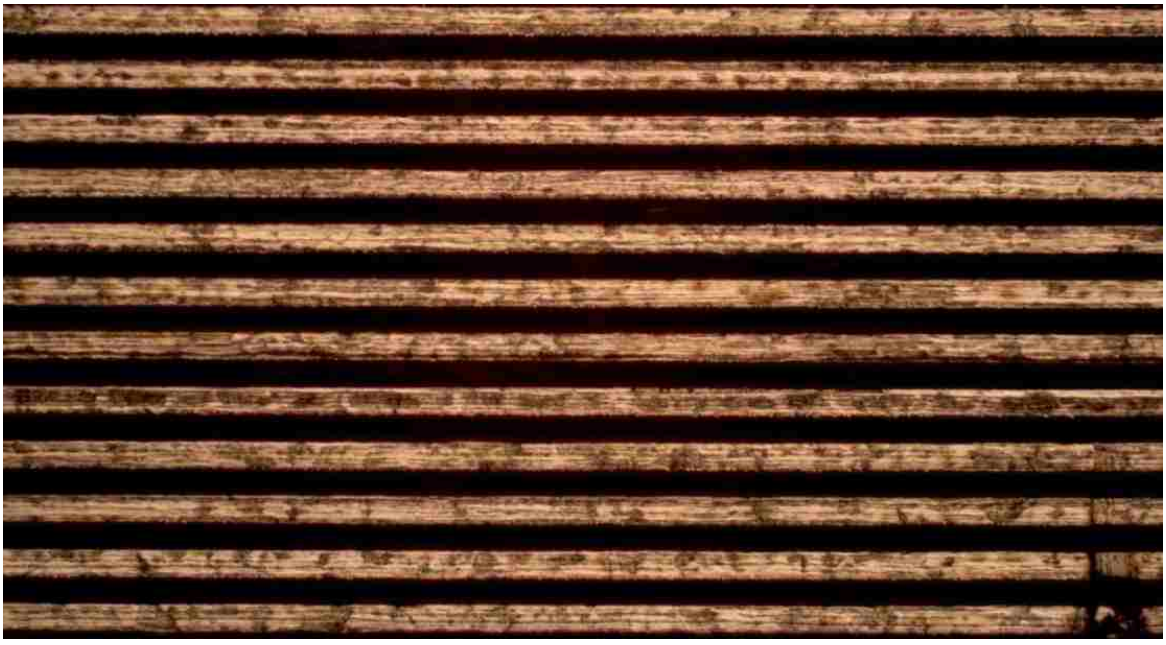

Figure 5-2: Top view microscope image of laser machined microchannels at 10x magnification

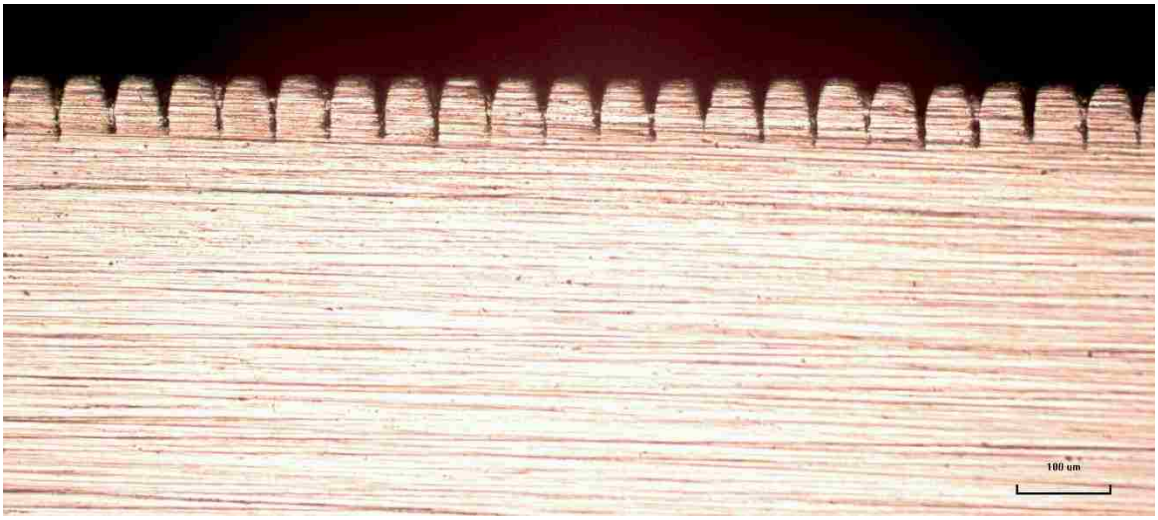

Figure 5-3: Side view microscope image of laser machined microchannels at 10x magnification. The lengthwise ridges have 25 μm spacing, 25 μm width and 50 μm height

Figure 5-4: Side view microscope image of laser machined microchannels at 20x magnification.

The maximum machining area for the laser was limited to 3.8 cm by 3.8 cm. The 16 cm channel length was made by repositioning the sample in the active cutting area along the length. The result was a periodic discontinuity between each of the cutting sections. Since the hypothesis was that the combination between the hydrophobic coating and the

micro-patterned surface results in the fluid contacting the top surface of the ridges and not penetrating into the depth of the ridge structure, the periodic discontinuity in ridge alignment should not affect the overall results. Two examples of the discontinuity between sections are shown Figure 5-5.

a) 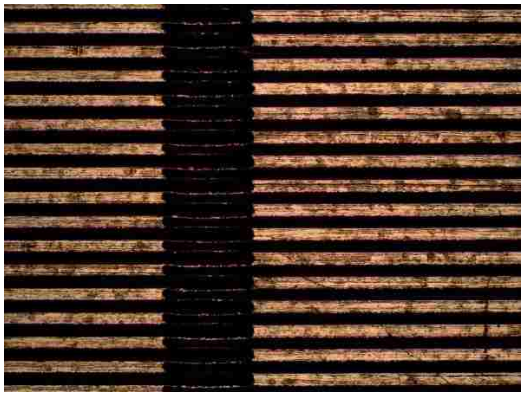 b) 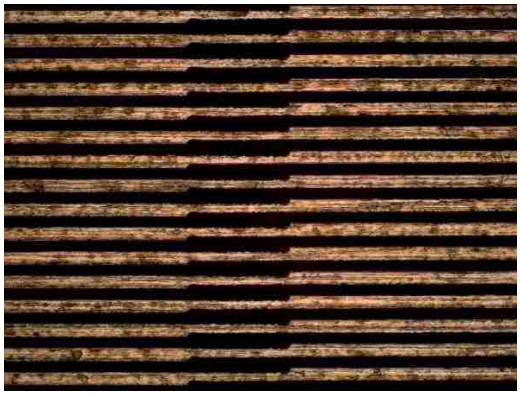

Figure 5-5: Two examples of the resulting ridge discontinuity caused by the 1.5 inch by 1.5 inch cutting area limitation of laser cutter: a) shows a complete misalignment resulting in the removal of all material and b) shows better alignment with partial ridge continuation.

5.2 Hydrophobic Coatings

To achieve a high slip boundary condition, both a hydrophobic coating and a micro-patterned surface are required. The first hydrophobic coating that was applied to the copper substrates was an aerogel coating based on the research of Gogte et al. and Truesdell et al. that had demonstrated a high wall slip potential in their testing [25], [36], [168]. The aerogel solution developed for this test effort followed the same recipe used previously and was originally developed by Prakash et al. [169]. The aerogel coating was prepared using a low temperature/pressure thin film process in which tetraethyl

orthosilicate was replaced with a 1:0.3 molar ratio of tetramethyl orthosilicate and trifluoropropyltrimethoxysilane [25]. Silicon samples were initially used as test pieces to determine coating thickness versus dip speed. The samples were dip coated using an automated system to control the rate at which the samples were removed from the aerogel solution and were dipped at 10, 20, and 30 mm/min. The thickness was measured using a scanning electronic microscope (SEM). Examples for each of the coating speeds are shown in Figure 5-6 through Figure 5-8 and the results are compiled on Table 5-1. Because the aerogel coating has a relatively poor electrical conductivity, a very thin layer of gold was applied to the top surface to assist in measuring the coating thickness in the SEM.

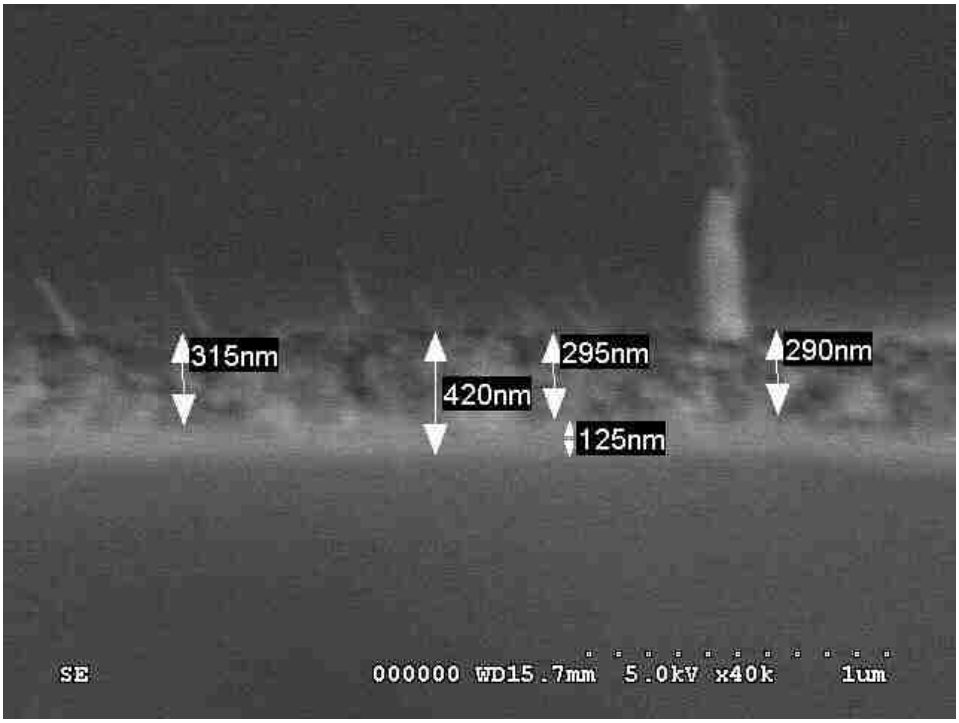

Figure 5-6: SEM example measurement of aerogel dip coated silicon at a rate of 10 mm/min.

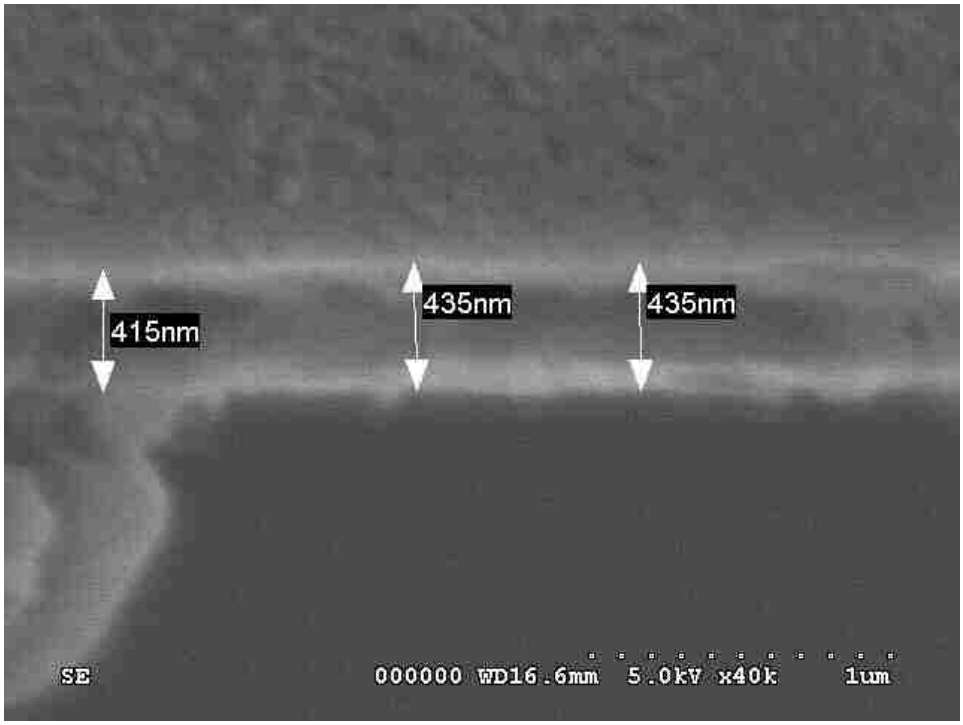

Figure 5-7: SEM example measurement of aerogel dip coated silicon at a rate of 20 mm/min.

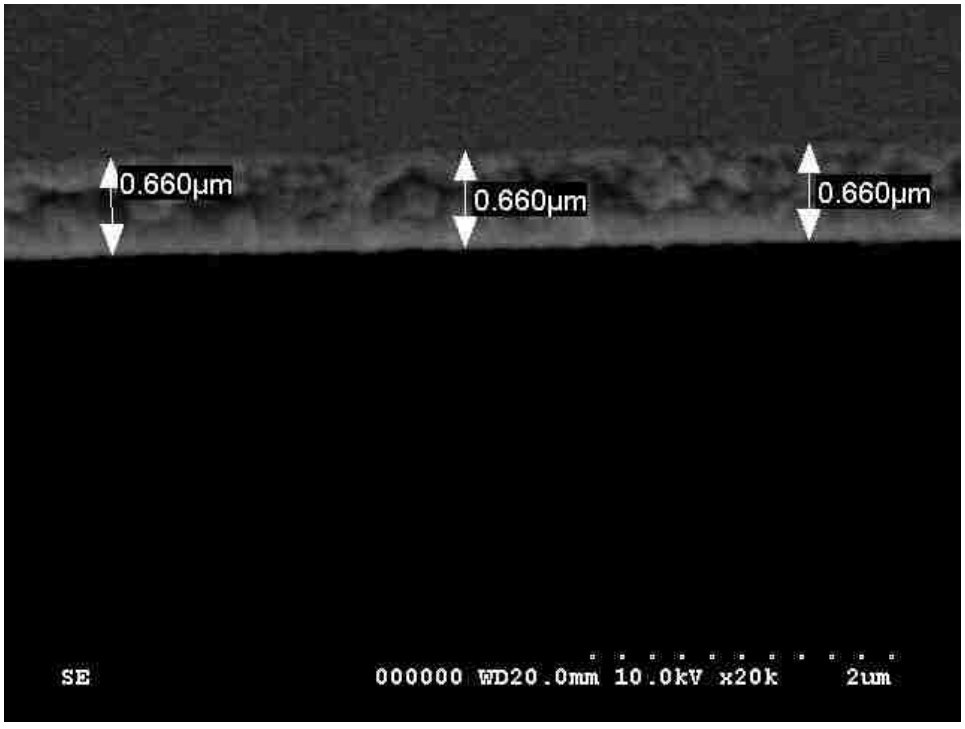

Figure 5-8: SEM example measurement of aerogel dip coated silicon at a rate of 30 mm/min.

Table 5-1: Complied coating thicknesses from SEM measurements for aerogel coating on silicon.

Location	Aerogel 10 [nm]	Aerogel 20 [nm]	Aerogel 30 [nm]
1	240	510	640
2	245	495	672
3	315	480	704
4	295	470	728
5	290	472	570
6	295	415	660
7	275	435	660
8	300	435	660
Average	**282**	**464**	**662**
StdDev	**27**	**33**	**47**

From Truesdell's [168] research, the ideal single dipped aerogel coating thickness was 500 nm. Based on the results from the SEM measurements, a coating speed of 20 mm/min was selected for the fabrication of the copper samples. Photograph of the aerogel coated sample is shown below.

Figure 5-9: Photograph of the coated aerogel plates using a dip speed of 20 mm/min.

In addition to the aerogel coating tested by Truesdell [168] and Gogte et al. [25], a commercial off-the-shelf hydrophobic coating selected and tested. The coating was a

consumer hydrophobic coating manufactured by Rust-Oleum® under the tradename NeverWet®, which is s a two-step system designed to create a moisture repelling barrier on metal, wood, aluminum, galvanized metal, PVC, concrete, masonry, asphalt, vinyl siding, fiberglass, canvas, and most plastics. The application process consisted of two parts: a base coat and a top coat that were both applied using an aerosol spray application. The MSDS components for each layer are shown on Table 5-2.

Table 5-2: MSDS for Rust-Oleum® NeverWet® components for base coat (left) and top superhydrophobic coat (right).

Chemical Name	Weight % Less Than
Aliphatic Hydrocarbon	20.0
Propane	20.0
n-Butyl Acetate	15.0
Methyl Isobutyl Ketone	15.0
Methyl Acetate	15.0
n-Butane	10.0
Ethyl Acetate	10.0

Chemical Name	Weight % Less Than
Acetone	75.0
Propane	20.0
n-Butane	10.0
Silicone Derivative (Proprietary)	5.0

Prior to applying the coating, the surface was cleaned and polished with a three step process. First, a weak acid was used to remove the top oxidation layer. Next, the surface was then cleaned with deionized water and acetone to remove the weak acid and any residual grease from the surface. Finally, isopropyl alcohol was used to remove any traces of the acetone. This cleaning process was used on all samples. After cleaning, each coating was applied per the application directions that came with the packaging. The base coat was applied in two layers with one hour between coatings. The first layer was applied in a left to right motion and the second layer was applied in an up and down

motion. The top coat was then applied in four thin layers with one hour between coatings. The final coating was allowed to dry for more than 24 hours before any test activity commenced. When not in use, the samples were stored in a nitrogen purge cabinet to minimize the potential for the copper to oxidize or the coating to degrade in the ambient laboratory environment. Images of the coated sample are shown in Figure 5-11 for the smooth surface samples and in Figure 5-12 for the microridge samples.

Figure 5-10: Photograph of the aerosol spray coated Rust-Oleum® NeverWet® smooth sample.

From the images it is clear that the coating is not smooth and has a random distribution of globs on the surface with a significant differential in height which causes much of the image to be out of focus. This is likely a product of the design of the coating to help enhance its hydrophobicity by adding microtexturing to the surface. The same surface structure forms on pretty much any surface the NeverWet® is applied. For the microridge samples, the coating forms the same globs as the smooth surface. The ridge structure can be seen in the microscope image, but it is unclear if there is a height differential caused by the microridges in the top surface of the hydrophobic coating.

a)

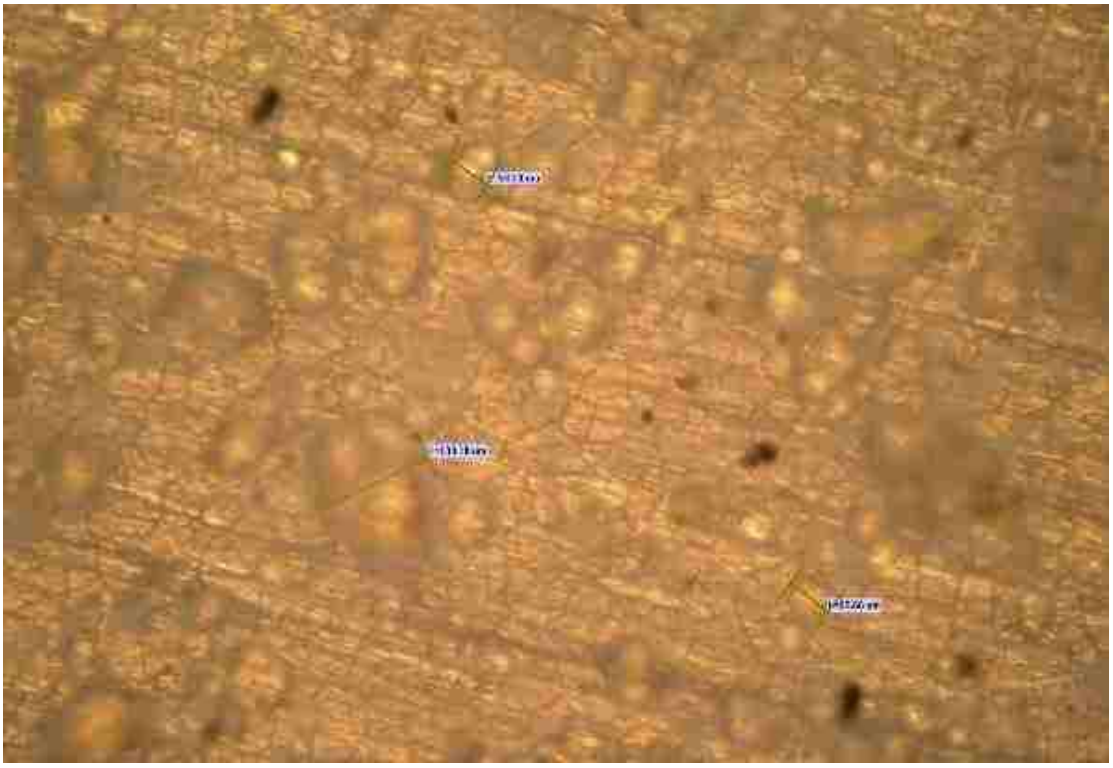

b)

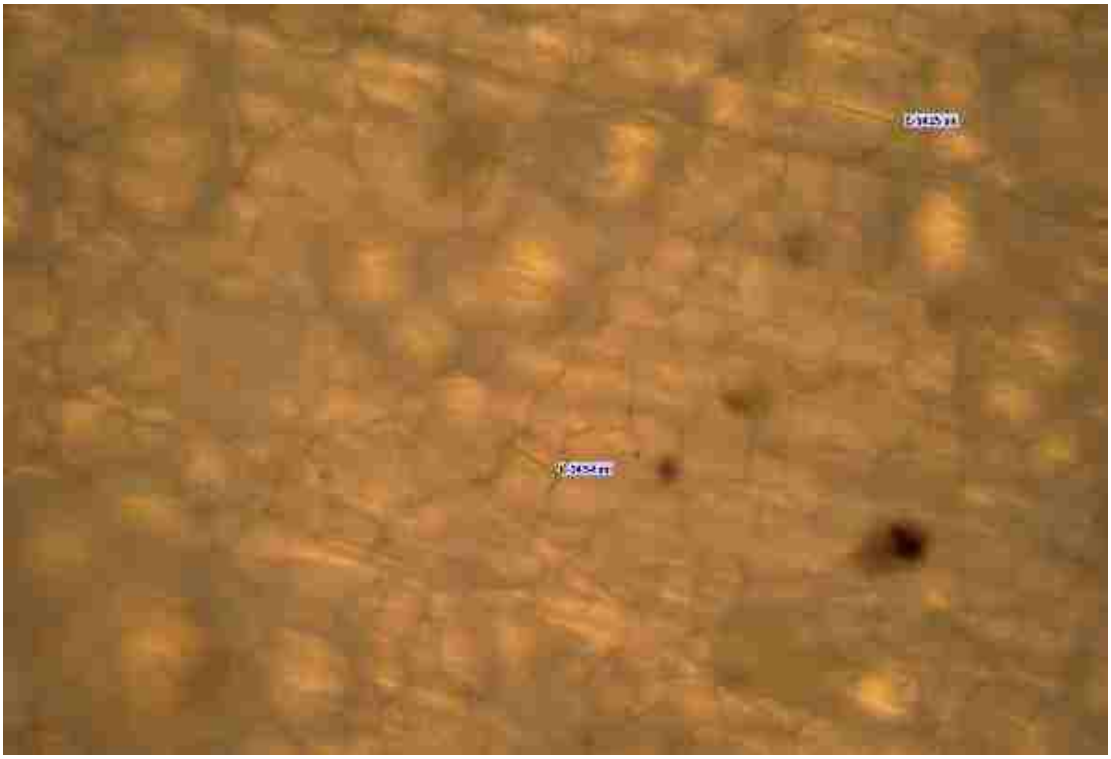

Figure 5-11: Microscope images of the Rust-Oleum® NeverWet® coating on the smooth surface copper sample at a) 10x magnification and b) 20x magnification.

a)

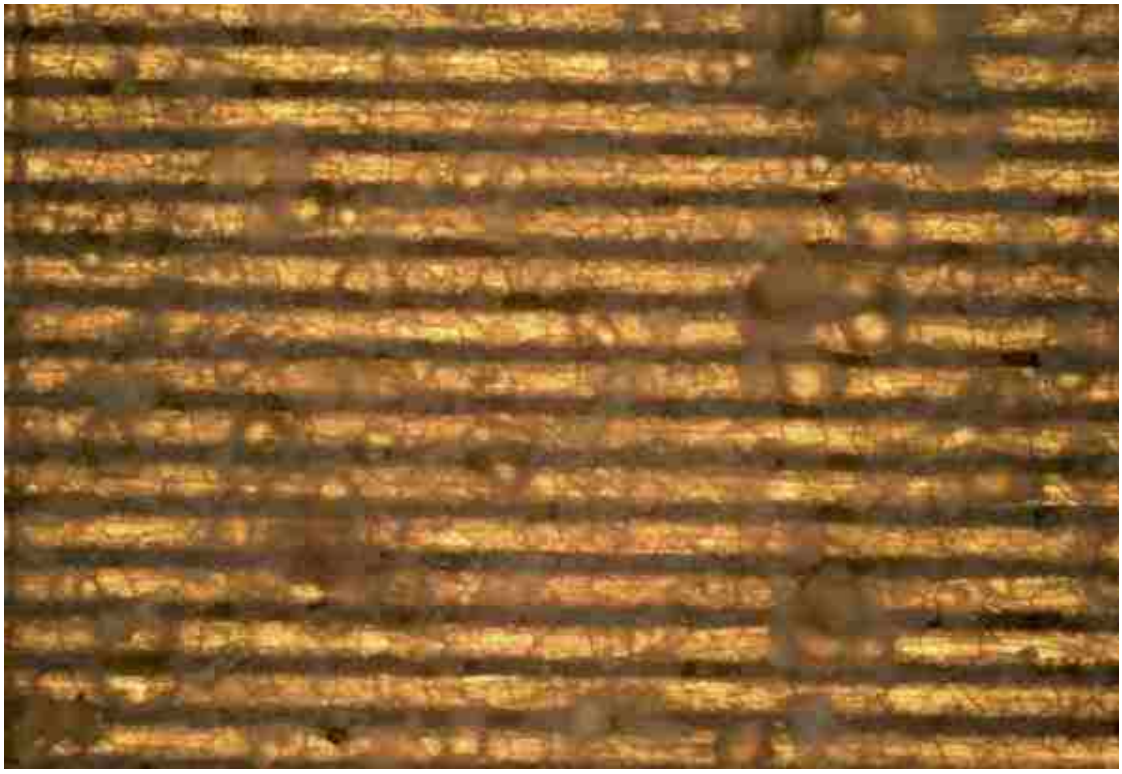

b)

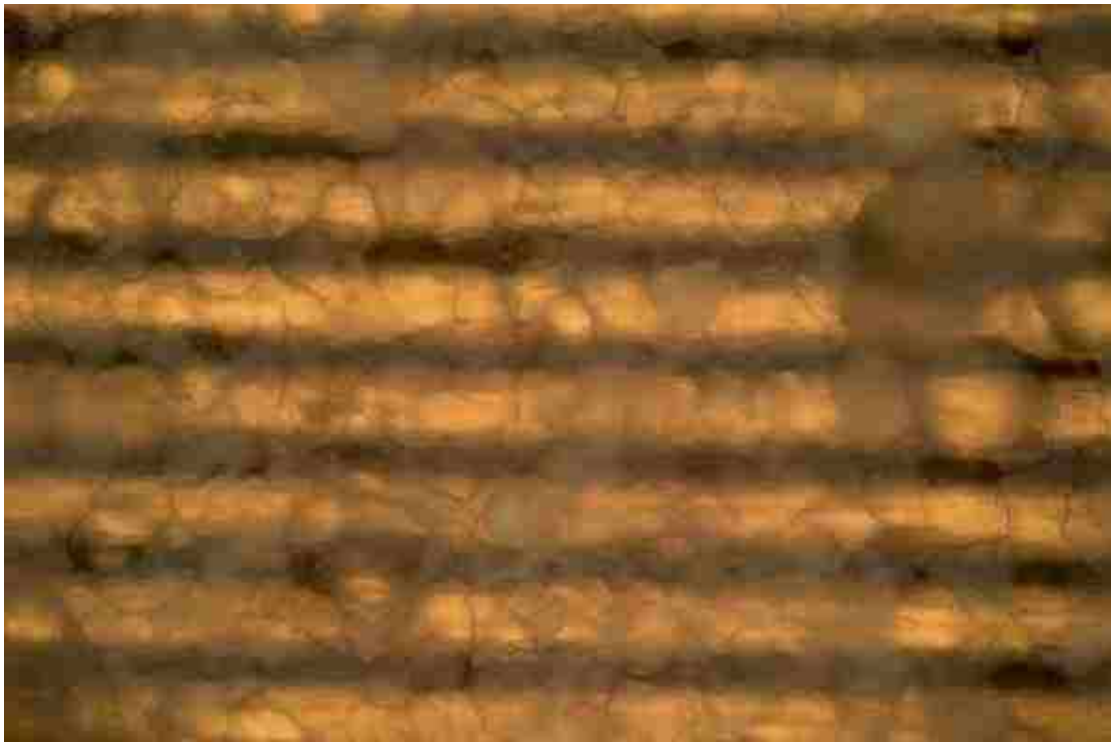

Figure 5-12: Microscope images of the Rust-Oleum® NeverWet® coating on the microridge surface copper sample at a) 10x magnification and b) 20x magnification.

Chapter 6

Contact Angle

To fully understand the effects of superhydrophobicity on friction loss and heat transfer, the surface characteristics must be fully understood. This includes both the contact angle and contact angle hysteresis as well as the ambient temperature and relative humidity when the measurements are taken. In most of the literature examining hydrophobicity and hydrophilicity, the contact angle is generally the only data point reported. Occasionally, the temperature is reported. The most comprehensive dataset for contact angle and contact angle hysteresis measurements was provided by Taft, Smith, and Moulton [85]. The emphasis of this chapter is on the contact angle and contact angle hysteresis measurements for all of the test samples.

6.1 Contact Angle Measurements Background

Once the various samples were fabricated, it was important to determine the degree of hydrophobicity for each sample. The first step was to measure the contact angle to

verify that an apparent contact angle exceeding 150° was achieved. Accurately measuring apparent contact angle can be quite challenging for superhydrophobic surfaces and there is a wide range of measurement techniques for determining the apparent contact angle of a droplet on a surface. They can be categorized into two major groups: direct optical measurements and indirect force balance measurements [133]. The next sections will review the various approaches to measure contact angle as well as the strengths, weaknesses, and accuracy of each approach.

6.1.1 Review of Direct Optical Measurement Techniques

One of the first and most widely used contact angle measurement techniques is the telescope-goniometer developed by Bigelow et al., which directly measured the tangent angle at the three phase contact point on a sessile drop [170]. A typical apparatus consisted of a micrometer pipette and motor driven syringe to form the sessile drop, a telescope with protractor eyepiece, a camera, and a light source. The telescope provided high magnification to enabled detailed examination of the interface profile which enhanced accuracy of the measurement [171]. Using a telescope-goniometer connected to a CCD camera, Sklodowaka et al. [172] used computer analysis based on a fragment of an ellipsoid of revolution to measure the contact angle. The motor driven syringe can also be used to measure the advancing and receding contact angle [173].

The advantages of this method are its relative simplicity and the fact that only small liquid volumes and solid substrate sizes are required. The biggest disadvantages are that

measurements are highly dependent on the accuracy and consistency of the user to follow precise guidelines to accurately assign the tangent line and that contact angles less than 20° cannot be accurately measured because of uncertainty in assigning the tangent angle when the drop is relatively flat. In addition, limitations of the optical profile, surface roughness variations, and contaminates will cause aberrations in the contact angle that are not captured by this technique. Only the intersection of the meridian plane and three-phase line is captured in the measurement [133]. Despite these limitations, the telescope-goniometer technique is commonly used where the contact angle accuracy requirement is greater than ±2° because of its relative simplicity [174], [175].

Variations on the telescope-goniometer approach include using a tangentometer, which consists of a mirror mounted at the baseline of the droplet that is rotated until the curve of the drop shape forms a smooth continuous curve on the mirror and a specular reflection approach that uses rotate a light above the three-phase line until small variations in rotation cause the light to appear or disappear [176], [177], [178]. Both methods eliminated user dependent accuracy error to some degree and have achieved accuracy of ±1° on sessile drops and menisci on flat plates and inside tubes [179].

Alternative techniques to sessile drop techniques use bubble or meniscus properties to determine the contact angle. The captive bubble approach uses an air bubble formed underneath a horizontal solid submerged in the test liquid and the contact angle of the bubble is directly measured [180], [181]. The advantages of this method include

monitoring fluid temperature to determine the temperature dependence of the contact angle, ensure the surface is in contact with a saturated atmosphere, and minimized contamination effects at the solid-vapor interface. The biggest disadvantages are high large liquid volumes and incompatibility between materials i.e. swelling solids or films on the solid dissolved by the liquid [133]. Good agreement between the sessile drop methods and the captive bubble method have been observed [182].

Meniscus-based techniques utilizes the properties and interactions of the three-phase interface in the meniscus to determine the contact angle. The tilting plate method uses a plate partially inserted the fluid that is rotated until the meniscus becomes horizontal on one side of the plate as in Figure 6-1. The angle between the plate and horizontal meniscus is the contact angle. The advantages of this approach are its relative simplicity, reduced dependents on the user's accuracy, and the ability to measure small contact angles. However, its accuracy is limited to ±5° because of surface-liquid contaminates, disturbance of the liquid by the rotating plate, and ensuring the solid-liquid interface remains at the axis of rotation [183]. Using more advanced techniques and measurement devices, the accuracy can be improved to ±2.5° [184], [185]. More modern, special techniques have also been used to improve the accuracy of this method by reducing the effects of solid-liquid contaminates, adding scanning laser measurement techniques, and applying high sensitivity thermocapillary response to the static curvature of the meniscus [186], [187].

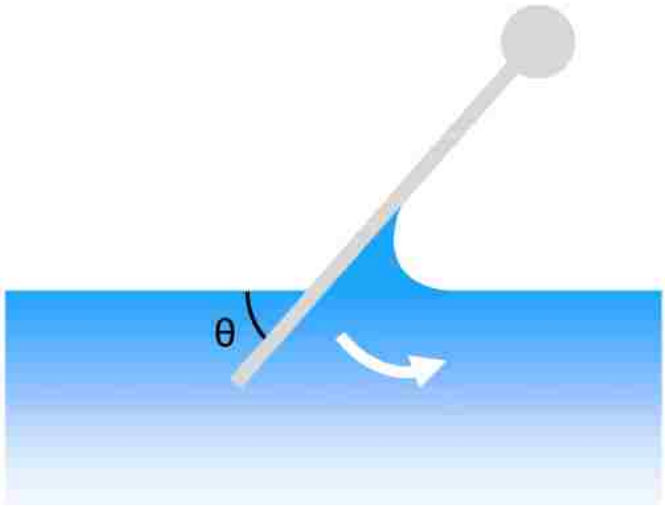

Figure 6-1: Illustration of the tilting plate method to measure the contact angle [133].

For cases where high accuracy of the dynamic contact angles are required or for cases with very low contact angle hysteresis, the capillary bridge method can be used. For this method a spherical solid, such as a watch glass, is placed in contact with a liquid such that a meniscus or capillary bridge forms around the contact line because of capillary effects as shown in Figure 6-2. The dynamic contact angle is determined by measuring changes in the wetted area and the height of the sphere from the surface and using the Young-Laplace equation of a simplified approximation:

$$A_w = 2\pi r\left(\kappa^{-1}\sqrt{2(1+\cos\theta)} - h\right) \tag{6-1}$$

where A_w is the wetted area, h is the height of the sphere from the fluid bath surface, r is the radius of the sphere, and κ is the capillary length of the liquid. The contact angle is determined from the experimentally measured A(h) curve [188], [189].

The advantages of the capillary bridge method include high accuracy, ability to easily measure the advancing and receding angles for systems with very low contact angle hysteresis, and the ability to accurately measure values for low friction coatings [190]. The disadvantages of the method include challenges with measuring the wetted perimeter, which usually requires transparent films to be coated on a transparent spherical surface thereby causing material limitations and challenges preparing samples [191].

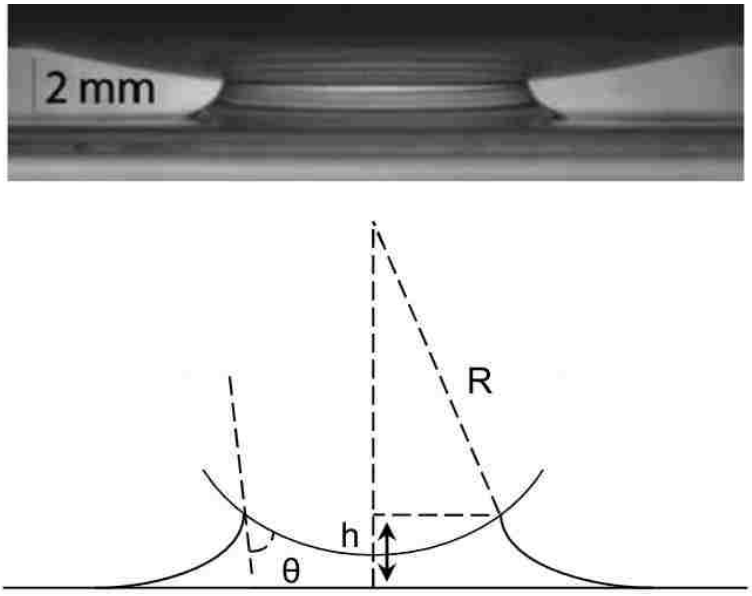

Figure 6-2: Image of the capillary bridge method and the contact line calculation [188].

6.1.2 Review of Indirect Force Measurement Techniques

Rather than optically measuring the contact angle or three-phase line properties, indirect force measurements use the interactions of wetting and buoyancy forces to determine the contact angle. The Wilhelmy balance method uses a balance or force

sensor to measure the change buoyancy and wetting force when a thin vertical plate is brought into contact with a liquid. The wetting force, f, is defined as [192]:

$$\mathrm{f} = \gamma_{LV} p_c \cos\theta \tag{6-2}$$

where p_c is the perimeter contact line. The total force change detected is a result of buoyancy and wetting forces and the contact angle can be calculated by:

$$\cos\theta = \frac{\Delta f + V\Delta\rho_{LV} g}{\gamma_{LV} p_c} \tag{6-3}$$

where Δf is the change in force on the force balance, V is the volume of displaced fluid, $\Delta\rho$ is the difference in density between the liquid and air, and g is the acceleration of gravity [193], [192].

The advantages of the Wilhelmy balance method are that it eliminates the challenge of correctly identifying the contact location and angle and replaces it with straight forward weight and length measurements, which can be performed with high accuracy and without subjectivity. In addition, the force measurement at any submersion depth is the average force over the wetting surface thereby yielding an average contact angle value over a large area. Finally, the dynamic contact angle and contact angle hysteresis can easily be determined for different wetting rates using this method. The drawbacks of this approach include the requirement that the solid must have a uniform cross-section with a known perimeter which makes simple geometries ideal and the sample must have the same composition and topography on all sides.

An alternative approach to the Wilhelmy balance method uses the capillary rise on a vertical plate to calculate the contact angle. The height of the capillary rise, h, can be determined by integrating the Laplace equation [194], [193]:

$$\sin\theta = 1 - \frac{\Delta\rho g h^2}{2\gamma_{LV}} \tag{6-4}$$

For this method to work, the plate must theoretically be infinitely wide, which is practically satisfied by plates measuring more than 2 cm in width [133]. By modifying the Wilhelmy balance method, the capillary rise height can be measured to calculate the contact angle [195]. The advantages and disadvantages of this method are similar to the Wilhelmy balance method, but the method has been automated [196], [197], and using trigonometric relationships, both the contact angle and liquid surface tension can be calculated simultaneously [198].

6.1.3 Drop Shape Analysis Techniques

With the proliferation of high resolution digital cameras and computers, automated drop shape analysis techniques have become much more prevalent and extremely accurate. Drop shape analysis techniques find the best theoretical profile fit for a digital droplet image and calculate the surface tension, contact angle, drop volume, and surface area of a sessile droplet, captive bubble, or pendant-shaped drop. These approaches utilize the balance of force between surface tension which wants to form a spherical droplet and external forces, primarily gravity, that want to flatten a sessile drop. The

balance between the forces is captured by the Laplace equation of capillarity, which provides the means to determine surface tension by analyzing drop shape [133].

Before the advent of digital systems, the $\theta/2$ method was used to determine contact angle from a sessile droplet shape. Assuming that the droplet is spherical, which is accurate when the droplet is smaller than the capillary length from Equation (2-11, the contact angle can be calculated using:

$$\frac{\theta}{2} = \tan^{-1}\frac{h}{d} \tag{6-5}$$

where d is the droplet diameter and h is the height at the apex of the droplet. This approach is only valid for small drops where external forces such as gravity can be ignored. Bashforth and Adams [199] used this approach to create sessile drop profile tables that could be used to interpolate contact angle based on surface tension and the radius of curvature at the apex of droplet [193]. Other authors have added to the Bashforth and Adams tables for sessile droplets and for pendant drops [200], [201], [202]. Using digital systems, many advancements to this technique have been made [133], [203], [204].

One of the major advances in drop shape analysis made possible by digital systems is the Axisymmetric Drop Shape Analysis (ADSA) method and is one of the most accurate techniques for high precision contact angle measurements with a reproducibility of ±0.2° [133]. The method originally developed by Rothberg et al. matches the best theoretical profile to the drop's shape by adjusting the surface tension until the theoretical profile

matches the experimental profile by minimizing the sum of the squares of the normal distances between the experimental profile and the theoretical profiles [205]. The assumptions of this approach are that 1) the drop is Laplacian and axisymmetric and 2) gravity is the only external force acting on the drop.

The original method has been improved by implementing computer-based edge operators, automated drop edge detection techniques, various optical distortion correction techniques [133], [203], [206], and more efficient algorithms using the curvature at the apex rather than the radius of curvature at the apex. An offshoot of the ADSA approach for contact angles less than 20° has also been developed that uses a top view image of the drop to measure the contact diameter [204]. The agreement between both ADSA approaches is ±0.4° with the diameter-based approach providing higher precision at low contact angles than the profile-based approach [207], [208].

A new drop shape method introduced by Cabezas et al. [209], [210] named Theoretical Image Fitting Analysis (TIFA) uses the whole two-dimensional projection to fit the theoretical profile to the experimental image instead of the ADSA approach of fitting only a one-dimensional curve to the image. TIFA does not use edge detection and employs an error function that measures pixel-by-pixel difference between the theoretical profile and the experimental image to find the optimal match [133]. TIFA, much like ADSA, suffers from a limitation in that the apex of curvature of the drop is used in the calculation. Thus, the most common sessile drop deposition approach where the

syringe needle is submerged in the droplet to minimize perturbations cannot be used. This limitation has led to the development of both TIFA and ADSA approaches that utilize alternative reference points than the apex to solve the Laplace equation and for curve fitting optimization with results approaching ±0.1° [211], [212].

Various authors have used new and specialized techniques to measure contact angles ranging from the mutual displacement of two immiscible fluids through a capillary, spreading a liquid between parallel plates, rotating a partial submerged cylinder in a liquid, capillary penetration methods, and various drop curve fitting techniques including ellipse, quadratic polynomial, spline curve, curve ruler fitting approaches [101]. However, the two most frequently used approaches are microscope examination of a sessile drop and the Wilhelmy balance method (and its variations). The choice of contact angle method depends on the geometry of the system and the contact angle to be measure i.e. large or small contact angles are harder to measure and can require specialized approaches. For this effort, the sessile drop method using drop analysis techniques was used.

6.2 Contact Angle Measurement Results

To measure the contact angle, an approach similar to that described by Lamour and Hamraoui [87] was used. Droplets were placed on each sample and photographed using a Canon 30D digital camera with an EFS 60 mm macro lens (1:2.8 USM). The drops were carefully placed using a 30 mL Luer-Lok™ syringe with a 25G x 1” Turemo® needle. The

syringe was clamped to a test tube stand to ensure height above the sample was consistent. The syringe tip was maintained at a height of 1 ±0.5 mm above the sample surface. Droplet size was measured using a Mettler Toledo AL 204 high precision scale with enclosure to be an average of 0.0105 g for DI water with a standard deviation of 0.0009 for 20 measurements. The ambient temperature was measured using a NIST traceable RTD to be 18.165 ±0.04 °C. Using the density of DI water at the measured room temperature resulted in an average droplet diameter of 2.72 mm assuming a spherical drop, which is on the order of the capillary length for water at room temperature. Thus, gravity effects on the droplet could be neglected. A lamp with a diffuser was used to minimize heat input and to provide a uniformly-bright, diffuse background light. The test setup is shown in Figure 6-3.

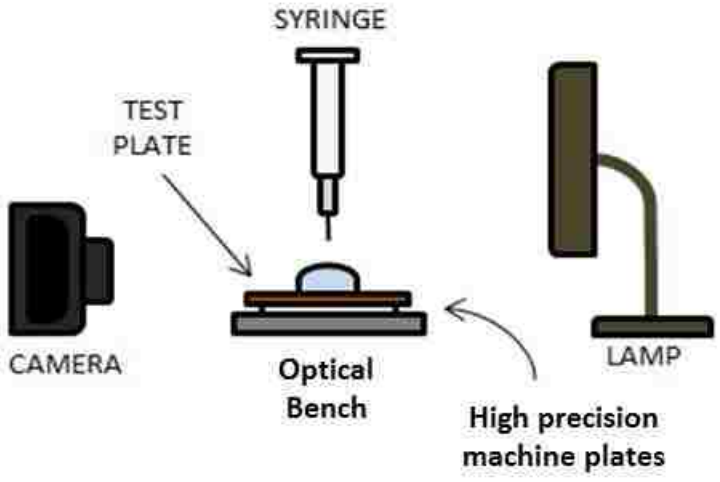

Figure 6-3: Test setup for the sessile drop contact angle and contact angle hysteresis measurements.

Images were taken at 18 uniformly distributed locations on each plate. The syringe was depressed until a small droplet formed and made good contact with the substrate. Droplet size was kept under to 2.7 mm to ensure that gravity effects could be neglected. The droplet was left impaled on the syringe to stabilize the droplet. Applying the droplet without leaving it impaled on the syringe led to an unstable droplet on the hydrophobic and superhydrophobic surfaces that would often roll from a high contact angle area to a more stable lower contact area and often times would roll off of the sample entirely. Also, air currents from the lab air conditioning system would disturb freestanding droplets. Once a stable, well-defined droplet was achieved, the camera was manually focused on the macro setting such that the largest cross section of the droplet was in focus. Special attention was paid to ensure the droplet-surface contact area was centered in the camera image and in-plane with the focal axis to minimize parallax issues affecting the measurement. After the image was taken, the droplet was wicked off of the surface with the tip of a lint-free cloth to avoid abrading or contaminating the surface.

The images were processed using ImageJ[7], which is an open-source, java-based image processing program developed by the National Institutes of Health. For each measurement, the image was opened in ImageJ and then sharpened, cropped, the brightness and contrast adjusted for sharpness, and converted to a grayscale image. After the image was prepared, the contact angle was measured using the DropSnake[8]

[7] National Institutes of Health ImageJ website: imagej.nih.gov/ij/
[8] Ecole Polytechnique Federale de Lausanne DropSnake website: bigwww.epfl.ch/demo/dropanalysis/

plugin, which uses a b-spline to shape the drops and determine the contact angle on both sides of the drop after the user defines the drop outline [213]. DropSnake was chosen over other options because user contour placement provides easier and more accurate processing in most all lighting conditions and because it measures the contact angle on each side of the drop independently [197]. For each image, ten points were manually selected on the droplet perimeter (five on each side of the droplet) and adjusted until the b-spline accurately outlined the droplet shape. The contact angles for each side of the droplet were recorded, and all 18 values were averaged together to form the contact angle for each sample. The averaged contact angle and the standard deviation for each test sample plate are presented in Table 6-1.

Table 6-1: Contact angle values using the sessile drop method.

			Sample 1		*Sample 2*			
Exp	*Surface Texture*	*Surface Treatment*	*Contact Angle*	*Std Dev*	*Contact Angle*	*Std Dev*	*Room Temperature*	*Relative Humidity*
1	Smooth	Uncoated	65.0	0.93	64.5	1.58	71.2 °F	21%
2	Smooth	Aerogel	85.9	8.34	82.5	13.72	72.4 °F	13%
3	Smooth	NeverWet	154.4	1.49	153.3	1.44	69.9 °F	16%
4	μ-ridges	Uncoated	57.0	5.61	49.2	4.67	68.7 °F	18%
5	μ-ridges	NeverWet	160.6	1.73	160.8	1.85	69.9 °F	16%

From the results, a few conclusions can be observed. First, the contact angle for the baseline smooth, uncoated copper plates was in the range of previous text values that are shown on Table 6-2. The values were a little lower than other measurements, but this was most likely attributed to differences in relative humidity especially since the measured values were similar to those of Taft, Smith, and Moulton [85] which had a

similar low relative humidity. Also, as predicted by Wenzel, adding surface roughness through the application of microridges made the samples more hydrophilic and reduced the contact angle by 11°. It should also be noted that the uncoated, microridge samples had much higher variability than the polished sample and was likely caused by non-uniformity in the fabrication process as well as oxidation and contamination on the surface and in the grooves of the samples. From the microscope images of the laser milled surfaces, the laser milled surface did not remain polished, nor was the surface polished after receipt for fear of contamination getting lodged in the grooves from polishing compounds.

Table 6-2: Literature values for the contact angle of water on copper 101 using the sessile drop technique (*Humidity was estimated by Taft, Smith, and Moulton) [85], [87], [214], [215], [216], [217].

Source	*Temperature [C°]*	*Humidity*	*Contact Angle*
Shoji and Zhang 1984	20°	71%*	71°
Yekta-Fard and Ponter 1985	20°	100%*	78°
Extrand 2003	N/A	80%*	69°
Li, Wang et al. 2008	N/A	65%*	74°
Larmour and Hamraoui 2010	20° – 100°	72%*	9° - 74°
Taft, Smith, and Moulton 2014	22°	18%	61.5° ± 3.7°

The second observation from the data is that the contact angle for the aerogel coating was very low for a hydrophobic coating and the standard deviation was very high. The high variability in the measurement was caused by the fragility of the coating on the substrate. The coating was so fragile that using a cloth to wick away the droplet without touching or abrading the surface degraded the coating. Initial measurements were on the order of 100° but after removing a few droplet the contact angle was on the order of

64°. In addition, the coating would quickly wash off the samples. This issues was not noted by Truesdell et al. or Gogte et al. [25], [168] for the aerogel-dipped substrates, and thus, was likely caused by changing substrate materials. The addition of an interface coating between the substrate and the aerogel coating could solve the adhesion problem, but that effort is left to future work. Unfortunately, since the aerogel hydrophobic coating did not adhere well to the copper substrate, it was eliminated from any additional testing. Representative images of the drop shapes are shown in Figure 6-4 through Figure 6-7.

a)  b) 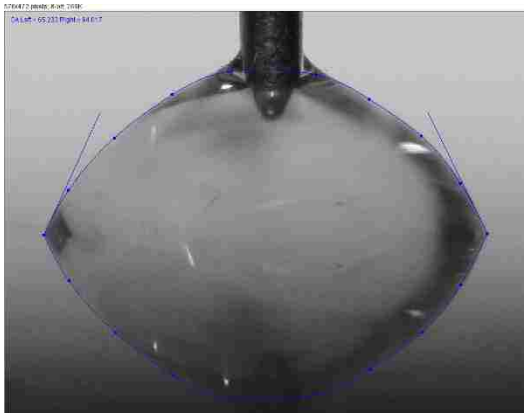

Figure 6-4: Representative images for a droplet on the smooth copper substrate with no coating a) photograph of the droplet and b) as processed image using ImageJ and DropSnake.

a)  b) 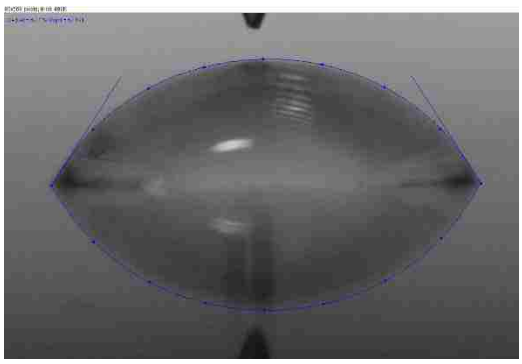

Figure 6-5: Representative images for a droplet on the microridges copper substrate with no coating a) photograph of the droplet and b) as processed image using ImageJ and DropSnake

a) 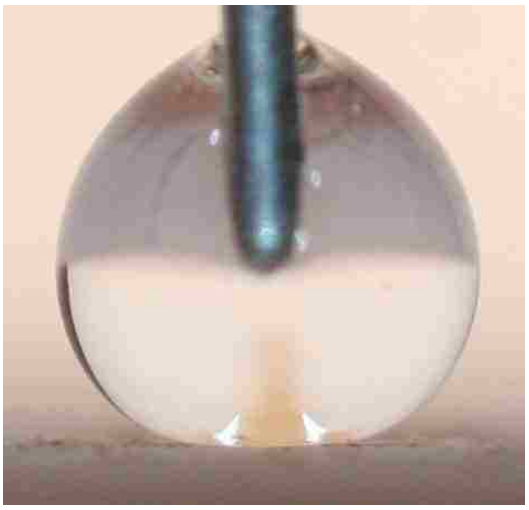 b) 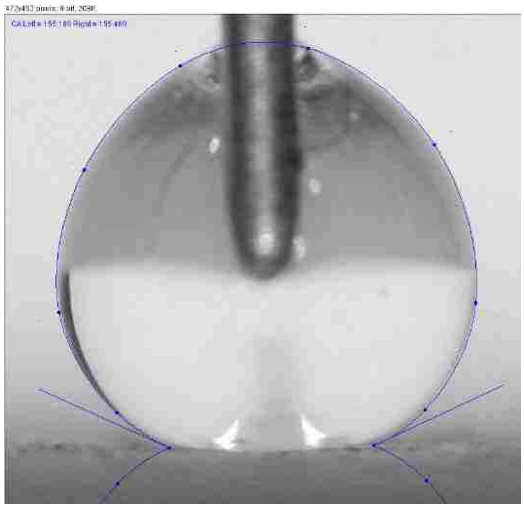

Figure 6-6: Representative images for a droplet on the smooth substrate with the NeverWet® coating a) photograph of the droplet and b) as processed image using ImageJ and DropSnake.

a)  b) 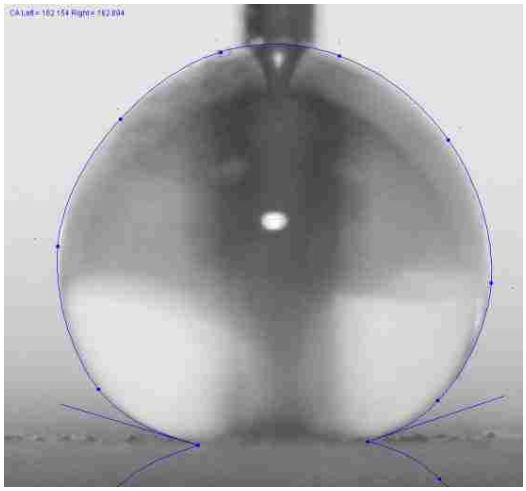

Figure 6-7: Representative images for a droplet on microridges substrate with the NeverWet® coating a) photograph of the droplet and b) as processed image using ImageJ and DropSnake.

6.3 Contact Angle Hysteresis

Many of the same methods used to measure the contact angle can also be used to measure the contact angle hysteresis by slowly moving the solid with respect to the liquid.

For sessile drop approaches, the telescope-goniometer approach can be used, and two main approaches have been used. The first is to use a mechanically driven syringe pump to add or remove fluid to measure the advancing and receding contact angles, respectively. The second approach is to tilt the plate until just before the drop begins to move. The contact angle at the lowest point is the advancing contact angle and the contact angle at the highest point is the receding contact angle. The method was developed by MacDougall and Ockrent [218] and used by Extrand and Kumagai [219], [220] to study contact angle hysteresis of liquids on silicon wafers and polymer surfaces. Similarly, the Wilhelmy balance method can be used by moving the solid up and down in the fluid bath.

To measure the advancing and receding angles, the capillary rise method was initially attempted. The experimental setup used essentially the same setup as before with the same camera, lens, and lighting background as the contact angle measurements. Since a motor to control the movement of the plate in the fluid was not available, fluid was added and removed from the bath using the syringe to change the fluid surface level with respect to the copper plate. The plate was suspended in a clear container of fluid and the syringe was connected to tubing mounted at the base of the beaker to minimize flow effects and disturbances at the surface. Fluid was added to the container to measure the advancing angle and removed with the syringe to measure the receding angle. The camera continuously took images at roughly 4.2 per second, which was the limit of the camera.

It is important to note that the speed at which the contact line moves has an effect on dynamic angle measurements. Both the contact line velocity and acceleration influence the dynamic contact angle in that the dynamic contact angle is larger for higher contact line acceleration [221]. Based on the physical limitations of the camera and syringe, the volumetric flow rate was 5 cm^3/s, which resulted in a contact line velocity of 0.6 mm/s. Using Equation (6-4), the advancing and receding contact angle can be determined from the capillary rise as fluid is added to or removed from the container. For any cases where a capillary depression occurs rather than a rise, which created and advancing angle greater than 90°, a modified equation was used that subtracted the angle from 180°. In addition, the contact angle was calculated from the advancing and receding contact angles using the following equations [222]:

$$\theta_o = \sin^{-1}\left(\frac{\Gamma_A \cos\theta_A + \Gamma_R \cos\theta_R}{\Gamma_A + \Gamma_R}\right) \tag{6-6}$$

where,

$$\Gamma_R = \left(\frac{\sin^3\theta_R}{2 - 3\cos\theta_R + \cos^3\theta_R}\right)^{1/3} \tag{6-7}$$

and,

$$\Gamma_A = \left(\frac{\sin^3\theta_A}{2 - 3\cos\theta_A + \cos^3\theta_A}\right)^{1/3} \tag{6-8}$$

The results from the capillary rise method were extremely poor and inconsistent. The method was not well suited for the sample geometry because the coating did not span

the width of the sample and was only on a 3.8 cm strip in the center. As a result, the advancing and receding contact angles could not be measured. The angles for the copper edges dominated the image and blocked the contact angles on the coated surface. Rotating the samples 90° was attempted to solve this issue since the coating covers edge to edge in the long direction, but this caused distorted values for the microridge machine samples because the ridges were parallel to the fluid rather than perpendicular, which changed the results.

As an alternative, a sessile drop approach was used instead where fluid was added or removed from the droplet with the syringe. A much smaller syringe was used for adding and removing fluid from the droplet to provide better control. The same continuous camera mode setting was used, and the images were evaluated for the point at which the contact line moved to determine the advancing or receding angle. This approach alleviated the geometry issues from the capillary rise method and worked relatively well for the uncoated samples. The results are shown on Table 6-3.

Table 6-3: Results for the advancing and receding angles calculated from the sessile drop approach

Exp	*Surface Texture*	*Surface Treatment*	θ_r	θ_a	*CAH*	*Std Dev*	*Room Temperature*	*Relative Humidity*
1	Smooth	Uncoated	32.2	90.6	48.4	2.4	24.4 °C	11%
3	Smooth	NeverWet	148.9	158.9	10.0	1.4	19.0 °F	27%
4	μ-ridges	Uncoated	23.7	107.9	84.2	2.9	23.8 °C	11%
5	μ-ridges	NeverWet	157.1	160.9	3.9	1.6	19.4 °F	27%

There are a few items of note. First, the results for the smooth, uncoated samples were in relatively good agreement with literature data. Second, as expected, the added

surface roughness from the microridges increased the contact angle hysteresis for the uncoated sample compared to the smooth sample. The receding contact angle was extremely difficult to measure accurately because of it low contact angle. The resulting measurement error was much higher as a result since this method losses accuracy below for contact angles below 20°. The contact angles for the hydrophobic coated samples were also extremely difficult because of the high mobility of the droplet. The contact angle measurements are somewhat suspect because they are within the uncertainty of the static contact angle measurements. It is safe to conclude that the contact angle hysteresis was extremely low for the hydrophobic coated smooth and microridge samples. As are result the droplets were in the Cassie state, thereby satisfying the requirement for superhydrophobicity.

Chapter 7

Slip Flow and Thermal Results

After the surfaces were characterized through contact angle measurements and verified to be superhydrophobic, the next steps were to characterize the hydrodynamic and thermal effects of the various surface treatments. The analysis results from Chapter 4 were used to guide the development of the experiment design and setup. Pressure head measurements from an incline manometer for a parallel plate flow configuration were used to evaluate hydrodynamic slip by comparing the superhydrophobic coated samples to uncoated samples. Thermal performance was evaluated using the same parallel plate configuration submerged in a recirculating ice bath. The results for the hydrodynamic and thermal performance tests for the superhydrophobic surfaces were compared to the baseline uncoated samples, the modeling results presented in Chapter 4, and literature predictions discussed in Chapter 3. This chapter will first present and

describe the experiment setup and then present the results, analysis, and comparison to predictions.

7.1 Hydraulic Slip Measurements

One of the major goals of this research effort was to achieve and measure the hydrodynamic slip resulting from the use of microtextured, superhydrophobic surfaces. To verify that the superhydrophobic samples achieved a slip state, an indirect slip measurement approach was used which compared the pressure loss through the uncoated copper samples to the other samples. The samples were mounted in a parallel plate configuration with a channel height of 0.40 cm. Silicone rubber gaskets were used to separate the plates and seal the channel. Allen head screws were used to compress the gasket to the desired height of 0.4 cm. This approach enabled a consistent water tight seal, but the compliance in the gasket required for sealing led to some inconsistency in the channel height between test samples on the order of ±0.02 cm. In addition, the compression of the gasket material resulted in a reduction of the test section width from to a measured width of 3.45 ±0.01 cm. Even with the reduction in height and width, the aspect ratio of the channel exceeded 8, which was sufficient to ignore the edge effects of the uncoated channel sides.

To ensure the flow in the test section was hydrodynamically fully developed, the inlet section consisted of a long flow adapter section that transitioned the flow from the

circular tubing cross-section to the rectangular cross-section of the parallel plate configuration. The adapter was made using a stereo lithography additive manufacturing process because of the complex internal flow geometry. To ensure the flow was fully developed by the time it entered the test section, the adapter transitioned from the circular to rectangular cross section over a length of 10 cm, and the rectangular section was 19 cm long to satisfy the requirement that the square root of the length must be much larger than the cross-sectional area. The exit section used a similar configuration, but much shorter rectangular cross-sectional region.

A Masterflex L/S peristaltic digital pump with Easy Load II pump head (Model #77921-75) was used to control the flow rate. The pump was calibrated using a 500 mL graduated cylinder and stop watch and was periodically verified during all tests. The flow rate measurements were accurate to less than 2% error. To minimize the flow oscillation effects caused by the peristaltic pump, a gravity feed chamber was used to provide continuous flow to the inlet of the test chamber. A 15 micron filter was used to keep large debris from contaminating the flow chamber and was installed on the pump outlet flow prior to entry to the gravity feed chamber. It was placed on the pump outlet rather than the entry to the test chamber flow adapter to eliminate negative pressure loss effects on the pressure measurements. Between the gravity feed chamber and the inlet to the test chamber, the tubing was teed off and connected to an incline manometer to measure the pressure differential in the test chamber. Because of the low pressure head loss in a 15 cm flow section, a very shallow inclination angle used. The length and rise

height of the manometer were measured and the inclination angle was calculated to be 1.47°. Finally, to maintain a consistent inlet temperature for all test cases regardless of lab conditions, the inlet temperature was maintained at 20 °C using a Neslab RTE 7 circulating temperature bath with digital temperature control. In addition, insulation was used to the maximum extent possible to minimize temperature changes prior to entry to the test section.

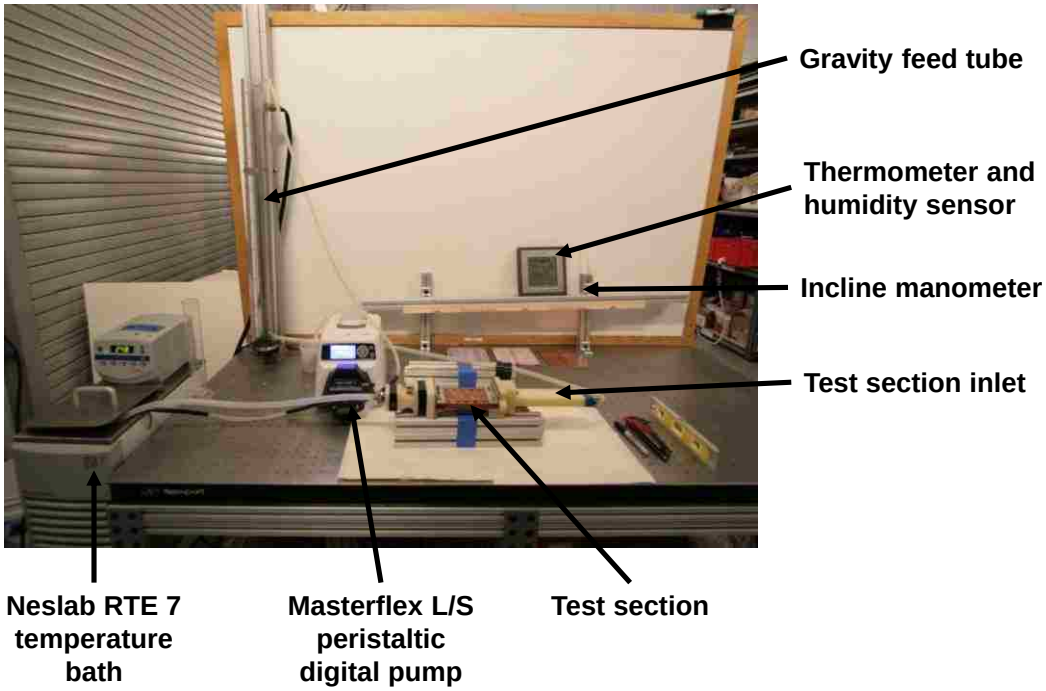

Figure 7-1. Pictures of the test setup for the slip flow experiments

For each test sample, the fluid level height in the incline manometer was measured for flow rates from 60 to 200 mL/min in increments of 20 mL/min. From the pressure measurements the normalized slip velocity was calculated by taking advantage of the flow velocity relationships that: for a given volumetric flow rate, only the velocity profile

changes for no slip and slip flow; the mean velocity is the same. Thus substituting Equation (4-8) into Equation (4-10) and simplifying, the slip velocity yields:

$$u_{slip} = \frac{H^2}{12\mu}\left[\left(\frac{\partial P}{\partial x}\right)_{no\ slip} - \left(\frac{\partial P}{\partial x}\right)_{slip}\right] \tag{7-1}$$

where, u_{slip} is the slip velocity. Normalizing by the mean velocity, using the relation in Equation (4-8), and utilizing that for Poiseuille flow the pressure gradient is only a function of x, yields the following simplified relationship:

$$\frac{u_{slip}}{u_m} = 1 - \frac{\Delta P_{slip}}{\Delta P_{no\ slip}} \tag{7-2}$$

The measurement results calculated from Equation (7-2), and the results are plotted on Figure 7-2 where RU is the microridge uncoated sample, SHD is the smooth sample coated with the superhydrophobic coating, and RHD is the microridge patterned sample coated with superhydrophobic coating.

From Figure 7-2, a few observations can be made. First, the no slip boundary condition held for the smooth, superhydrophobic coated sample across all flow rates tested within the uncertainty of the experimental measurement. Second, the uncoated, microridge patterned sample exhibited higher pressure loss than the uncoated sample, which resulted in an average negative slip length of -0.11 mm. This result conflicts with classical laminar flow theory in that the friction loss and thus pressure head loss for laminar flow is dependent on the Reynolds number and channel geometry and not on the surface roughness. Thus, there is likely an artifact in the test setup or assembly that

increased the pressure loss for the uncoated, microridge patterned sample compared to the uncoated sample and could include an over compressed gasket resulting in a smaller channel height or a disruption in the flow field perturbing laminar flow. In the next section, the heat transfer results for the uncoated, microridge patterned surface were significantly higher than all of the other samples, which supports both hypotheses for the increase in pressure loss.

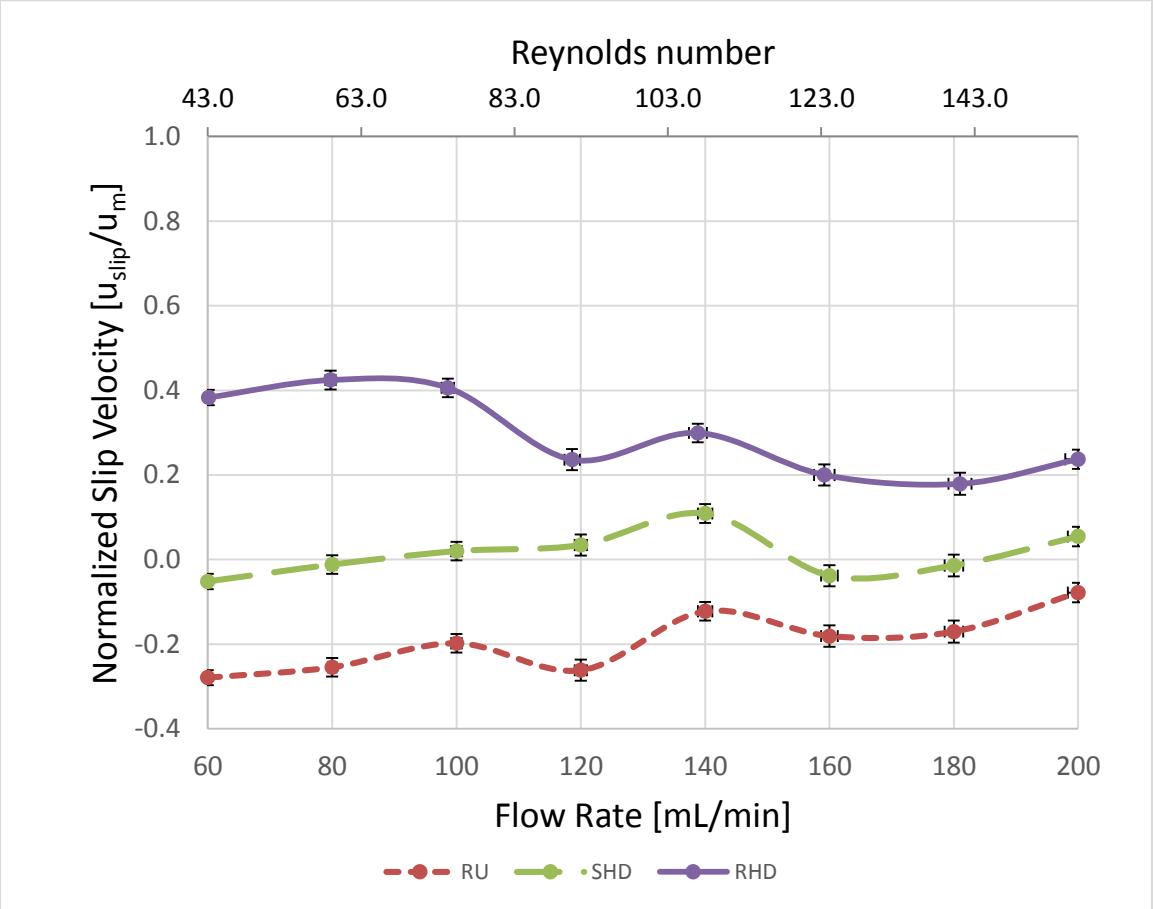

Figure 7-2: Plot of the calculated normalized slip velocity [u_{slip}/u_m] with respect to Reynolds number for the modified samples compared to the baseline uncoated copper sample where RU is the uncoated microridge sample, SHD is the smooth sample coated with the super-hydrophobic coating, and RHD is the microridge sample coated with the superhydrophobic coating.

Finally from Figure 7-2, the superhydrophobic coated, microridge patterned sample exhibited a lower pressure drop than the uncoated smooth baseline sample that resulted in an average normalized slip velocity of 0.30. From Equation (4-6), the velocity profile can be determined using the normalized slip velocity:

$$u(y)_{slip\ BC2} = 6\left[\frac{y}{H} - \left(\frac{y}{H}\right)^2\right] - 6\frac{u_{slip}}{u_m}\left[\frac{y}{H} - \left(\frac{y}{H}\right)^2\right] + \frac{u_{slip}}{u_m} \tag{7-3}$$

Solving Equation (7-3) at y=0 and then taking the derivative and solving at y = 0, yields the equation for the slip length based on the definition from Equation (2-1) and Figure 2-1:

$$\lambda = \frac{H}{6}\left(\frac{u_{slip}}{u_m - u_{slip}}\right) \tag{7-4}$$

Table 7-1 shows the calculated slip velocities and slip length at the various flow rates measured for the microridge patterned, superhydrophobic coated sample, which was the only one where slip was observed.

Table 7-1: The calculated slip velocity and slip length for the microridge patterned, superhydrophobic coated sample.

Flow Rate [mL/min]	*Reynolds Number*	*Slip Velocity [mm/s]*	*Slip Length [mm]*
60	52.0	2.79	0.41
80	69.4	4.12	0.49
100	86.7	4.93	0.46
120	104.1	3.44	0.21
140	121.4	5.09	0.28
160	138.8	3.89	0.17
180	156.1	3.91	0.15
200	173.4	5.76	0.21

7.2 Heat Transfer Measurements

The reasons for developing the numerical model were twofold. The first reason was to develop a tool to predict the effect of the slip boundary condition on heat transfer. The laminar parallel plate flow configuration with constant temperature boundary condition was chosen because it has an analytical solution for the no-slip boundary condition and because it has a fairly straight forward experimental implementation using an ice bath to establish a constant temperature boundary condition. The second reason was to parametrically trade various design parameters to help determine the optimal test configuration based on limitations for fabricating the test samples. It was very challenging to fabricate long test sections, so during experiment design, it was important to maximize the temperature difference between the inlet and outlet sections. The parametric model was used to identify the optimal test conditions to maximize the temperature difference between the plain, uncoated samples and the superhydrophobic samples. Maximizing this difference reduced the impact of experimental uncertainty on the results.

The thermal experiment setup consisted of the same hardware and setup as the pressure loss setup with a few additions for thermal testing. As discussed previously, a constant temperature ice bath was selected to control the boundary condition for the experiment. A mechanical mixer was used to rapidly circulate ice water slurry in the ice bath to enhance heat transfer to better approximate the constant temperature condition.

In reality, a constant temperature boundary condition at 0 °C was not achieved. K-type thermocouples were mounted on each plate at three positions (one inch from the inlet, midpoint of the sample, and one inch from the outlet) to monitor the surface temperature between the plate and the ice bath. The results for all test samples and flow rates are summarized below.

Table 7-2: Summarized thermocouple surface temperatures across all tests.

	Inlet	*Mid*	*Outlet*	*Average*
Average	1.46	1.17	1.08	1.23
StdDev	0.51	0.45	0.49	0.51

The same inlet flow adapters for the inlet and outlet sections used in the pressure drop test setup were also used in the thermal test to ensure hydrodynamically fully developed, laminar flow. The inlet adapter was mounted to the exterior wall of the ice bath, and the sample section was mounted to the interior wall of the ice bath to constrain and focus heat transfer effects into the sample section. Thus, the flow into the sample section was hydrodynamically fully developed but not thermally developed. Using the following approximation for the thermal entry length, the entry length for the lowest flow rate was 0.16 m and was 0.54 m for the highest flow rate. Since the sample test length was 0.15 m, the flow was never fully thermally developed [88]:

$$x_{fd,T,lam} \approx 0.06 Re_{D_h} Pr D_h \tag{7-5}$$

Temperature measurements were made with K-type thermocouples that were calibrated using a multi-point calibration by comparison technique to a NIST-traceable standard platinum resistance temperature device in a water bath. Using this approach,

the thermocouples are accurate to ±0.1 K. A National Instruments data acquisition card connected to a laptop recorded temperatures at 12 locations (2 in the inlet flow, 2 in the outlet flow, 6 mounted to the test samples, one inside the ice bath, and one measuring room temperature), and the full test setup is shown in Figure 7-3.

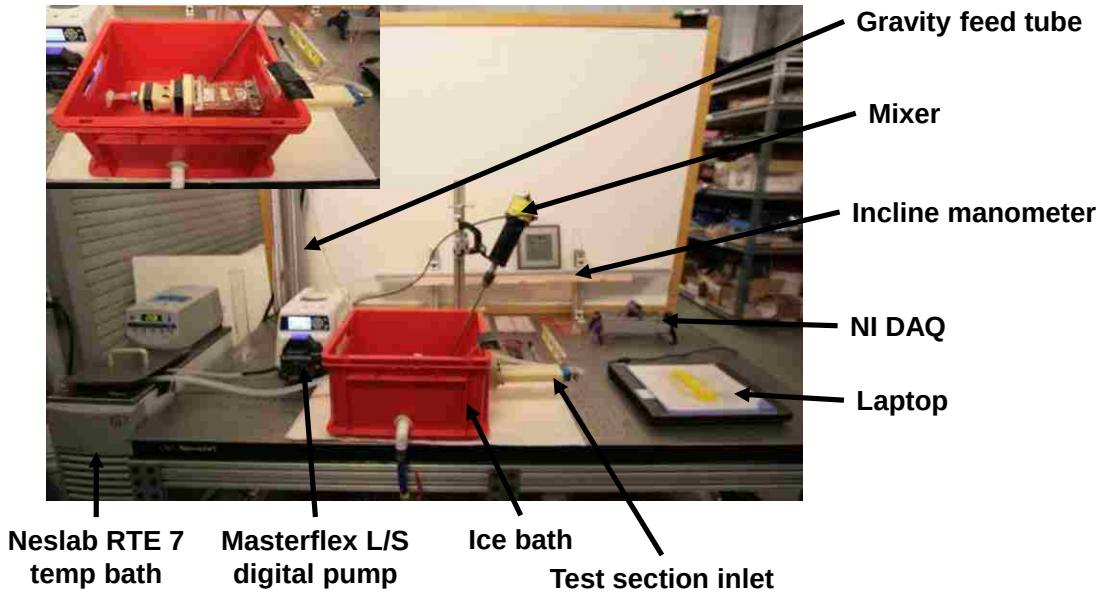

Figure 7-3. Pictures of the experiment test setup

As with the previous testing, inlet and outlet temperature measurements for each test sample were recorded for flow rates from 60 to 200 mL/min in increments of 20 mL/min. For each flow rate, the setup was monitored until steady state was reached. Once at steady state, temperature data was recorded at 2 Hz for one to two minutes. The values were then averaged over the recorded duration. From the temperature measurements, the heat transfer coefficient was calculated using [88]:

$$T_{out} = T_s - (T_s - T_{in})e^{\left(-\frac{pL\bar{h}}{\dot{m}c_p}\right)} \quad (7\text{-}6)$$

where, T_{out} is the mean outlet temperature, T_{in} is the mean inlet temperature, T_s is the surface temperature, p is the channel perimeter, L is the channel length, $\bar{h}$ is the average heat transfer coefficient, $\dot{m}$ is the mass flow rate, and c_p is the heat capacitance of water at constant pressure.

The inlet temperate was taken as the average value of the inlet thermocouples. Since the surface temperature was not maintained at 0 °C, the average temperature across the six thermocouples mounted to the samples was used as the ensemble surface temperature. This approximation results in measurement error and calculation uncertainty as discussed in Appendix C, but the end goal was to compare the baseline samples to the superhydrophobic samples rather than classical theory. As a result of this approach, some measurement and calculation error was eliminated in the final output. Finally, the mean outlet temperature was determined by first calculating the parabolic equation for the curve that passed through the measured surface temperature and the measured outlet temperature thermocouple location. Symmetry of the flow was assumed to calculate the parabolic equation. From the equation, the mean outlet temperature was calculated.

Using the calculated average heat transfer coefficient, the average Nusselt number was determined using:

$$Nu = \frac{\bar{h} D_h}{k} \tag{7-7}$$

The plot of the Nusselt numbers for the various samples are plotted on Figure 7-4 along with the estimated classical Nusselt number from the numerical model. The calculated Nusselt number for the uncoated smooth baseline sample agrees relatively well with the classical Nusselt number for no slip with moderate deviation at higher flow rates. The difference between the values is likely do to experimental uncertainty and the fact that the ice bath did not provide a perfect constant temperature boundary condition at 0 °C. The Nusslet number for the uncoated microridge patterned sample is significantly higher than all of the other measured samples, which is consistent with the higher pressure loss previously discussed. Finally, both superhydrophobic coated samples exhibited enhanced heat transfer compared to the baseline sample with the smooth sample showing improved results above 120 mL/min (Re = 90.5), and the microridge had improved results above 80 mL/min (Re = 59). In addition, the microridge patterned superhydrophobic sample consistently performed better than the smooth superhydrophobic coated sample.

As discussed in Section 7.1, the microridge patterned, superhydrophobic coated sample clearly exhibited hydrodynamic slip. Maynes et al. [64], [65] and Enright et al. [62] predicted, from their modeling efforts, that thermal slip is also likely based on comparisons with wall slip in gas dynamics where a temperature jump occurs at the wall because of reduced heat transfer efficiency caused by the molecular slip at the boundary. Both authors predicted that wall slip would reduce thermal efficiency and result in a lower

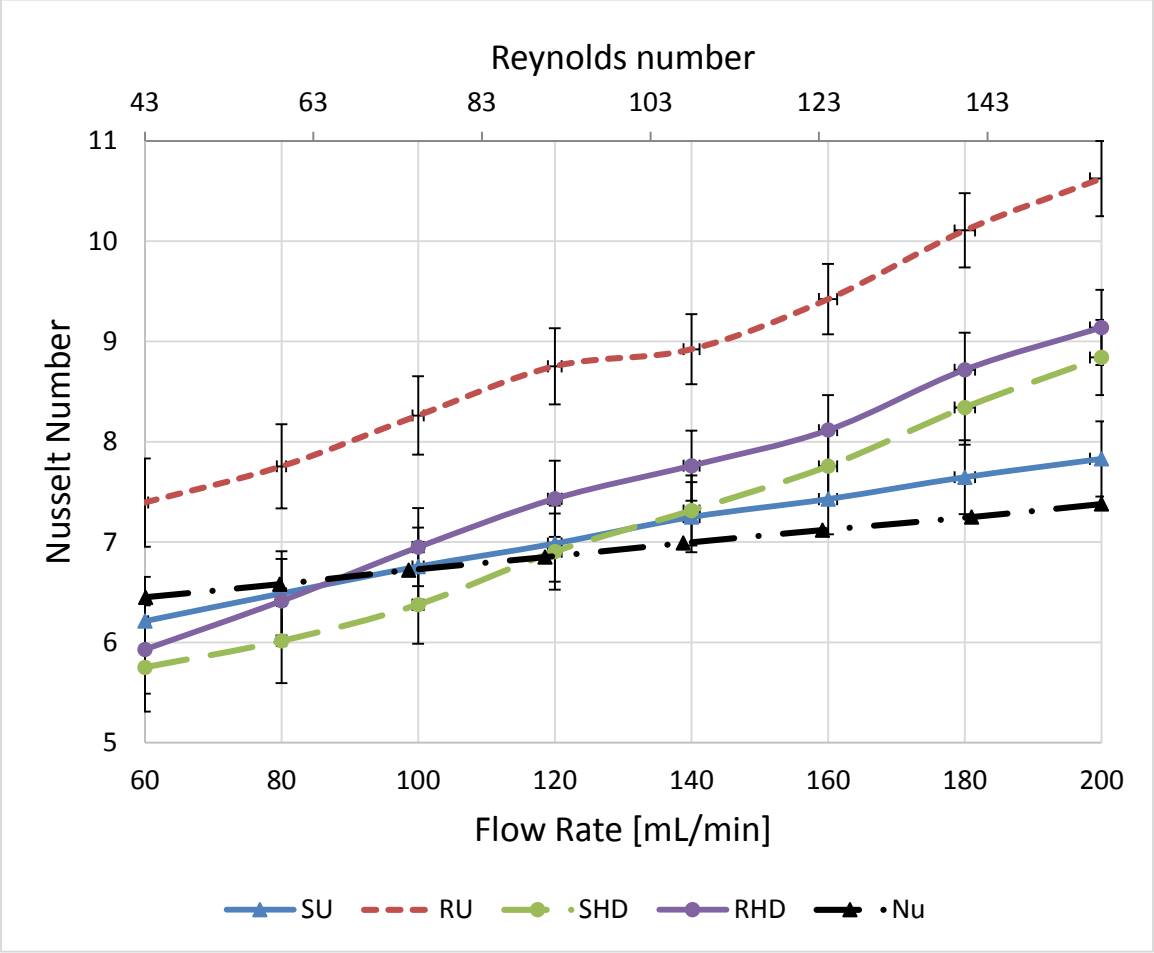

Figure 7-4: Plot of the calculated Nusselt number with respect to Reynolds number for all of the samples where SU is the uncoated smooth sample, RU is the uncoated microridge sample, SHD is the smooth hydrophobic sample, RHD is the hydrophobic microridge and Nu is the classical Nusselt number from the numerical model.

that slip increases the Nusselt number and results in improved heat transfer efficiency unlike in the case of gas dynamics. It is hypothesized that apparent slip in liquids improves convection efficiency by eliminating the low conductivity stagnate layer pinned to the wall and enables convection effects to occur closer to the wall without a temperature jump boundary condition because of the much higher density and thermal conductivity of liquids compared to gases.

The results from the pressure loss and the heat transfer measurements for the samples portray somewhat mixed results especially the uncoated microridge patterned sample. An alternative approach to combine the pressure loss and heat transfer performance into an efficiency factor was proposed by Maynes et al. as noted in Section 3.3 [63]. However, rather than comparing the ratio of the Nusselt number to the friction loss for each surface to the classical value, the modified samples were compared to the baseline, uncoated results. The results of this approach are presented in Figure 7-5. From the figure, a clear distinction in the results becomes obvious with the superhydrophobic coated, microridge patterned surface significantly outperforming the other three samples. In addition, the uncoated microridge sample and the superhydrophobic smooth sample essentially performed the same as the baseline smooth, uncoated sample.

Finally, it should be noted that the overall durability of the hydrophobic coated samples was good. During post-test inspection there was clearly visible degradation of the coatings with obvious signs of discoloration and wear, but the coatings samples remained superhydrophobic based on post-test contact angle measurements. There was no degradation in the contact angle for the hydrophobic coated microridge samples and an average of 5° reduction in contact angle for the hydrophobic coated smooth samples.

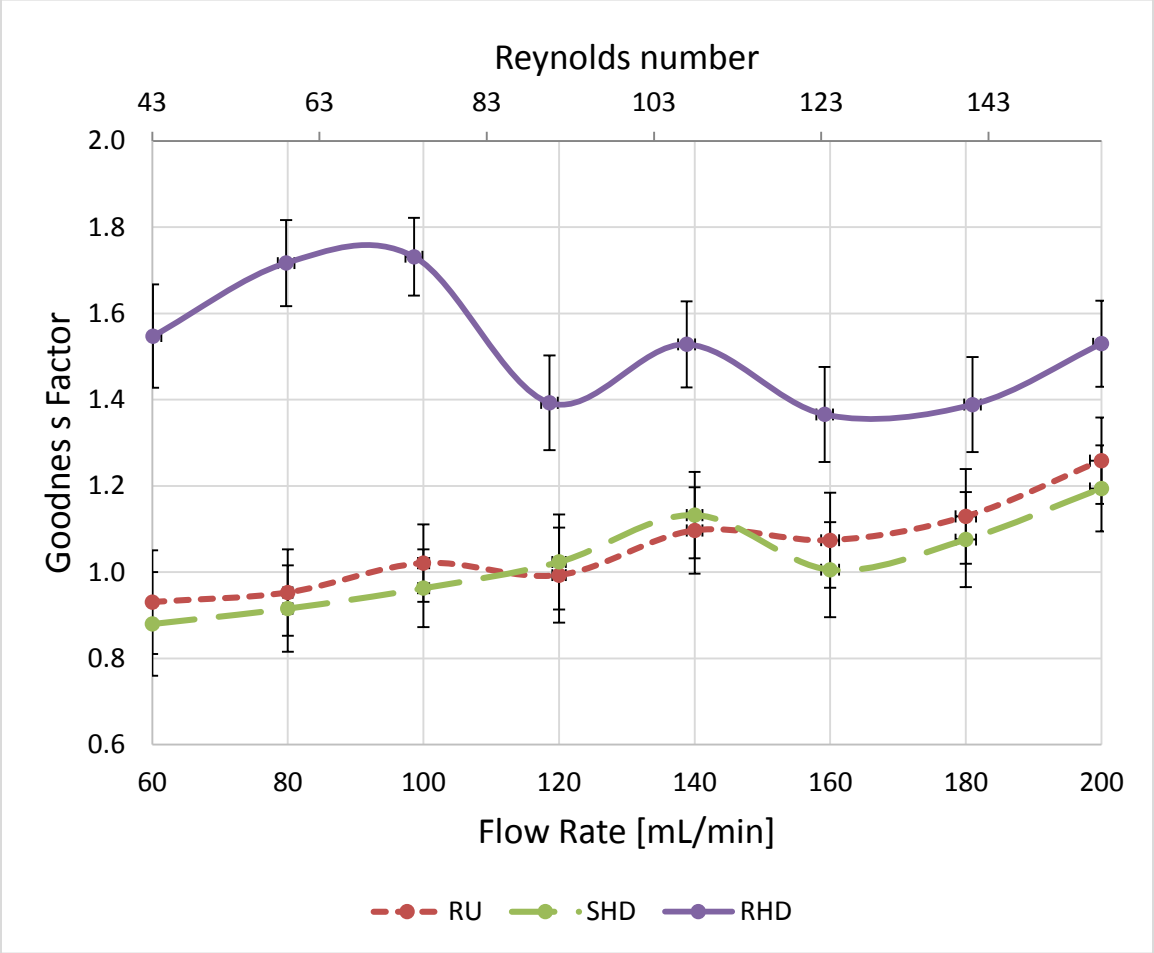

Figure 7-5: Plot of the calculated Goodness factor [Nusselt number/Friction loss] with respect to Reynolds number for the modified samples compared to the baseline uncoated copper sample.

Chapter 8

Conclusions and Future Research

8.1 Summary and Conclusions

From many centuries, researchers have investigated the complex interactions between a solid surface and a fluid in motion relative to the surface. For many cases, the classical no slip boundary condition holds true. However, there are a subset of situations where this assumption is no longer valid, and slip between the surface and fluid must be considered. Situations include gas flow dynamics, contact line motion, and surface energy modified surfaces such as hydrophilic and hydrophobic surfaces. A number of researchers have explored hydrodynamic slip characteristics for hydrophobic and superhydrophobic surfaces. Multiple authors have shown that micropatterned surfaces with hydrophobic coatings achieve a superhydrophobic state that enables slip and results in a decrease in drag and pressure losses for both laminar and turbulent flow. A smaller number of researchers have investigated the effects of slip flow on heat transfer, and most studies

in the open literature are analytically or numerically based. There are very few studies that have experimentally explored slip flow heat transfer for purely hydrophobic coated surfaces and none that have experimentally investigated slip flow heat transfer for micropatterned superhydrophobic surfaces. This work was the first investigation into this area.

The primary goal of this research effort was to experimentally explore the effects of slip flow on laminar convection heat transfer using micropatterned, superhydrophobic surfaces. To achieve that goal, the first step was to design, develop, and fabricate test samples of adequate size, configuration, and durability for experimental investigation. Copper was first chosen as the base material because of its high thermal conductivity, is relatively easy to work with, and is highly applicable to heat transfer devices and applications. Fabricating a micropatterned surface on the copper substrate was fairly straightforward using a laser machining approach, and the resulting surface was consistent and repeatable. Finding a superhydrophobic coating with good adhesion to copper was much more challenging. Initially a hydrophobic coating developed and tested at UNM was attempted, but the adhesion was extremely poor, and the coating did not survive sessile drop contact angle measurements. Eventually, a commercial product, Rust-Oleum® NeverWet®, was found that had good adhesion to the copper substrate to survive laminar flow testing. In total, four sets of sample surfaces were fabricated and tested: uncoated smooth, uncoated microridge patterned, superhydrophobic coated smooth, and superhydrophobic coated microridge patterned. Contact angle

measurements were made on all of the test samples to ensure the coated plates were superhydrophobic and the uncoated plates were not.

In parallel to sample fabrication, numerical models to predict and estimate the thermal performance of the no slip and slip boundary conditions were created. A Crank-Nicolson approach was first developed in Matlab, but under some parameters, temperature oscillations at the wall occurred. To fix this problem, the numerical model was changed from a Crank-Nicolson approach to one using Matlab's built in ODE45 function. This eliminated temperature oscillations at the wall under all conditions. The numerical model predicted heat transfer enhancement for the slip boundary condition, which was consistent with other models in the literature assuming that the hydrodynamic slip condition does not also create a thermal slip condition and a temperature jump at the boundary as many literature models predict. Investigating the thermal condition at the wall was important for this effort.

Using the model predictions as a guide, the experiment setup was designed to try to maximize the temperature difference between the no slip and slip boundary conditions based on the limitations of the test sample fabrication size. An ice bath was used to simulate a constant temperature boundary condition, and only low flow rates were studied because of the short heat transfer length. The results indicate that slip was only achieved on the micropatterned, superhydrophobic coated sample with an average slip length of 0.30 mm. As for the thermal results, the superhydrophobic coating appeared

to enhance heat transfer rather than hinder it. Finally, the efficiency ratio, which is a measure comparing heat transfer performance and friction loss performance, clearly showed improvement for the micropatterned, superhydrophobic coated sample over the baseline sample. The uncoated micropatterned and the superhydrophobic smooth samples performed similarly to the baseline sample.

From these findings, a few conclusions were made. First, only the micropatterned, superhydrophobic coated sample achieved a slip state. Second, hydrodynamic slip was observed without the accompaniment of thermal slip and a temperature jump boundary condition since the heat transfer performance for the superhydrophobic sample was as good as or better than the baseline sample for all flow rates tested. This result was contradictory to literature predictions that hydrodynamic slip would be accompanied by thermal slip at the boundary similar to slip flow in gas dynamics. It was hypothesized that the reason for this dissimilarity between fluid slip flow and gas slip flow is a result of the much higher density and thermal conductivity of liquids compared to gases. In addition, it was concluded that micropatterned superhydrophobic surfaces reduce pressure loss and heat transfer as seen by the improved efficiency factor and thus makes them a good candidate for small and microscale devices where pressure losses can be significant. The ability to control interfacial flow through the use of micropatterning and surface modification, whether it be for hydrophilic or hydrophobic surfaces, in macro and micro systems opens up a wide range of potential design parameters for engineers to truly

design and control properties and the micro- and nanoscales. Finally and in conclusion, the three objectives outlined in Chapter 1 have been accomplished.

Objective 1: Develop and fabricate micro-patterned, superhydrophobic surfaces using copper, aluminum, or other relevant heat transfer surfaces

Objective 2: Investigate the effect of hydrophobicity and superhydrophobicity on friction loss and heat transfer performance for laminar flow

Objective 3: Determine and calculate hydrodynamic and thermal slip on a superhydrophobic surface and compare that to existing analytical and numerical models

8.2 Future Research

The experimental work presented here provided an initial investigation into the thermal effects of slip flow on superhydrophobic surfaces. This first look proof-of-principle was focused on either supporting or refuting the various models and approaches put forward in the literature, but it by no means conclusively supports any one prediction. There are still many more experiments and configurations that need to be explored. To begin with, only one surface pattern was tested. The microridge configuration oriented in the streamwise direction is likely the most conducive pattern for improving both friction loss and heat transfer performance because of the continuous three-phase contact line in the velocity direction. Micropost, microhole, and transverse microridge patterns have a discontinuous three-phase contact line in the flow direction, which could significantly impact both the friction loss and heat transfer performance. A near term

area of investigation should be to explore the pressure loss and thermal effects of the other micropattern features discussed in the literature.

In addition to the limited exploration of surface patterns, only one microridge configuration was investigated (25 μm x 25 μm). Explorations modifying the pitch and cavity fraction should also be investigated to better understand the effect of slip on friction loss, heat transfer, and the combination of the two. Increasing the cavity fraction improves friction loss until the surface is no longer able to support the fluid in the Cassie state. However, contrary to friction loss, increasing the cavity fraction should reduce heat transfer performance because of the reduced surface area contact with the fluid. Understanding the tradeoff between these parameters will be required to fully optimize systems for both pressure loss reductions and heat transfer enhancements.

Another parameter that should be expanded in future work is the Reynolds number. This effort explored a fairly small span of Reynolds number from 40 to 160 for a proof of principle effort because of the challenges and limits of heat transfer experiments and sample fabrication. Expanding the exploration to higher Reynolds numbers in the laminar regime and ultimately into the transition and turbulent regimes. This expansion will require a combination of more robust hydrophobic coatings (including durability and usage temperature) and the ability to make longer test samples to increase the heat transfer length and improve the temperature differential for higher flow rates. The predictions by Maynes et al. and Enright et al. indicate that the heat transfer performance

and the pressure loss enhancement are functions of Reynolds number with a local maximum performance [62], [64], [65]. Investigating that possibility should be the focus of an expanded experiment for laminar flow.

Finally, alternative experiment approaches should be explored. Using Indirect friction loss measurements and temperature measurements in the bulk fluid provide a macroscopic overview of the physics occurring at the interface, but a direct measurement that combines measurements for slip length, slip velocity, heat transfer measurements at the interface, and temperature distribution in both the streamwise and surface normal directions would greatly enhance the understanding of fluid flow and heat transfer for laminar slip flow using superhydrophobic surfaces. Micro-PIV experiments have shown excellent quality for capturing flow characteristics including slip length and slip velocity, and Hsieh et al. added micro laser-induced fluorescence (μLIF) for combined flow and temperature visualization [167]. The key for any temperature measurement approach is that the accuracy must at least 0.1 K, and ideally would be much less, because of the high impact of uncertainty on the Nusselt number for small temperature differentials and length scales. It is unclear if current tracer particles have the accuracy required over a wide enough temperature range to eliminate sufficient experimental uncertainty to accurately compare no slip and slip flow boundary conditions over a wide array of test conditions. Ultimately, this is research area is in its infancy with a wide range of potential options to explore. This effort showed through a first proof of principle experiment that

further exploration is warranted because of the potential improvement in pressure loss and heat transfer for macro-, micro-, and possibly nanofluidic applications.

Appendix A: 2012 AIAA Aerospace Sciences Conference Paper

50th AIAA Aerospace Sciences Meeting including the New Horizons Forum and Aerospace Exposition
09 - 12 January 2012, Nashville, Tennessee

AIAA 2012-0528

Effect of Slip Flow on Heat Transfer: Numerical Analysis

Andrew D. Williams,[1] Peter Vorobieff,[2] and Andrea Mammoli,[2]
University of New Mexico, Albuquerque, NM 87131

This paper presents numerical analysis that investigates the effect a slip boundary condition has on heat transfer. Multiple researchers have shown that superhydrophobic surfaces, those with a contact angle greater than 150° and contact angle hysteresis less than 5°, have demonstrated drag reduction for both laminar and turbulent flow on the order of 20% to 50% and slip lengths up to 50 times larger than the feature length. This effort seeks to take a first step into understanding the effect that slip has on heat transfer. A 2-D parallel plate setup was evaluated. The velocity profile was analytically solved and used to determine the thermal profile using the Crank-Nicolson finite difference approach. The numerical results reveal that increasing the slip length improves heat transfer for a (h) 1.3 cm x (L) 15.2 cm parallel plate configuration. In addition, the temperature difference decays exponentially with Reynolds number, and a maximum temperature difference of 3.78 K between the no slip and 2 mm slip boundary conditions occurs at a Reynolds number of 90.

Nomenclature

c	=	thermal capacitance of the fluid
C	=	constant of integration
g	=	gravitational acceleration
H	=	channel height
L	=	heated length
u	=	velocity in the x-direction
M	=	number of nodes in the x-direction
N	=	number of nodes in the y-direction
k	=	thermal conductivity of the fluid
P	=	pressure
r	=	ratio between the actual surface area of a rough solid and its projected surface area
t	=	time
T	=	fluid temperature
T_{in}	=	temperature at the channel inlet
T_m	=	mean temperature
T_{out}	=	temperature at the channel outlet
T_s	=	surface temperature
u	=	velocity in the x-direction
u_m	=	average velocity in the x-direction
$u_{no\ slip}$	=	velocity in the x-direction for no slip boundary condition
u_{slip}	=	slip velocity at the solid-fluid boundary
$u_{slipBC1}$	=	velocity in the x-direction for slip on only one boundary
$u_{slipBC2}$	=	velocity in the x-direction for slip on both boundaries
v	=	velocity in the y-direction
W	=	channel width
θ	=	Young's contact angle
θ_c	=	contact angle
θ^*	=	apparent contact angle
θ_m	=	normalized mean temperature
ρ	=	fluid density
μ	=	dynamic viscosity
φ_s	=	fraction of the solid in contact with a droplet resting on the surface

[1] PhD candidate, Department of Mechanical Engineering, AIAA Senior Member
[2] Associate Professor, Department of Mechanical Engineering, 1 University of New Mexico, MSC01 1150

I. Introduction

Virtually all undergraduate mechanical engineering students and most professional engineers accept that the boundary condition for fluid flow over a solid surface to be no slip. However, very few know the details regarding the heated debate that occurred during the 18th and 19th century prior to the acceptance of the no slip boundary condition (NSBC). A review of the history of this discussion was provided by Goldstein[1]. The NSBC was first proposed in 1738 by Daniel Bernoulli to account for errors between his calculations for a perfect fluid and experimental results. In the 19th century, three hypotheses were put forward: 1) Coulomb stated that the fluid velocity at the boundary of a solid is the same as the solid and changes continuously in the fluid, 2) Girard believed that there was a stagnant layer between the solid and the bulk fluid and that at the interface between the stagnant layer and the bulk fluid slip occurred, and 3) Navier deduced that slip occurs at the boundary and is proportional to the stress[1]. Ultimately, the NSBC was accepted in part because it could not be disproven by measurement devices of the time. However, over time, Navier's hypothesis that slip occurs at the interface was shown to be accurate and that Bernoulli's NSBC is an acceptable approximation without loss of accuracy for most cases.

Maxwell was the first to predict and quantify the slip length as being on the order of the mean free path of the fluid [b=O(1 nm)], and it was Tolstoi in 1952 and then Blake in 1990 that provided the rigor to this theory[2]. Schnell produced the first experimental evidence suggesting slip by measuring the flow rate of water in glass capillaries treated to be hydrophobic[3]. Thompson and Troian were the first to demonstrate that surface hydrophobicity can produce slip lengths larger than the mean free path using molecular dynamic simulations[4]. More recently, studies have focused on superhydrophobic surfaces, which are surfaces that combine hydrophobic coatings, such as Teflon, and micro-patterned surfaces to achieve contact angles greater than 150° and contact angle hysteresis less than 5°. Examples of superhydrophobic surfaces are presented in Figure 1.

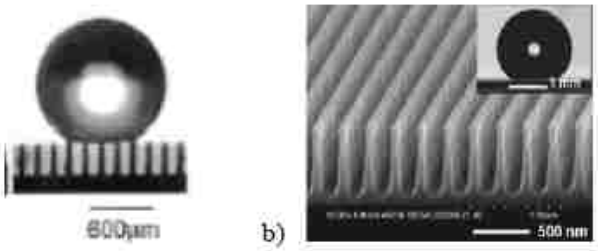

Figure 1. a) Photograph of a liquid droplet on a superhydrophobic surface utilizing micro-posts[5] b) scanning electron microscope image of a micro-patterned surface consisting of lengthwise ridges[6]

A number of experimental studies have since confirmed the importance of superhydrophobicity on fluid slip and have tried to quantify drag reduction, the magnitude of the slip length, the parameters that affect it, and means to enhance it.

II. Background

Superhydrophobic Surfaces

Surfaces are either hydrophilic ($\theta_c < 90°$) or hydrophobic ($\theta_c > 90°$) depending on the contact angle, θ_c, made by a water droplet on the surface. Superhydrophobic ($\theta_c > 150°$) surfaces were inspired by the lotus leaf and are achieved through a combination of hydrophobic surfaces or coatings and micro- and nano-scale surface roughness[7]. The addition of surface roughness influences the contact angle hysteresis (CAH), which is the difference between the advancing and receding contact angles. For small CAH, droplets become unstable to small perturbations; whereas, for large CAH, droplets are pinned. From this, it is important to note that the CAH is the critical parameter and not the contact angle for determining the effective slip that can be expected for a surface.

Based on the CAH, there are two states possible for superhydrophobic surfaces: one with high adhesion and one with high slip. For the high adhesion, or Wenzel, state water penetrates the surface roughness to fully wet the surface[8]. For the high slip, or Cassie, state the fluid is supported by surface tension and spans the roughness thereby minimizing the contact area with the surface[9]. A diagram for both states is shown in Figure 2. For the Wenzel state, the CAH is on the order of 110°; whereas, for the Cassie state, it is on the order of 5°[10].

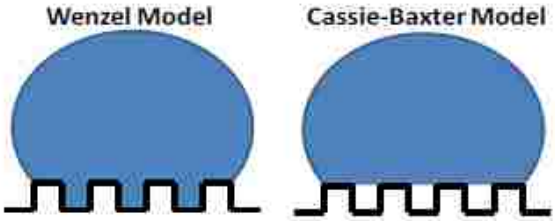

Figure 2. Diagram of a superhydrophobic surface in the Wenzel and Cassie-Baxter states

For the Wenzel state, the apparent contact angle is denoted as:

$$\cos\theta^* = r\cos\theta \tag{1}$$

where θ is Young's contact angle, and r is the ratio between the actual surface area of a rough solid and its projected (or apparent) surface area. For the Cassie state, the apparent contact angle is denoted as:

$$\cos\theta^* = -1 + \varphi_s(\cos\theta + 1) \tag{2}$$

where φ_s defines the fraction of solid remaining in contact with the drop. The transition point between the states is dependent on r and φ_s and occurs when $\cos\theta_c = (\varphi_s - 1)(r - \varphi_s)$, which corresponds to matching points in both regimes[10]. The two states predict different behavior as shown in Figure 3 where the steep line denotes the Wenzel state, the shallow line denotes the Cassie state, and the dashed line denotes a metastable Cassie state in the Wenzel regime.

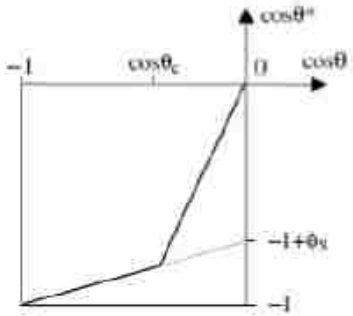

Figure 3. Relationship for the Wenzel, Cassie, and metastable Cassie states within the Wenzel regime[10]

In addition to the above, the contact state also depends on the formation of the droplet on the surface[10]. If a droplet is deposited in such a way that air is trapped between droplet and the surface, a metastable Cassie state can be achieved. However, if vapor is condensed on the surface, then a Wenzel state is more likely. A Wenzel state can also be achieved by forcing fluid into the cavities. As such, it is important to not only design a slip surface to induce air trapping but also to ensure that the Cassie state is the preferred state. This is especially true for pressurized systems.

Previous Research

Research into superhydrophobic surfaces for fluid slip has focused on four primary areas: droplet behavior, drag reduction for both laminar and turbulent flow and maximizing slip length for laminar flow. In the area of droplet behavior, Oner and McCarthy investigated the effects on hydrophobicity of various micro-post parameters including post height, geometry, silanizing agent, post cross-sectional area, and pitch by measuring the advancing and receding contact angles and minimum tilt angle[11]. From their measurements, they observed that 1) spacing between 2 and 32 μm between features exhibited superhydrophobic behavior; 2) spacing between 64 and 128 μm exhibited liquid intrusion and droplet pinning; 3) increasing the perimeter-to-area ratio of the post diminishes the hydrophobic

behavior of the surface; and 4) hydrophobicity was independent of post height and silanizing agent. From these observations, they concluded that the key issue for enhancing hydrophobicity and thus increasing surface slip was the structure of the three phase (solid-liquid-vapor) contact line including shape, length, continuity of contact, and amount of contact.

Yoshimitsu and colleagues furthered the understanding of droplet behavior on superhydrophobic surfaces by investigating the sliding effect of water droplet size on various surface structures[5]. They determined that sliding behavior occurred when roughness was greater than 1.23, and droplet pinning occurs when roughness was less than 1.10. They also compared sliding behavior for micro-post and micro-ridge geometries. The geometry providing the lowest sliding angle were micro-ridges oriented parallel to the flow direction followed by micro-posts and micro-ridges orthogonal to the flow. This supports observations that sliding behavior depends on the length and continuity of the three-phase interface line where a continuous, short three-phase contact line is preferred.

In the area of drag reduction, numerous authors have investigated multiple surface geometries, hydrophobic coatings, and measurement techniques with drag reduction ranging from 20% to 40% for laminar flow, and slip lengths an order of magnitude greater than feature spacing[12,13,14]. From observations, pressure drop increased linearly with flow rate and monotonically decreased with increasing post spacing. In addition, pressure drop was found to increase linearly with increasing channel height. Because of these observations, it was hypothesized that the reduction in pressure drop was attributed to a shear-free liquid-vapor interface between posts supported by the surface tension of the water as shown in Figure 4. When compared to analytical, empirical predictive correlations, and CFD results, good agreement for the velocity profile within the bounds of the experimental error have been obtained[15,16,17]. As for pressure drop reduction, solutions provide good qualitative agreement with the experimental results, but quantitatively, they under predicted for all cases.

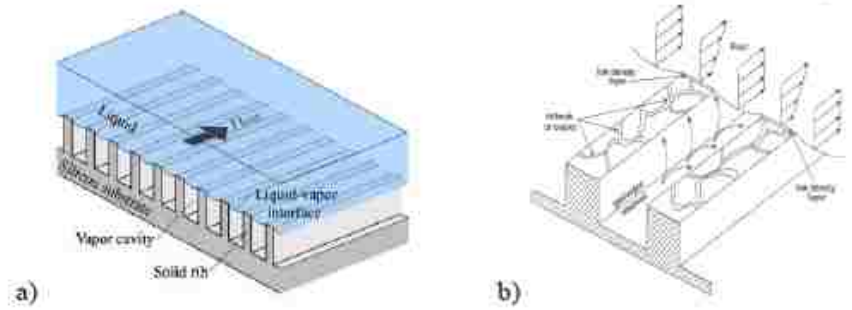

Figure 4. a) Fluid flow over a superhydrophobic surface and the three-phase (solid-liquid-vapor) interfaces[18] b) Slip enhancement through the introduction of microcracks[19]

As for efforts seeking to maximize slip length for pressurized flows, a number of authors have engineered various micro-patterned surface structures to maximize fluid slip. For high pressure flow on the order of 100 kPa, multiple authors have reported slip lengths an order of magnitude longer than the feature size with maximum values of 140 μm for micro-posts and 400 μm for micro-ridges[6,20,21]. For low pressure flow on the order of 5 kPa, a maximum slip length greater than 50 times the feature size has been reported[14].

The majority of the work relating to the effect of superhydrophobic surfaces in turbulent flow has been to determine the drag reduction rather than the effective slip length of the surface. Martell and colleagues used numerical simulation to determine the effect of superhydrophobic surfaces on turbulent flow[22]. They studied both micro-post and micro-ridge geometries, and their results predict increasing drag reduction with increasing feature spacing, which is consistent with reducing the three phase contact line length. However, they also found that post geometries provide higher slip velocities and larger shear stress reductions than ridge geometries, which is contrary to the results for laminar flow[22]. In addition, Martell's numerical simulations also predict that unlike laminar flows increasing the flow rate and Reynolds number results in an increase in drag reduction in turbulent flow.[23] These predictions are consistent with results presented by Daniello and colleagues, where the friction coefficient decreased with increasing Reynolds number until reaching a maximum of ~50% at which point it leveled off[24]. From these results, they hypothesized that the proper scaling dimension was the viscous sub-layer thickness and that the onset of drag reduction occurs when the viscous sub-layer thickness approached the micro-feature size[24].

III. Numerical Analysis Method

The advantage of these surfaces for fluid and cooling applications, especially micro-fluidic systems, is drag reduction and thus reduced pumping power required for these systems. However, the question remaining for micro-cooling applications is: what is the effect of the slip boundary condition on the convective heat transfer? The slip boundary condition should locally enhance heat transfer because the non-zero velocity at the interface enables both convection and fluid conduction near the surface such that heat is transported away from the surface in a more efficient manner. However, micro-patterning the surface reduces the solid-liquid contact area, which reduces heat transfer. Identifying which is the more dominate parameter is key to understanding the potential heat transfer enhancement that can be achieved through the use of superhydrophobic coatings. This paper seeks to take the first step by evaluating the effect that slip flow has on heat transfer for two-dimensional flow between parallel plates. The effect of heat transfer area reduction is not considered.

For flow between parallel plates, the velocity profile for each of the three possible boundary condition cases can be determined analytically. The input parameters and problem setup are shown in Figure 5. The test section consisted of an adiabatic entry region to provide hydrodynamically fully developed flow prior to entry into the heated section.

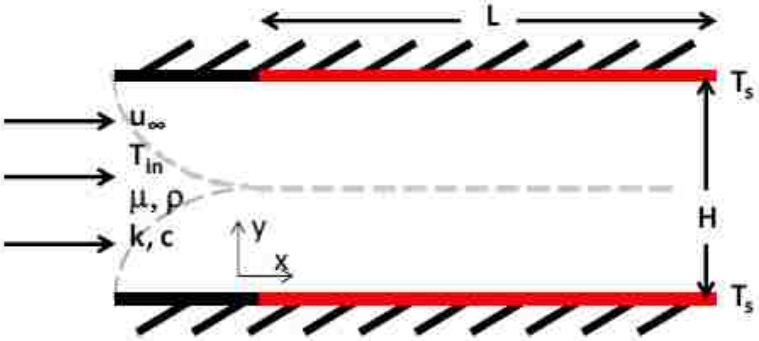

Figure 5. Parallel plates setup and inputs for analytical analysis with an unheated entry section to allow for hydrodynamically, fully developed flow before entry into the heated length

The general equation for conservation of momentum is:

$$\rho\left[\frac{\partial u}{\partial t}+u\frac{\partial u}{\partial x}+v\frac{\partial u}{\partial y}\right]=-\frac{dP}{dx}+\mu\left[\frac{\partial^2 u}{\partial y^2}+\frac{\partial^2 u}{\partial x^2}\right]+\rho g_x \tag{3}$$

where ρ is the density of the fluid [kg/m^3], u is the velocity in the x-direction [m/s], v is the velocity in the y-direction [m/s], t is time [s], P is pressure [Pa], μ is the dynamic viscosity of the fluid [kg/m-s], and g is the acceleration caused by gravity [m/s^2]. Assuming steady state, horizontal, fully developed flow, constant cross section, and boundary layer simplifications, the conservation of momentum equation reduces to:

$$\left[\frac{\partial^2 u}{\partial y^2}\right]=\frac{1}{\mu}\frac{dP}{dx} \tag{4}$$

Integrating twice yields:

$$u=\frac{1}{2\mu}\frac{dP}{dx}y^2+C_1y+C_2 \tag{5}$$

Applying the boundary conditions for the three cases and solving for the constants yields:
Case 1: u = 0 at y = 0, y = H

$$u_{no\ slip}=6u_m\left[\frac{y}{H}-\left(\frac{y}{H}\right)^2\right] \tag{6}$$

Case 2: $u = u_{slip}$ at $y = 0$; $u = 0$ at $y = H$

$$u_{slip\,BC1} = 6u_m\left[\frac{y}{H} - \left(\frac{y}{H}\right)^2\right] - u_{slip}\left[4\left(\frac{y}{H}\right) - 3\left(\frac{y}{H}\right)^2 - 1\right] \tag{7}$$

Case 3: $u = u_{slip}$ at $y = 0$, $y = H$

$$u_{slip\,BC2} = 6u_m\left[\frac{y}{H} - \left(\frac{y}{H}\right)^2\right] - 6u_{slip}\left[\frac{y}{H} - \left(\frac{y}{H}\right)^2\right] + u_{slip} \tag{8}$$

where u_m is the average velocity at x [m/s], H is the distance between the plates [m], and u_{slip} is the slip velocity at the boundary [m/s]. For the special case of plug flow, Case 3 reduces to:

$$u_{plug} = u_m \tag{9}$$

The general thermal energy balance equation is:

$$\rho c\left[\frac{\partial T}{\partial t} + u\frac{\partial T}{\partial x} + v\frac{\partial T}{\partial y}\right] = k\left[\frac{\partial^2 T}{\partial x^2} + \frac{\partial^2 T}{\partial y^2}\right] + \dot{g}_v''' \tag{10}$$

where c is the specific heat [J/kg-K], T is the temperature of the fluid [K], k is the thermal conductivity of the fluid [W/m-K], and $\dot{g}_v'''$ is:

$$\dot{g}_v''' = \mu\left[\left(\frac{\partial u}{\partial x} + \frac{\partial u}{\partial y}\right)^2 + 2\left[\left(\frac{\partial u}{\partial x}\right)^2 + \left(\frac{\partial u}{\partial y}\right)^2\right]\right] \tag{11}$$

Assuming steady state; hydrodynamically, fully developed flow; axial conduction is small compared to lateral conduction i.e. Peclet number is large; and viscous dissipation is small i.e Brinkman number is small, the thermal energy balance equation reduces to:

$$\rho c\left[u\frac{\partial T}{\partial x}\right] = k\left[\frac{\partial^2 T}{\partial y^2}\right] \tag{12}$$

Solving the thermal energy balance using Crank-Nicolson finite difference numerical approximation in the y-directions leads to:
Node 1 (bottom):

$$\frac{\partial T_1}{\partial x} = \frac{k}{\rho c u_1 \Delta y^2}(T_2 - 3T_1 + 2T_s) \tag{13}$$

Nodes 2 through N-1:

$$\frac{\partial T_i}{\partial x} = \frac{k}{\rho c u_i \Delta y^2}(T_{i-1} - 2T_i + T_{i+1}) \tag{14}$$

Node N (top):

$$\frac{\partial T_N}{\partial x} = \frac{k}{\rho c u_N \Delta y^2}(T_{N-1} - 3T_N + 2T_s) \tag{15}$$

The Crank-Nicolson approach was selected because it is an implicit, second-order method that is numerically stable. The approach is unconditionally stable, but the solution can oscillate if the step size ratio is too large.

IV. Thermal Analysis Results

The parameters for the analysis are summarized in Table 1.

Table 1. Analysis parameters

Parameter	Symbol	Value	Units
Channel height	H	0.013	m
Heated channel length	L	0.152	m
Channel width	W	0.038	m
Inlet temperature	T_{in}	330	K
Surface temperature	T_s	274	K
Number of y nodes	N	21	
Number of x nodes	M	100	

The velocity profile with respect to the y-direction and the thermal profile with respect to the x-direction are presented in Figure 6 for each of the boundary conditions. The velocity and temperature profiles for the no slip and plug flow boundary conditions agree with theory and validate the accuracy of the Crank-Nicolson approach and step size for the problem. The temperature profile is based on the mean temperature of the fluid for each position along the length of the channel.

$$\mathbf{T_m} = \frac{1}{\mathbf{Hu_m}} \int_0^{\mathbf{H}} \mathbf{uTdy} \tag{16}$$

The integrand of Eq. 16 is evaluated for each node, and the integral is approximated as a summation in the numerical analysis. The slip lengths were 0.5, 1, 1.5, and 2 mm. The Reynolds number based on the flow parameters in Table 1 was 470. From the figure, it is clear that as the slip length increases, the heat transfer increases.

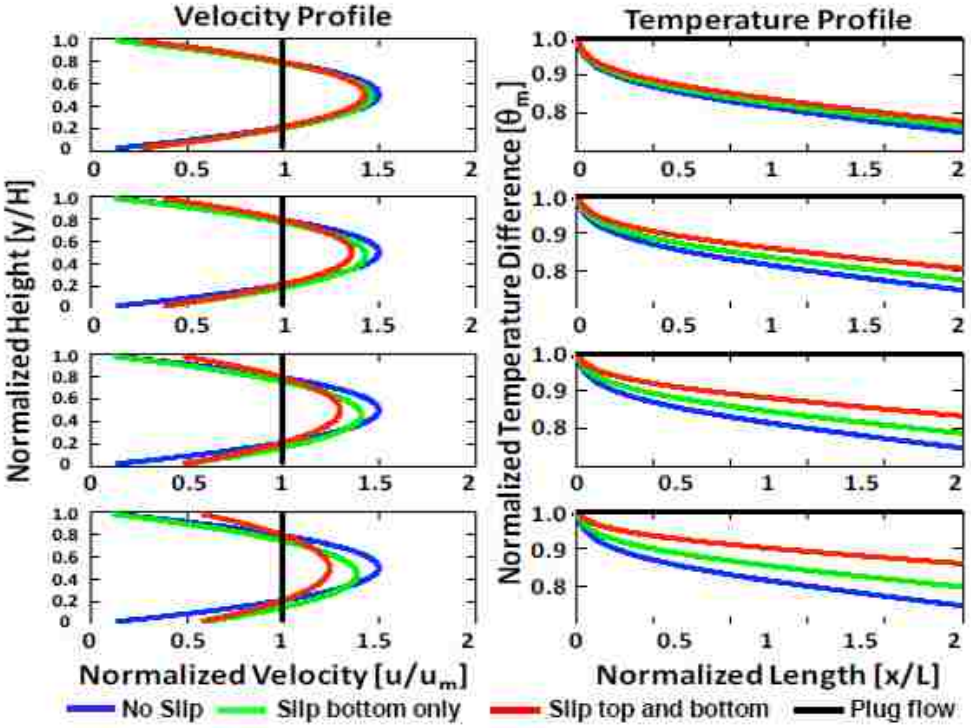

Figure 6. Velocity profile with respect to y and thermal profile with respect to x for parallel plates with channel height of 0.013 m for slip lengths of 0.5, 1, 1.5, and 2 mm for each of boundary conditions

The local Nusselt number for each of the flow conditions is shown in Figure 7, which clearly shows the increased heat transfer for the plug flow and slip flow conditions compared to the no slip condition.

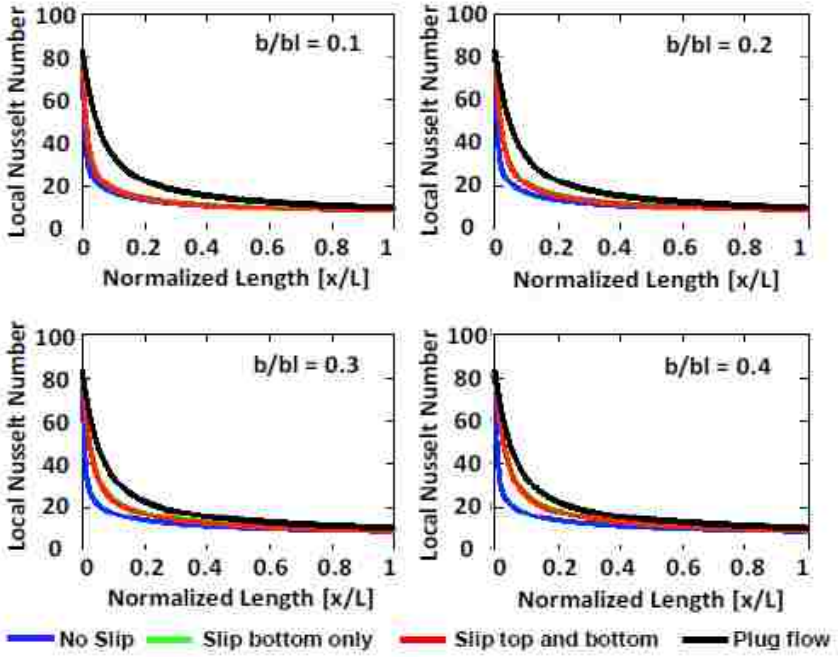

Figure 7. Local Nusselt number with respect to x for each slip length and slip condition. b/bl is defined as the slip length divided by the boundary layer thickness

The temperature differences between the inlet and outlet temperature for the range of laminar Reynolds numbers for each slip length for Case 3 are shown in Figure 8.

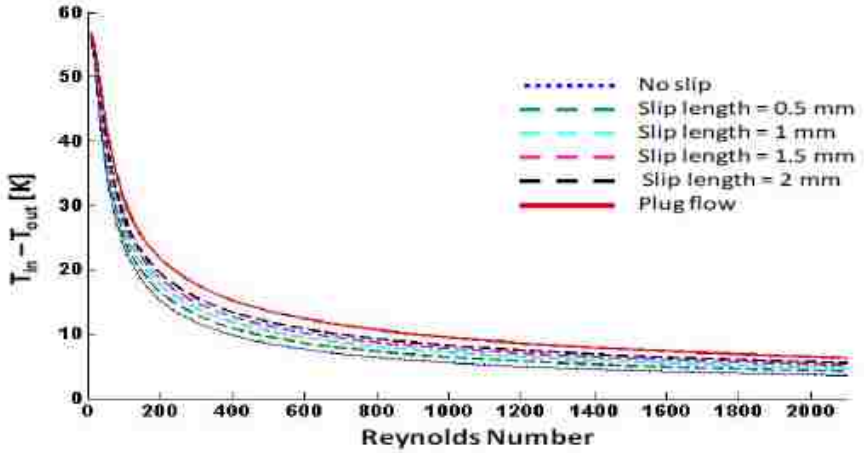

Figure 8. The effect of inlet velocity on the temperature difference for each slip length evaluated

As expected for very low Reynolds numbers, the temperature difference for all of the cases is the same at the limiting case of uniform temperature at the channel exit. However, as flow rate increases, the temperature difference decays exponentially. The maximum temperature difference between the no slip condition and the 2 mm slip length condition is shown in Figure 9. The maximum temperature differential of -3.78 K occurs at a Reynolds number 90, which corresponds to a flow rate of 0.9 mL/s. For the ideal case where the channel height is the same as the slip length, or twice the slip length for the parallel plate configuration, plug flow will occur and the maximum temperature difference of -7.30 K occurs at a Reynolds number of 364.

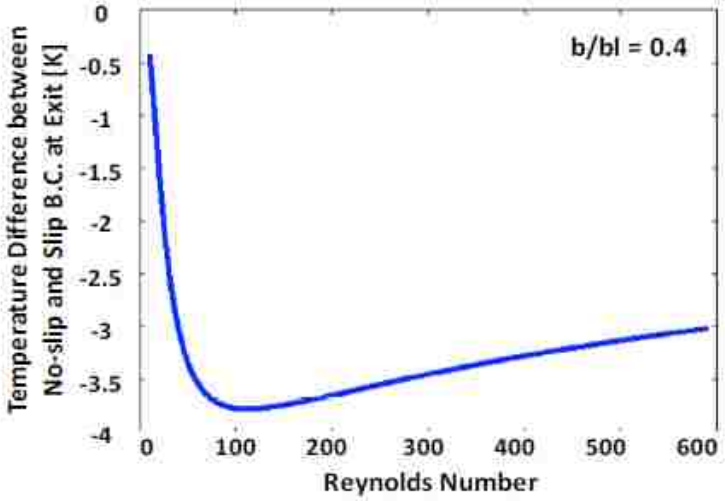

Figure 9. The maximum temperature difference between the no slip and 2 mm slip cases with respect to Reynolds number

Finally, the temperature difference between the no slip and the slip boundary conditions at the exit of the channel was evaluated for all slip lengths ranging from 0 to 6.5 mm. As can be seen on Figure 10, the effect of slip length asymptotically increases to the plug flow solution.

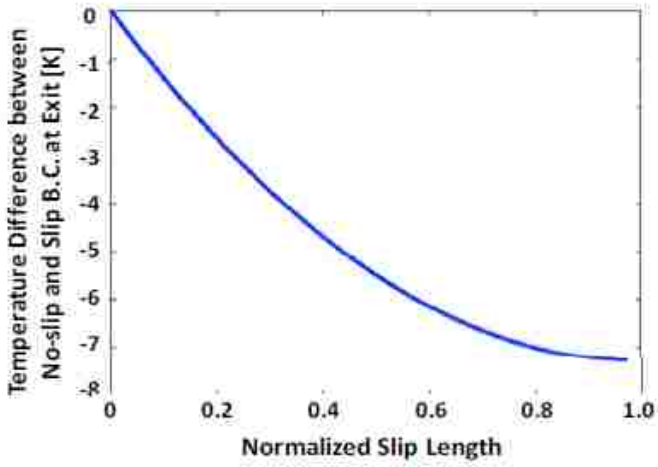

Figure 10. Temperature difference between the no slip and slip boundary condition at the channel outlet for the range of slip lengths between 0 and 5 mm

V. Conclusions and Future Work

This paper discussed the numerical analysis to evaluate the effect of the slip boundary condition on heat transfer using micro-patterned, superhydrophobic surfaces. The velocity profile was analytically solved and used to determine the thermal profile using the Crank-Nicolson finite difference approach. The numerical results reveal that increasing the slip length improves heat transfer and that heat transfer increased asymptotically to the plug flow case for a (h) 1.3 cm x (L) 15.2 cm parallel plates. In addition, the temperature difference between the inlet and outlet temperature decays exponentially with respect to the Reynolds number, and a maximum temperature difference of 3.78 K between the no slip and 2 mm slip boundary conditions occurs at a Reynolds number of 90 for this configuration. As the channel height approaches the plug flow case for a 2 mm slip boundary condition, the temperature difference is -7.30 K at a Reynolds number of 364.

The next step in the development will be to extend the numerical analysis to a three-dimensional model that takes into consideration the effect that the reduction in the liquid-solid contact area has on heat transfer as well as heat conduction effects in the z-direction. Because of the complexity of the analysis, this will likely be done through CFD analysis. In addition to the numerical analysis, experimental data will be collected for various surface geometries to verify and compare the numerical results.

Acknowledgments

This research was sponsored in part by the Air Force Office of Scientific Research (AFOSR).

References

[1] Goldstein, S. ed, *Modern Developments in Fluid Dynamics: An Account of Theory and Experiment Relating to Boundary Layers, Turbulent Motion and Wakes*, Dover, New York, 1965, pp. 702.

[2] Rothstein, J., "Slip on Superhydrophobic Surfaces," *Annual Review of Fluid Mechanics*, Vol. 42, 2009, pp.89-109.

[3] Schnell, E., "Slippage of Water over Nonwettable Surfaces," *Journal of Applied Physics*, Vol. 27, 1965, 1149-1152.

[4] Thompson, P., Troian, S., "A General Boundary Condition for Liquid Flow at Solid Surfaces," *Nature*, Vol. 389, 1997, pp. 360-362.

[5] Yoshimitsu, Z., Nakajima, A., Watanabe, T., Hashimoto, K., "Effects of Surface Structure on the Hydrophobicity and Sliding Behavior of Water Droplets," *Langmuir*, Vol. 18, 2002, pp. 5818-5822.

[6] Choi, C.H., Ulmanella, U., Kim, J., Ho, C.M., Kim, C.J., "Effective Slip and Friction Reduction in Nanograted Superhydrophobic Microchannels," *Physics of Fluids Vol.* 18, 2006.

[7] Barthlott, W., Neinhuis, C., "Purity of the Sacred Lotus, or Escape from Contamination in Biological Surfaces," *Planta*, Vol. 202, 1997, pp. 1–8.

[8] Wenzel, R.N., "Resistance of Solid Surfaces to Wetting by Water," *Industrial and Engineering Chemistry* Vol. 28, 1936, pp. 988–94.

[9] Cassie, A.B.D., Baxter, S., "Wettability of Porous Surfaces," *Transactions of the Faraday Society*, Vol. 40, 199 pp. 546–51.

[10] Qu'er'e, D., Luafuma, A., Bico, J., "Slippy and Sticky Microtextured Solids," *Nanotechnology*, Vol. 14, 2003, pp. 1109-1112.

[11] Oner, D., McCarthy, T.J., "Ultrahydrophobic Surfaces: Effects of Topography Length Scales on Wettability," *Langmuir*, Vol. 16, 2000, pp. 7777–82.

[12] Wantanabe, K., Takayama, T., Ogata, S., Isozaki, S., "Flow between Two Coaxial Rotating Cylinders with Highly Water-repellent Wall," *American Institute of Chemical Engineers Journal*, Vol. 49, No. 8., 2003.

[13] Ou, J., Perot, J.B., Rothstein, J.P., "Laminar Drag Reduction in Microchannels using Ultrahydrophobic Surfaces," *Physical Fluids Journal*, Vol. 16, 2004, pp. 4635–60.

[14] Truesdell, R., Mammoli, A., Vorobieff, P., van Swol, F., Brinker, C.J., "Drag Reduction on a Patterned Superhydrophobic Surface," *Physics Review Letters*, Vol. 97:044504, 2006.

[15] Philip, J.R., "Integral Properties of Flows Satisfying Mixed No-slip and No-shear Conditions," *Journal of Mathematical Physics*, Vol. 23, 1972, pp. 960–68.

[16]Ou, J., Rothstein, J.P., "Direct Velocity Measurements of the Flow Past Drag-reducing Ultrahydrophobic Surfaces," *Physical Fluids Journal*, Vol. 17:103606, 2005.
[17]Woolford, B., Prince, J., Maynes, D., Webb, B.W., "Particle Image Velocimetry Characterization of Turbulent Channel Flow with Rib Patterned Superhydrophobic Walls," *Physics of Fluids*, Vol. 21:08516, 2009.
[18]Jeffs, K., Maynes, D., Webb, B., "Prediction of Trubulent Channel Flow with Superhydrophobic Walls Consisting of Micro-ribs and Cavities Oriented Parallel to the Flow Direction," *Journal of Heat & Mass Transfer*, Vol. 53, 2009, pp. 786-96.
[19]Truesdell, R., *Modification of the Non-slip Boudnary Condition by Superhydrophobic Wall Patterning*, University of New Mexico Ph.D. Dissertation, 2006.
[20]Choi, C.H., Kim, C.J., "Large Slip of Aqueous Liquid Flow over a Nanoengineered Superhydrophobic Surface," *Physical Review Letters*, Vol. 96:066001, 2006.
[21]Lee, C., Kim, C.J., "Maximizing the Giant Liquid Slip on Superhydrophobic Microstructrures by Nanostructuring their Side Walls," *Langmuir*, Vol. 25(21), 2009, pp. 12812-12818.
[22]Martell, M.B., Perot, J.B., Rothstein, J.P., Direct Numerical Simulations of Turbulent Flows over Superhydrophobic Surfaces," *Journal of Fluid Mechanics*, Vol. 620, 2009, pp. 31–41.
[23]Martel, M.B., Rothstein, J.P., Perot, J.B., "An Analysis of Superhydrophobic Turbulent Drag Reduction Mechanisms using Direct Numerical Simulation," *Physics of Fluids*, Vol. 22:065102, 2010.
[24]Daniello, R., Waterhouse, N.E., Rothstein, J.P., "Turbulent Drag Reduction using Superhydrophobic Surfaces," *Physics of Fluids*, Vol. 21:085103-1, 2009.

Appendix B: Matlab Thermal Models

B.1 Matlab Thermal Analysis Program [88]

```
clear all; format compact; hold on

%Input parameters
V_inf = 200;                                %Volume flow rate [mL/min]
slip_length = 0;                           %Slip length [m]

%Experiment parameters
H = 0.004;                                  %Channel height [m]
L = 6*2.54/100;                             %Channel length [m]
W = 0.0345;                                 %Channel width [m]
T_in = 293.2;                               %Inlet temp [K]
T_s = 273.15;                               %Surface temp [K]

u_m = V_inf/60/H/W*1e-6;                    %Inlet velocity [m/s]

%Flow parameters
[rho] = H2Oprops('rho',T_in);               %Density of water [kg/m^3]
[mu] = H2Oprops('mu',T_in);                 %Viscosity of water
[k] = H2Oprops('k',T_in);                   %Thermal conductivity
[c] = H2Oprops('Cp_P',T_in);                %Specific heat
[Pr] = H2Oprops('Pr',T_in);                 %Prandtl number
D_h = 2*H*W/(H+W);                          %Hydraulic diameter
Re = rho*u_m*D_h/mu;                        %Reynolds number
Pe = Re*Pr;                                 %Peclet number
Be = mu*u_m.^2/(k*(T_s - T_in));            %Brinkman number
X_fd_t_lam = 0.06*Re*Pr*D_h;                %Entry length
```

```
%Setting up coordinate grid in x an y
M = 1000;
dx = L/(M-1);                               %Node width [m]
for j = 1:M
    x(j) = dx*(j-1);
end

N = 101;                                    %Number of Y nodes
Dy = H/N;                                   %Distance between nodes
for i = 1:N
    y(i) = Dy*(i-0.5);                      %Position of each node
end

%Velocity node vector
u_slip = 4*u_m*(slip_length/H - (slip_length/H)^2);
for i = 1:N
    if slip_length == 0
        u(i) = 6*u_m*(y(i)/H - (y(i)/H)^2);
    elseif slip_length >= H/2
        u(i) = u_m;
    else
        u(i) = 6*u_m*(y(i)/H - (y(i)/H)^2) - 6*u_slip*(y(i)/H - ...
            (y(i)/H)^2) + u_slip;
    end
end

%Crank-Nicolson Numerical Model
%[T]=dTdx_CN_function(T_in,Dy,dx,H,u_m,u,T_s,N,M);

%ODE45 Numerical Approach
OPTIONS = odeset('RelTol',1e-6);
[x,T] = ode45(@(x,T)dTdx_ODE45_function(x,T,Dy,k,rho,c,u,T_s),[0,L],...
    T_in*ones(N,1),OPTIONS);

[M,g] = size(T);                             %Number of length steps used

%Heat transfer calculations
for j = 1:M
    T_mean(j) = sum(T(j,:).*u)*Dy/(H*u_m);
    qf(j) = k*(T_s - T(j,1))/(Dy/2);
    htc(j) = qf(j)/(T_s - T_mean(j));
    Nusselt(j) = htc(j)*2*H/k;
end

%Average properties
h_mean = -log((T_mean(j)-T_s)/(T_in-T_s))*V_inf/60*1e-
6*rho*c/L/(2*H+2*W);
Nu_mean = h_mean*D_h/k
[rho] = H2Oprops('rho',T_mean(j));          %Density of water [kg/m^3]
[mu] = H2Oprops('mu',T_mean(j));            %Viscosity of water
Re_out = rho*u_m*D_h/mu;
Re_avg = (Re + Re_out)/2
```

```
plot(T(j,:),y)
```

B.2 Matlab ODE45 Function Thermal Model [88]

```
function[dTdx]=dTdx_ODE45_function(x,T,Dy,k,rho,c,u,T_s)
    %Inputs
    % x = position [m]
    % T = node temperatures [K] (vector form)
    % Dy = y node spacing [m]
    % k = thermal conductivity [W/m-K]
    % rho = density [kg/m^3]
    % c = specific heat capacity [J/kg-K]
    % u = node veolicities [m/s] (vector form)
    % T_s = surface temperature [K]

    [N,g] = size(T);                %Setup array size based on nodes
    dTdx = zeros(N,1);              %Initialize array
    dTdx(1) = k*(T(2) + 2*T_s - 3*T(1))/(rho*c*Dy^2*u(1));
    for i = 2:(N-1)
        dTdx(i) = k*(T(i+1) + T(i-1) - 2*T(i))/(rho*c*Dy^2*u(i));
    end
    dTdx(N) = k*(T(N-1) + 2*T_s - 3*T(N))/(rho*c*Dy^2*u(N));
end
```

B.3 Matlab Crank-Nicolson Function Thermal Model [88]

```
function[T]=dTdx_CN_function(T_in,Dy,dx,H,u_m,u,T_s,N,M)
    %Inputs
    % T_in = Inlet Temperature [K]
    % Dy = y node spacing [m]
    % dx = x node spacing [m]
    % H = Channel Height [m]
    % u_m = Average Velocity [m/s]
    % u = node veolicities [m/s] (vector form)
    % T_s = surface temperature [K]
    % N = number of nodes in y direction
    % M = number of nodes in x direction

%Initial temperature condition
T(:,1) = T_in*ones(1,N);              %Temperature at entry
```

```
%Step through space
for j = 1:(M-1)
    %Determining water properties based on mean temp
    T_i = sum(T(:,j).*u')*Dy/(H*u_m);
    [rho] = H2Oprops('rho',T_i);          %Density of water [kg/m^3]
    [mu] = H2Oprops('mu',T_i);            %Viscosity of water
    [k] = H2Oprops('k',T_i);              %Thermal conductivity
    [Cp_P] = H2Oprops('Cp_P',T_i);        %Specific heat

    %Setting up the Crank-Nicholson matrix
    C1 = rho*Cp_P*Dy^2;
    A(1,1) = 1 + 3*k*dx/(2*C1*u(1));
    A(1,2) = -k*dx/(2*C1*u(1));
    for mm = 2:(N-1)
        A(mm,mm-1) = -k*dx/(2*C1*u(mm));
        A(mm,mm) = 1 + k*dx/(C1*u(mm));
        A(mm,mm+1) = -k*dx/(2*C1*u(mm));
    end
    A(N,N) = 1 + 3*k*dx/(2*C1*u(N));
    A(N,N-1) = -k*dx/(2*C1*u(N));

    %Stepping through space
    b(1) = T(1,j) + k*dx*(T(2,j) + 4*T_s - 3*T(1,j))/(2*C1*u(1));
    for jj = 2:(N-1)
        b(jj) = T(jj,j)+k*dx*(T(jj+1,j)+T(jj-1,j)-
2*T(jj,j))/(2*C1*u(jj));
    end
    b(N) = T(N,j) + k*dx*(T(N-1,j) + 4*T_s - 3*T(N,j))/(2*C1*u(N));
    T(:,j+1) = A\b';
end
T = T';
```

Appendix C: Uncertainty Analysis

The following code shows how the slip velocity, heat transfer coefficient, Nusselt number, efficiency factor, and related uncertainty were calculated. The summarized values are below.

Parameter	*Error*
Length [mm]	± 0.03
Height [mm]	± 0.2
Width [mm]	± 0.1
Volume [mL]	± 1
Time [s]	± 0.5
Volumetric flow rate [mL/min]	± 0.83%
Temperature [K]	± 0.1
Pressure head height [mm]	± 1
Slip velocity	± 9%
Heat transfer coefficient	± 9%
Nusselt number	± 11%
Efficiency factor	± 14%

```
clear all; format compact;

%Assigning input values
Q_in = [60 80 100 120 140 160 180 200];          %Flow rate in [ml/min]
```

```
T_out = [278.84 280.15 281.53 282.54 283.68 284.37 284.71 285.17];
DPnoslip = [15.4 16.5 20.2 23.3 29.4 31.5 35.2 42.2];
DPslip = [9.5 9.5 12.0 17.8 20.6 25.2 28.9 32.2];

%Experiment parameters
t = 60;                                 %Flow rate measurement time [s]
H = 0.004;                              %Channel height [m]
W = 0.0345;                             %Channel width [m]
L = 6*2.54/100;                         %Channel length [m]
T_in = 292.6;                           %Inlet temperature [K]
T_s = 273.15+1.23;                      %Surface temperature [K]

%Measurement uncertainty
u_V = 1*1e-6;               %Uncertainty in volume measurement
u_t = 0.5;                  %Uncertainty in time measurement (1st order)
u_measure = 0.00001;        %Uncertainty in length measurements
u_head = 1;                 %Uncertainty in the pressure head height
u_T = 0.1;                  %Uncertainty in temperature measurements
u_L = 0.001*2.54/100;       %Uncertainty in sample length
u_H = 0.2/1000;             %Uncertainty in channel height
u_W = 0.1/1000;             %Uncertainty in channel width

%Uncertainty in length parameters
    %Cross-sectional area in [m^2]
    A = H*W;
    U_A = sqrt((u_H*W)^2 + (u_W*H)^2);

    %Perimeter in [m]
    per = 2*H + 2*W;
    U_per = sqrt((u_H*2)^2 + (u_W*2)^2);

    %Hydraulic diameter [m]
    Dh = 4*A/per;
    dDh_dA = 4/per;
    dDh_dper = -4*A/per^2;
    U_Dh = sqrt((U_A*dDh_dA)^2 + (U_per*dDh_dper)^2);

for j = 1:length(Q_in)
%Uncertainty in flow
    %Flow rate
    V = Q_in(j);                            %Measured fluid volume
    Q = Q_in(j)/60*1e-6;
    U_Q = sqrt((u_V/V)^2 + (u_t/t)^2)*Q;
    U_Q_mL(j) = U_Q*60/1e-6;

    %Fluid properties - viscosity
    [mu_in] = H2Oprops('mu',T_in);              %Viscosity at inlet
    [mu_s] = H2Oprops('mu',T_s);                %Viscosity at surface
    [mu_out] = H2Oprops('mu',T_out(j));         %Viscosity at outlet
    mu_avg = (mu_in+mu_out+2*mu_s)/4;           %Linear average water
    U_mu = std([mu_in,mu_s,mu_out,mu_s])/sqrt(4);
```

```
    %Fluid properties - density
    [rho_in] = H2Oprops('rho',T_in);              %Density at inlet
    [rho_s] = H2Oprops('rho',T_s);                %Density at surface
    [rho_out] = H2Oprops('rho',T_out(j));         %Density at outlet
    rho_avg = (rho_in+2*rho_s+rho_out)/4;         %Linear average water
    U_rho = std([rho_in,rho_s,rho_out,rho_s])/sqrt(4);

    %Fluid properties - heat capacity
    [c_in] = H2Oprops('Cp_P',T_in);           %Specific heat at inlet
    [c_s] = H2Oprops('Cp_P',T_s);             %Specific heat at surface
    [c_out] = H2Oprops('Cp_P',T_out(j));      %Specific heat at outlet
    c_avg = (c_in+2*c_s+c_out)/4;             %Linear average water
    U_c = std([c_in,c_s,c_out,c_s])/sqrt(4);

    %Fluid properties - thermal conductivity
    [k_in] = H2Oprops('k',T_in);               %Conductivity at inlet
    [k_s] = H2Oprops('k',T_s);                 %Conductivity at surface
    [k_out] = H2Oprops('k',T_out(j));          %Conductivity at outlet
    k_avg = (k_in+2*k_s+k_out)/4;              %Linear average water
    U_k = std([k_in,k_s,k_out,k_s])/sqrt(4);

%Uncertainty for pressure drop equation (Eq 8.6c from "Introduction to
%Fluid Mechanics by Fox and McDonald)
%
%    delta_P = 12*Q*mu*L/w/H^3

%Propogation errors
dP_dQ = 12*mu_avg*L/W/H^3;
dP_dmu = 12*Q*L/W/H^3;
dP_dL = 12*Q*mu_avg/W/H^3;
dP_dW = -12*Q*mu_avg*L/W^2/H^3;
dP_dH = -36*Q*mu_avg*L/W/H^4;

%Total length measurements error

U_L = sqrt(u_measure^2 + u_L^2);
U_W = sqrt(u_measure^2 + u_W^2);
U_H = sqrt(u_measure^2 + u_H^2);

%Pressure drop uncertainty
U_DP = sqrt((U_Q*dP_dQ)^2 + (U_mu*dP_dmu)^2 + (U_L*dP_dL)^2 +
(U_W*dP_dW)^2 + ...
       (U_H*dP_dH)^2);

%Slip velocity/mean velocity uncertainty
dus_dDPslip = -1/DPnoslip(j);
dus_dDPns = DPslip(j)/DPnoslip(j)^2;
U_usum(j) = sqrt((U_DP*dus_dDPslip)^2 + (U_DP*dus_dDPns)^2);

% Re = rho*Q*Dh/mu/A
dRe_drho = Q*Dh/mu_avg/A;
dRe_dQ = rho_avg*Dh/mu_avg/A;
```

```
dRe_dDh = rho_avg*Q/mu_avg/A;
dRe_dmu = -rho_avg*Q*Dh/mu_avg^2/A;
dRe_dA = -rho_avg*Q*Dh/mu_avg/A^2;
U_Re = sqrt((U_rho*dRe_drho)^2 + (U_Q*dRe_dQ)^2 + (U_Dh*dRe_dDh)^2 +...
    (U_mu*dRe_dmu)^2 + (U_A*dRe_dA)^2);

%Heat transfer coefficient
m_dot = rho_avg*Q;
U_mdot = sqrt((U_rho*Q)^2 + (U_Q*rho_avg)^2);
AA = m_dot*c_avg/per/L;
BB = log((T_out(j) - T_s)/(T_in - T_s));


dh_dmdot = c_avg/per/L*BB;
dh_dc = m_dot/per/L*BB;
dh_dper = -m_dot*c_avg/per^2/L*BB;
dh_dL = -m_dot*c_avg/per/L^2*BB;
dh_dTout = AA*(1/(T_out(j)-T_s));
dh_dTs = AA*((T_in-T_out(j))/((T_in-T_s)*(T_s-T_out(j))));
dh_dTin = AA*(1/(T_s-T_in));

U_Ts = sqrt(u_T^2 + (2*0.51)^2);
U_Tin = sqrt(u_T^2 + (2*0.02)^2);
U_Tout = sqrt(u_T^2 + (2*0.04)^2);

h = AA*BB;
U_h = sqrt((U_mdot*dh_dmdot)^2 + (U_c*dh_dc)^2 + (U_per*dh_dper)^2 +
...
    (U_L*dh_dL)^2 + (U_Tout*dh_dTout)^2 + (U_Ts*dh_dTs)^2 +
(U_Tin*dh_dTin));

%Nusselt number Nu = h*Dh/k
dNu_dh = Dh/k_avg;
dNu_dDh = h/k_avg;
dNu_dk = -h*Dh/k_avg^2;

Nu = -h*Dh/k_avg
U_Nu(j) = sqrt((U_h*dNu_dh)^2 + (U_Dh*dNu_dDh)^2 + (U_k*dNu_dk)^2);

dF_fs = Nu/Nu/DPnoslip(j);
dF_Nuns = DPslip(j)/Nu/DPnoslip(j);
dF_Nus = -DPslip(j)*Nu/Nu^2/DPnoslip(j);
dF_fns = -DPslip(j)*Nu/Nu/DPnoslip(j)^2;
U_F(j) = sqrt((U_DP*dF_fs)^2 + (U_Nu(j)*dF_Nuns)^2 + ...
      (U_Nu(j)*dF_Nus)^2 + (U_DP*dF_fns)^2);

end

U_Q = U_Q_mL
U_usum = U_usum
U_Nu = U_Nu
U_F = U_F
```

References

[1] J. Drelich, E. Chibowski, D. D. Meng and K. Terpilowski, "Hydrophilic and superhydrophilic surfaces and materials," *Soft Matter,* vol. 7, no. 21, pp. 9804-9828, 2011.

[2] J. T. Simpson, S. R. Hunter and T. Aytug, "Superhydrophobic materials and coatings: a review," *Reports on Progress in Physics,* vol. 78, no. 8, p. 086501, 2015.

[3] P. Zhang and F. Y. Lv, "A review of the recent advances in superhydrophobic surfaces and the emerging energy-related applications," *Energy,* vol. 82, pp. 1068-1087, 2015.

[4] A. Balmert, H. F. Bohn, P. Ditsche-Kuru and W. Barthlott, "Dry under water: Comparative morphology and functional aspects of air-retaining insect surfaces," *Journal of Morphology,* vol. 272, no. 4, pp. 442-451, 2011.

[5] W. Barthlott and C. Neinhuis, "Purity of the sacred lotus, or escape from contamination in biological surfaces," *Planta,* vol. 202, no. 1, pp. 1-8, 1997.

[6] E. Bormashenko, Y. Bormashenko, T. Stein, G. Whyman and E. Bormashenko, "Why do pigeon feathers repel water? Hydrophobicity of pennae, Cassie--Baxter wetting hypothesis and Cassie--Wenzel capillarity-induced wetting transition," *Journal of colloid and interface science,* vol. 311, no. 1, pp. 212-216, 2007.

[7] D. Byun, J. Hong, J. H. Ko, Y. J. Lee, H. C. Park, B.-K. Byun, J. R. Lukes and others, "Wetting characteristics of insect wing surfaces," *Journal of Bionic Engineering,* vol. 6, no. 1, pp. 63-70, 2009.

[8] Y. T. Cheng, D. Rodak, C. Wong and C. Hayden, "Effects of micro-and nano-structures on the self-cleaning behaviour of lotus leaves," *Nanotechnology,* vol. 17, no. 5, p. 1359, 2006.

[9] R. Furstner, W. Barthlott, C. Neinhuis and P. Walzel, "Wetting and self-cleaning properties of artificial superhydrophobic surfaces," *Langmuir,* vol. 21, no. 3, pp. 956-961, 2005.

[10] X. Gao and L. Jiang, "Biophysics: water-repellent legs of water striders," *Nature,* vol. 432, no. 7013, pp. 36-36, 2004.

[11] X. Gao, X. Yan, X. Yao, L. Xu, K. Zhang, J. Zhang, B. Yang and L. Jiang, "The dry-style antifogging properties of mosquito compound eyes and artificial analogues prepared by soft lithography," *ADVANCED MATERIALS-DEERFIELD BEACH THEN WEINHEIM-,* vol. 19, no. 17, p. 2213, 2007.

[12] K. Koch, B. Bhushan, Y. C. Jung and W. Barthlott, "Fabrication of artificial Lotus leaves and significance of hierarchical structure for superhydrophobicity and low adhesion," *Soft Matter,* vol. 5, no. 7, pp. 1386-1393, 2009.

[13] Y. Kwon, N. Patankar, J. Choi and J. Lee, "Design of surface hierarchy for extreme hydrophobicity," *Langmuir,* vol. 25, no. 11, pp. 6129-6136, 2009.

[14] X.-M. Li, T. He, M. Crego-Calama and D. N. Reinhoudt, "Conversion of a metastable superhydrophobic surface to an ultraphobic surface," *Langmuir,* vol. 24, no. 15, pp. 8008-8012, 2008.

[15] Y. Liu, X. Chen and J. Xin, "Hydrophobic duck feathers and their simulation on textile substrates for water repellent treatment," *Bioinspiration \& biomimetics,* vol. 3, no. 4, p. 046007, 2008.

[16] C. Neinhuis and W. Barthlott, "Characterization and distribution of water-repellent, self-cleaning plant surfaces," *Annals of Botany,* vol. 79, no. 6, pp. 667-677, 1997.

[17] A. Otten and S. Herminghaus, "How plants keep dry: a physicist's point of view," *Langmuir,* vol. 20, no. 6, pp. 2405-2408, 2004.

[18] A. R. Parker and C. R. Lawrence, "Water capture by a desert beetle," *Nature,* vol. 414, no. 6859, pp. 33-34, 2001.

[19] G. S. Watson, B. W. Cribb and J. A. Watson, "How micro/nanoarchitecture facilitates anti-wetting: an elegant hierarchical design on the termite wing," *ACS nano,* vol. 4, no. 1, pp. 129-136, 2010.

[20] G. S. Watson, B. W. Cribb and J. A. Watson, "The role of micro/nano channel structuring in repelling water on cuticle arrays of the lacewing," *Journal of structural biology,* vol. 171, no. 1, pp. 44-51, 2010.

[21] C.-H. Choi, K. J. A. Westin and K. S. Breuer, "Apparent slip flows in hydrophilic and hydrophobic microchannels," *Physics of Fluids (1994-present),* vol. 15, no. 10, pp. 2897-2902, 2003.

[22] C.-H. Choi and C.-J. Kim, "Large slip of aqueous liquid flow over a nanoengineered superhydrophobic surface," *Physical review letters,* vol. 96, no. 6, p. 066001, 2006.

[23] C. Choi, Y. Yoon, D. Hong, K. S. Brammer, K. Noh, Y. Oh, S. Oh, F. E. Talke and S. Jin, "Strongly superhydrophobic silicon nanowires by supercritical CO2 drying," *Electronic Materials Letters,* vol. 6, no. 2, pp. 59-64, 2010.

[24] R. J. Daniello and J. P. Rothstein, "Turbulent drag reduction using superhydrophobic surfaces," in *APS Division of Fluid Dynamics Meeting Abstracts*, 2008.

[25] S. Gogte, P. Vorobieff, R. Truesdell, A. Mammoli, F. van Swol, P. Shah and C. J. Brinker, "Effective slip on textured superhydrophobic surfaces," *Physics of fluids,* vol. 17, no. 5, pp. 51701-51701, 2005.

[26] P. Joseph, C. Cottin-Bizonne, J.-M. Benoit, C. Ybert, C. Journet, P. Tabeling and L. Bocquet, "Slippage of water past superhydrophobic carbon nanotube forests in microchannels," *Physical review letters,* vol. 97, no. 15, p. 156104, 2006.

[27] C. Lee, C.-H. Choi and others, "Structured surfaces for a giant liquid slip," *Physical review letters,* vol. 101, no. 6, p. 064501, 2008.

[28] C. Lee and C.-J. ". Kim, "Maximizing the giant liquid slip on superhydrophobic microstructures by nanostructuring their sidewalls," *Langmuir,* vol. 25, no. 21, pp. 12812-12818, 2009.

[29] C. Lee and C.-J. ". Kim, "Influence of surface hierarchy of superhydrophobic surfaces on liquid slip," *Langmuir,* vol. 27, no. 7, pp. 4243-4248, 2011.

[30] M. B. Martell, J. B. Perot and J. P. Rothstein, "Direct numerical simulations of turbulent flows over superhydrophobic surfaces," *Journal of Fluid Mechanics,* vol. 620, pp. 31-41, 2009.

[31] M. B. Martell, J. P. Rothstein and J. B. Perot, "An analysis of superhydrophobic turbulent drag reduction mechanisms using direct numerical simulation," *Physics of Fluids (1994-present),* vol. 22, no. 6, p. 065102, 2010.

[32] K. Moaven, M. Rad and M. Taeibi-Rahni, "Experimental investigation of viscous drag reduction of superhydrophobic nano-coating in laminar and turbulent flows," *Experimental Thermal and Fluid Science,* vol. 51, pp. 239-243, 2013.

[33] J. Ou, B. Perot and J. P. Rothstein, "Laminar drag reduction in microchannels using ultrahydrophobic surfaces," *Physics of Fluids (1994-present),* vol. 16, no. 12, pp. 4635-4643, 2004.

[34] J. Ou and J. P. Rothstein, "Direct velocity measurements of the flow past drag-reducing ultrahydrophobic surfaces," *Physics of Fluids (1994-present),* vol. 17, no. 10, p. 103606, 2005.

[35] J. P. Rothstein, "Slip on superhydrophobic surfaces," *Annual Review of Fluid Mechanics,* vol. 42, pp. 89-109, 2010.

[36] R. Truesdell, A. Mammoli, P. Vorobieff, F. van Swol and C. J. Brinker, "Drag reduction on a patterned superhydrophobic surface," *Physical review letters,* vol. 97, no. 4, p. 044504, 2006.

[37] K. Watanabe, T. Takayama, S. Ogata and S. Isozaki, "Flow between two coaxial rotating cylinders with a highly water-repellent wall," *AIChE journal,* vol. 49, no. 8, pp. 1956-1963, 2003.

[38] B. Woolford, D. Maynes and B. Webb, "Liquid flow through microchannels with grooved walls under wetting and superhydrophobic conditions," *Microfluidics and nanofluidics,* vol. 7, no. 1, pp. 121-135, 2009.

[39] B. Woolford, J. Prince, D. Maynes and B. Webb, "Particle image velocimetry characterization of turbulent channel flow with rib patterned superhydrophobic walls," *Physics of Fluids (1994-present),* vol. 21, no. 8, p. 085106, 2009.

[40] A. R. Betz, J. Jenkins, D. Attinger and others, "Boiling heat transfer on superhydrophilic, superhydrophobic, and superbiphilic surfaces," *International Journal of Heat and Mass Transfer,* vol. 57, no. 2, pp. 733-741, 2013.

[41] J. B. Boreyko and C.-H. Chen, "Self-propelled dropwise condensate on superhydrophobic surfaces," *Physical Review Letters,* vol. 103, no. 18, p. 184501, 2009.

[42] C.-H. Chen, Q. Cai, C. Tsai, C.-L. Chen, G. Xiong, Y. Yu and Z. Ren, "Dropwise condensation on superhydrophobic surfaces with two-tier roughness," *Applied Physics Letters,* vol. 90, no. 17, p. 173108, 2007.

[43] R. Chen, M.-C. Lu, V. Srinivasan, Z. Wang, H. H. Cho and A. Majumdar, "Nanowires for enhanced boiling heat transfer," *Nano letters,* vol. 9, no. 2, pp. 548-553, 2009.

[44] X. Chen, R. Ma, J. Li, C. Hao, W. Guo, B. L. Luk, S. C. Li, S. Yao and Z. Wang, "Evaporation of droplets on superhydrophobic surfaces: Surface roughness and small droplet size effects," *Physical review letters,* vol. 109, no. 11, p. 116101, 2012.

[45] J. Cheng, A. Vandadi and C.-L. Chen, "Condensation heat transfer on two-tier superhydrophobic surfaces," *Applied Physics Letters,* vol. 101, no. 13, p. 131909, 2012.

[46] C. Dietz, K. Rykaczewski, A. Fedorov and Y. Joshi, "Visualization of droplet departure on a superhydrophobic surface and implications to heat transfer enhancement during dropwise condensation," *Applied physics letters,* vol. 97, no. 3, p. 033104, 2010.

[47] L.-W. Fan, J.-Q. Li, D.-Y. Li, L. Zhang and Z.-T. Yu, "Regulated transient pool boiling of water during quenching on nanostructured surfaces with modified wettability from superhydrophilic to superhydrophobic," *International Journal of Heat and Mass Transfer,* vol. 76, pp. 81-89, 2014.

[48] H. Gelderblom, A. G. Marin, H. Nair, A. van Houselt, L. Lefferts, J. H. Snoeijer and D. Lohse, "How water droplets evaporate on a superhydrophobic substrate," *Physical Review E,* vol. 83, no. 2, p. 026306, 2011.

[49] C.-C. Hsu and P.-H. Chen, "Surface wettability effects on critical heat flux of boiling heat transfer using nanoparticle coatings," *International Journal of Heat and Mass Transfer,* vol. 55, no. 13, pp. 3713-3719, 2012.

[50] Y. Jung and B. Bhushan, "Wetting behaviour during evaporation and condensation of water microdroplets on superhydrophobic patterned surfaces," *Journal of microscopy,* vol. 229, no. 1, pp. 127-140, 2008.

[51] S. Kulinich and M. Farzaneh, "Effect of contact angle hysteresis on water droplet evaporation from super-hydrophobic surfaces," *Applied Surface Science,* vol. 255, no. 7, pp. 4056-4060, 2009.

[52] N. Miljkovic and E. N. Wang, "Condensation heat transfer on superhydrophobic surfaces," *MRS bulletin,* vol. 38, no. 05, pp. 397-406, 2013.

[53] N. A. Patankar, "Supernucleating surfaces for nucleate boiling and dropwise condensation heat transfer," *Soft Matter,* vol. 6, no. 8, pp. 1613-1620, 2010.

[54] D. H. Shin, S. H. Lee, J.-Y. Jung and J. Y. Yoo, "Evaporating characteristics of sessile droplet on hydrophobic and hydrophilic surfaces," *Microelectronic Engineering,* vol. 86, no. 4, pp. 1350-1353, 2009.

[55] Y. Takata, S. Hidaka and M. Kohno, "Enhanced nucleate boiling by superhydrophobic coating with checkered and spotted patterns," in *Proceedings of the Sixth International Conference on Boiling Heat Transfer. Spoleto. New York: Curran Associates, Inc*, 2006.

[56] X. Zhang, S. Tan, N. Zhao, X. Guo, X. Zhang, Y. Zhang and J. Xu, "Evaporation of sessile water droplets on superhydrophobic natural lotus and biomimetic polymer surfaces," *ChemPhysChem,* vol. 7, no. 10, pp. 2067-2070, 2006.

[57] J. B. Boreyko, C. H. Baker, C. R. Poley and C.-H. Chen, "Wetting and dewetting transitions on hierarchical superhydrophobic surfaces," *Langmuir,* vol. 27, no. 12, pp. 7502-7509, 2011.

[58] J. B. Boreyko and C.-H. Chen, "Vapor chambers with jumping-drop liquid return from superhydrophobic condensers," *International Journal of Heat and Mass Transfer,* vol. 61, pp. 409-418, 2013.

[59] R. Enright, C. Eason, T. Dalton, M. Hodes, T. Salamon, P. Kolodner and T. Krupenkin, "Friction factors and Nusselt numbers in microchannels with superhydrophobic walls," in *ASME 4th International Conference on Nanochannels, Microchannels, and Minichannels*, 2006.

[60] Y. Cheng, J. Xu and Y. Sui, "Numerical study on drag reduction and heat transfer enhancement in microchannels with superhydrophobic surfaces for electronic cooling," *Applied Thermal Engineering,* vol. 88, pp. 71-81, 2015.

[61] A. Cowley, D. Maynes and J. Crockett, "Effective temperature jump length and influence of axial conduction for thermal transport in superhydrophobic channels," *International Journal of Heat and Mass Transfer,* vol. 79, pp. 573-583, 2014.

[62] R. Enright, M. Hodes, T. Salamon and Y. Muzychka, "Isoflux Nusselt number and slip length formulae for superhydrophobic microchannels," *Journal of Heat Transfer,* vol. 136, no. 1, p. 012402, 2014.

[63] D. Maynes, B. Webb and J. Davies, "Thermal transport in a microchannel exhibiting ultrahydrophobic microribs maintained at constant temperature," *Journal of Heat Transfer,* vol. 130, no. 2, p. 022402, 2008.

[64] D. Maynes, B. Webb, J. Crockett and V. Solovjov, "Analysis of laminar slip-flow thermal transport in microchannels with transverse rib and cavity structured superhydrophobic walls at constant heat flux," *Journal of heat transfer,* vol. 135, no. 2, p. 021701, 2013.

[65] D. Maynes and J. Crockett, "Apparent Temperature Jump and Thermal Transport in Channels With Streamwise Rib and Cavity Featured Superhydrophobic Walls at Constant Heat Flux," *Journal of Heat Transfer,* vol. 136, no. 1, p. 011701, 2014.

[66] D. Moreira and P. R. Bandaru, "Thermal transport in laminar flow over superhydrophobic surfaces, utilizing an effective medium approach," *Physics of Fluids (1994-present),* vol. 27, no. 5, p. 052001, 2015.

[67] M. Shojaeian and A. Kocsar, "Convective heat transfer and entropy generation analysis on Newtonian and non-Newtonian fluid flows between parallel-plates under slip boundary conditions," *International Journal of Heat and Mass Transfer,* vol. 70, pp. 664-673, 2013.

[68] K. Gotoh, Y. Nakata, M. Tagawa and M. Tagawa, "Wettability of ultraviolet excimer-exposed PE, PI and PTFE films determined by the contact angle measurements," *Colloids and Surfaces A: Physicochemical and Engineering Aspects,* vol. 224, no. 1, pp. 165-173, 2003.

[69] H. Kamusewitz and W. Possart, "The static contact angle hysteresis obtained by different experiments for the system PTFE/water," *International journal of adhesion and adhesives,* vol. 5, no. 4, pp. 211-215, 1985.

[70] J. D. Miller, S. Veeramasuneni, J. Drelich, M. Yalamanchili and G. Yamauchi, "Effect of roughness as determined by atomic force microscopy on the wetting properties of PTFE thin films," *Polymer Engineering \& Science,* vol. 36, no. 14, pp. 1849-1855, 1996.

[71] K. L. Mittal, Contact angle, wettability and adhesion, vol. 4, CRC Press, 2006.

[72] T. Yasuda, T. Okuno and H. Yasuda, "Contact angle of water on polymer surfaces," *Langmuir,* vol. 10, no. 7, pp. 2435-2439, 1994.

[73] M. Yekta-Fard and A. B. Ponter, "The influences of vapor environment and temperature on the contact angle-drop size relationship," *Journal of colloid and interface science,* vol. 126, no. 1, pp. 134-140, 1988.

[74] J. Zhang, J. Li and Y. Han, "Superhydrophobic PTFE surfaces by extension," *Macromolecular Rapid Communications,* vol. 25, no. 11, pp. 1105-1108, 2004.

[75] A. Cassie and S. Baxter, "Wettability of porous surfaces," *Transactions of the Faraday Society,* vol. 40, pp. 546-551, 1944.

[76] A. Cassie, "Contact angles," *Discussions of the Faraday Society,* vol. 3, pp. 11-16, 1948.

[77] R. N. Wenzel, "Resistance of solid surfaces to wetting by water," *Industrial \& Engineering Chemistry,* vol. 28, no. 8, pp. 988-994, 1936.

[78] R. N. Wenzel, "Surface Roughness and Contact Angle.," *The Journal of Physical Chemistry,* vol. 53, no. 9, pp. 1466-1467, 1949.

[79] J. Bico, U. Thiele and D. Quere, "Wetting of textured surfaces," *Colloids and Surfaces A: Physicochemical and Engineering Aspects,* vol. 206, no. 1, pp. 41-46, 2002.

[80] L. Feng, S. Li, Y. Li, H. Li, L. Zhang, J. Zhai, Y. Song, B. Liu, L. Jiang and D. Zhu, "Super-hydrophobic surfaces: from natural to artificial," *Advanced materials,* vol. 14, no. 24, pp. 1857-1860, 2002.

[81] D. Y. Kwok and A. W. Neumann, "Contact angle measurement and contact angle interpretation," *Advances in colloid and interface science,* vol. 81, no. 3, pp. 167-249, 1999.

[82] D. Li and A. Neumann, "Contact angles on hydrophobic solid surfaces and their interpretation," *Journal of colloid and interface science,* vol. 148, no. 1, pp. 190-200, 1992.

[83] A. Marmur, "Wetting on hydrophobic rough surfaces: to be heterogeneous or not to be?," *Langmuir,* vol. 19, no. 20, pp. 8343-8348, 2003.

[84] N. Shirtcliffe, G. McHale, M. Newton and C. Perry, "Wetting and wetting transitions on copper-based super-hydrophobic surfaces," *Langmuir,* vol. 21, no. 3, pp. 937-943, 2005.

[85] B. Taft, S. Smith and J. Moulton, "Contact Angle Measurements for Advanced Thermal Management Technologies," *Frontiers in Heat and Mass Transfer (FHMT),* vol. 5, no. 1, 2014.

[86] Z. Yoshimitsu, A. Nakajima, T. Watanabe and K. Hashimoto, "Effects of surface structure on the hydrophobicity and sliding behavior of water droplets," *Langmuir,* vol. 18, no. 15, pp. 5818-5822, 2002.

[87] G. Lamour, A. Hamraoui, A. Buvailo, Y. Xing, S. Keuleyan, V. Prakash, A. Eftekhari-Bafrooei and E. Borguet, "Contact angle measurements using a simplified experimental setup," *Journal of chemical education,* vol. 87, no. 12, pp. 1403-1407, 2010.

[88] G. Nellis and S. Klein, Heat Transfer, Cambridge University Press, 2009.

[89] A. D. Williams, P. Vorobieff and A. Mammoli, "Effect of Slip Flow on Heat Transfer: Numerical Analysis," in *50th AIAA aerospace sciences meeting*, 2012.

[90] S. Goldstein, Modern developments in fluid dynamics: an account of theory and experiment relating to boundary layers, turbulent motion and wakes, vol. 1, Clarendon Press, 1938.

[91] D. Bernoulli, Hydrodynamica sive de viribus et motibus fluidorum commentarii, Johann Reinhold Dulsecker, 1738.

[92] D. M. Tolstoi, "Molecular theory for slippage of liquids over solid surfaces (in Russian)," *Doklady Akad Nauk SSSR,* 1952.

[93] T. D. Blake, "Slip between a liquid and a solid: DM Tolstoi's (1952) theory reconsidered," *Colloids and surfaces,* vol. 47, pp. 135-145, 1990.

[94] E. Lauga, M. Brenner and H. Stone, "Microfluidics: the no-slip boundary condition," in *Springer handbook of experimental fluid mechanics*, Springer, 2007, pp. 1219-1240.

[95] E. Schnell, "Slippage of water over nonwettable surfaces," *Journal of Applied Physics,* vol. 27, no. 10, pp. 1149-1152, 1956.

[96] P. A. Thompson and S. M. Troian, "A general boundary condition for liquid flow at solid surfaces," *Nature,* vol. 389, no. 6649, pp. 360-362, 1997.

[97] P. Tabeling, "Slip phenomena at liquid-solid interfaces.," *Comptes Rendus Physique,* vol. 5, no. 5, pp. 531-537, 2004.

[98] E. Muntz, D. Weaver and D. Campbell, Rarefied Gas Dynamics: Theoretical and Computational Techniques, American Institute of Aeronautics and Astronautics, 1989.

[99] M. Gad-el-Hak, "The fluid mechanics of microdevices-the freeman scholar lecture," *Transactions-American Society of Mechanical Engineers Journal of FLUIDS Engineering,* vol. 121, pp. 5-33, 1999.

[100] P.-G. De Gennes, "Wetting: statics and dynamics," *Reviews of modern physics,* vol. 57, no. 3, p. 827, 1985.

[101] E. Dussan, "On the spreading of liquids on solid surfaces: static and dynamic contact lines," *Annual Review of Fluid Mechanics,* vol. 11, no. 1, pp. 371-400, 1979.

[102] P.-G. de Gennes, "On fluid/wall slippage," *Langmuir,* vol. 18, no. 9, pp. 3413-3414, 2002.

[103] C. Cottin-Bizonne, S. Jurine, J. Baudry, J. Crassous, F. Restagno and E. Charlaix, "Nanorheology: an investigation of the boundary condition at hydrophobic and hydrophilic interfaces," *The European Physical Journal E,* vol. 9, no. 1, pp. 47-53, 2002.

[104] J. Israelachvili and D. Tabor, "The measurement of van der Waals dispersion forces in the range 1.5 to 130 nm," in *Proceedings of the Royal Society of London A: Mathematical, Physical and Engineering Sciences*, 1972.

[105] Y. Zhu and S. Granick, "Rate-dependent slip of Newtonian liquid at smooth surfaces," *Physical review letters,* vol. 87, no. 9, p. 096105, 2001.

[106] Y. Zhu and S. Granick, "Limits of the hydrodynamic no-slip boundary condition," *Physical review letters,* vol. 88, no. 10, p. 106102, 2002.

[107] J.-H. J. Cho, B. M. Law and F. Rieutord, "Dipole-dependent slip of Newtonian liquids at smooth solid hydrophobic surfaces," *Physical review letters,* vol. 92, no. 16, p. 166102, 2004.

[108] C. Henry, C. Neto, D. Evans, S. Biggs and V. Craig, "The effect of surfactant adsorption on liquid boundary slippage," *Physica A: Statistical Mechanics and its Applications,* vol. 339, no. 1, pp. 60-65, 2004.

[109] U.-C. Boehnke, T. Remmler, H. Motschmann, S. Wurlitzer, J. Hauwede and T. M. Fischer, "Partial air wetting on solvophobic surfaces in polar liquids," *Journal of colloid and interface science,* vol. 211, no. 2, pp. 243-251, 1999.

[110] N. Churaev, J. Ralston, I. Sergeeva and V. Sobolev, "Electrokinetic properties of methylated quartz capillaries," *Advances in colloid and interface science,* vol. 96, no. 1, pp. 265-278, 2002.

[111] P. Joseph and P. Tabeling, "Direct measurement of the apparent slip length," *Physical Review E,* vol. 71, no. 3, p. 035303, 2005.

[112] D. C. Tretheway and C. D. Meinhart, "Apparent fluid slip at hydrophobic microchannel walls," *Physics of Fluids (1994-present),* vol. 14, no. 3, pp. L9--L12, 2002.

[113] D. C. Tretheway and C. D. Meinhart, "A generating mechanism for apparent fluid slip in hydrophobic microchannels," *Physics of Fluids (1994-present),* vol. 16, no. 5, pp. 1509-1515, 2004.

[114] H. Hervet and L. Leger, "Flow with slip at the wall: from simple to complex fluids," *Comptes rendus physique,* vol. 4, no. 2, pp. 241-249, 2003.

[115] R. Pit, H. Hervet and L. L{\'e}ger, "Friction and slip of a simple liquid at a solid surface," *Tribology letters,* vol. 7, no. 2-3, pp. 147-152, 1999.

[116] R. Pit, H. Hervet and L. Leger, "Direct experimental evidence of slip in hexadecane: solid interfaces," *Physical review letters,* vol. 85, no. 5, p. 980, 2000.

[117] D. Lumma, A. Best, A. Gansen, F. Feuillebois, J. Radler and O. Vinogradova, "Flow profile near a wall measured by double-focus fluorescence cross-correlation," *Physical Review E,* vol. 67, no. 5, p. 056313, 2003.

[118] E. Bonaccurso, H.-J. Butt and V. S. Craig, "Surface roughness and hydrodynamic boundary slip of a Newtonian fluid in a completely wetting system," *Physical review letters,* vol. 90, no. 14, p. 144501, 2003.

[119] V. S. Craig, C. Neto and D. R. Williams, "Shear-dependent boundary slip in an aqueous Newtonian liquid," *Physical review letters,* vol. 87, no. 5, p. 054504, 2001.

[120] C. Neto, V. Craig and D. Williams, "Evidence of shear-dependent boundary slip in Newtonian liquids," *The European Physical Journal E,* vol. 12, no. 1, pp. 71-74, 2003.

[121] G. Nagayama and P. Cheng, "Effects of interface wettability on microscale flow by molecular dynamics simulation," *International Journal of Heat and Mass Transfer,* vol. 47, no. 3, pp. 501-513, 2004.

[122] N. V. Priezjev and S. M. Troian, "Molecular origian and dynamic behavior of slip in sheared polymer films," *Physical Review Letters,* vol. 92, no. 1, p. 018302, 2004.

[123] H. Wu and P. Cheng, "An experimental study of convective heat transfer in silicon microchannels with different surface conditions," *International Journal of Heat and Mass Transfer,* vol. 46, no. 14, pp. 2547-2556, 2003.

[124] U.-C. Boehnke, T. Remmler, H. Motschmann, S. Wurlitzer, J. Hauwede and T. M. Fischer, "Partial air wetting on solvophobic surfaces in polar liquids," *Journal of colloid and interface science,* vol. 211, no. 2, pp. 243-251, 1999.

[125] C. Cottin-Bizonne, B. Cross, A. Steinberger and E. Charlaix, "Boundary slip on smooth hydrophobic surfaces: Intrinsic effects and possible artifacts," *Physical review letters,* vol. 94, no. 5, p. 056102, 2005.

[126] D. Tretheway, S. Stone and C. Meinhart, "Effects of Absolute Pressure and Dissolved Gasses on Apparent Fluid Slip in Hydrophobic Microchannels," in *APS Division of Fluid Dynamics Meeting Abstracts*, 2004.

[127] Z. Lin and S. Granick, "Platinum nanoparticles at mica surfaces," *Langmuir,* vol. 19, no. 17, pp. 7061-7070, 2003.

[128] E. Ruckenstein and P. Rajora, "On the no-slip boundary condition of hydrodynamics," *Journal of colloid and interface science,* vol. 96, no. 2, pp. 488-491, 1983.

[129] K. Lum, D. Chandler and J. D. Weeks, "Hydrophobicity at small and large length scales," *The Journal of Physical Chemistry B,* vol. 103, no. 22, pp. 4570-4577, 1999.

[130] K. Jeffs, D. Maynes and B. W. Webb, "Prediction of turbulent channel flow with superhydrophobic walls consisting of micro-ribs and cavities oriented parallel to the flow direction," *International Journal of Heat and Mass Transfer,* vol. 53, no. 4, pp. 786-796, 2010.

[131] P.-G. De Gennes, F. Brochard-Wyart and D. Quere, Capillarity and wetting phenomena: drops, bubbles, pearls, waves, Springer Science \& Business Media, 2013.

[132] J.-L. Barrat and L. Bocquet, "Large slip effect at a nonwetting fluid-solid interface," *Physical review letters,* vol. 82, no. 23, p. 4671, 1999.

[133] Y. Yuan and T. R. Lee, "Contact angle and wetting properties," in *Surface science techniques*, Springer, 2013, pp. 3-34.

[134] J. H. Snoeijer and B. Andreotti, "A microscopic view on contact angle selection," *Physics of Fluids (1994-present),* vol. 20, no. 5, p. 057101, 2008.

[135] T. Young, "An essay on the cohesion of fluids," *Philosophical Transactions of the Royal Society of London,* vol. 95, pp. 65-87, 1805.

[136] D. Quere, "Non-sticking drops," *Reports on Progress in Physics,* vol. 68, no. 11, p. 2495, 2005.

[137] J. B. Boreyko, "From Dynamical Superhydrophobicity to Thermal Diodes," 2012.

[138] C. Marangoni, "Study on surface tension of fluid," *Boletim da Divisao Nacional de Dermatologia Sanitaria,* 1871.

[139] E. G. Shafrin and W. A. Zisman, "Contact angle, wettability and adhesion," *Advances in Chemistry Series,* vol. 43, pp. 145-157, 1964.

[140] N. Selvakumar, H. C. Barshilia, M. Ramesh and K. Rajam, "Effect of substrate roughness on the contact angle of sputter deposited superhydrophobic polytetrafluoroethylene coatings," 2010.

[141] S. S. Latthe, C. Terashima, K. Nakata and A. Fujishima, "Superhydrophobic surfaces developed by mimicking hierarchical surface morphology of lotus leaf," *Molecules,* vol. 19, no. 4, pp. 4256-4283, 2014.

[142] D. Quere, A. Lafuma and J. Bico, "Slippy and sticky microtextured solids," *Nanotechnology,* vol. 14, no. 10, p. 1109, 2003.

[143] J. Bico, C. Marzolin and D. Quere, "Pearl drops," *EPL (Europhysics Letters),* vol. 47, no. 2, p. 220, 1999.

[144] J. Bico, C. Tordeux and D. Quere, "Rough wetting," *EPL (Europhysics Letters),* vol. 55, no. 2, p. 214, 2001.

[145] D. Quere, "Rough ideas on wetting," *Physica A: Statistical Mechanics and its Applications,* vol. 313, no. 1, pp. 32-46, 2002.

[146] E. Lauga and H. A. Stone, "Effective slip in pressure-driven Stokes flow," *Journal of Fluid Mechanics,* vol. 489, pp. 55-77, 2003.

[147] B. He, N. A. Patankar and J. Lee, "Multiple equilibrium droplet shapes and design criterion for rough hydrophobic surfaces," *Langmuir,* vol. 19, no. 12, pp. 4999-5003, 2003.

[148] C. Ishino, K. Okumura and D. Quere, "Wetting transitions on rough surfaces," *EPL (Europhysics Letters),* vol. 68, no. 3, p. 419, 2004.

[149] T.-G. Cha, J. W. Yi, M.-W. Moon, K.-R. Lee and H.-Y. Kim, "Nanoscale patterning of microtextured surfaces to control superhydrophobic robustness," *Langmuir,* vol. 26, no. 11, pp. 8319-8326, 2010.

[150] D. Oner and T. J. McCarthy, "Ultrahydrophobic surfaces. Effects of topography length scales on wettability," *Langmuir,* vol. 16, no. 20, pp. 7777-7782, 2000.

[151] C. Furmidge, "Studies at phase interfaces I: The sliding of liquid drops on solid surfaces and a theory of spray retention," *Journal of Colloid Science,* vol. 17, no. 4, pp. 309-324, 1962.

[152] R. Johnson and R. Dettre, "Contact angle hysteresis. I. Study of an idealized rough surface," *Adv. Chem. Ser,* vol. 43, no. 112, pp. 1964-65, 1964.

[153] J. R. Philip, "Integral properties of flows satisfying mixed no-slip and no-shear conditions," *Zeitschrift f{\"u}r angewandte Mathematik und Physik ZAMP,* vol. 23, no. 6, pp. 960-968, 1972.

[154] C.-H. Choi, U. Ulmanella, J. Kim, C.-M. Ho and C.-J. Kim, "Effective slip and friction reduction in nanograted superhydrophobic microchannels," *Physics of Fluids (1994-present),* vol. 18, no. 8, p. 087105, 2006.

[155] A. K. Balasubramanian, A. C. Miller and O. K. Rediniotis, "Microstructured hydrophobic skin for hydrodynamic drag reduction," *AIAA journal,* vol. 42, no. 2, pp. 411-414, 2004.

[156] R. J. Daniello, N. E. Waterhouse and J. P. Rothstein, "Drag reduction in turbulent flows over superhydrophobic surfaces," *Physics of Fluids (1994-present),* vol. 21, no. 8, p. 085103, 2009.

[157] E. Aljallis, M. A. Sarshar, R. Datla, V. Sikka, A. Jones and C.-H. Choi, "Experimental study of skin friction drag reduction on superhydrophobic flat plates in high Reynolds number boundary layer flow," *Physics of Fluids (1994-present),* vol. 25, no. 2, p. 025103, 2013.

[158] G. Rosengarten, J. Cooper-White and G. Metcalfe, "Experimental and analytical study of the effect of contact angle on liquid convective heat transfer in microchannels," *International journal of heat and mass transfer,* vol. 49, no. 21, pp. 4161-4170, 2006.

[159] M. J. Martin and I. D. Boyd, "Momentum and heat transfer in a laminar boundary layer with slip flow," *Journal of Thermophysics and Heat Transfer,* vol. 20, no. 4, pp. 710-719, 2006.

[160] T. N. Vezirouglu and S. Chandra, Thermal conductance of two-dimensional constrictions, Mechanical Engineering Department, University of Miami, 1968.

[161] J. R. Philip, "Flows satisfying mixed no-slip and no-shear conditions," *Zeitschrift für angewandte Mathematik und Physik ZAMP,* vol. 23, no. 3, pp. 353-372, 1971.

[162] C. J. Teo and B. C. Khoo, "Analysis of Stokes flow in microchannels with superhydrophobic surfaces containing a periodic array of micro-grooves," *Microfluidics and nanofluidics,* vol. 7, no. 3, pp. 353-382, 2009.

[163] L. Steigerwalt-Lam, C. Melnick, M. Hodes, G. Ziskind and R. Enright, "Nusselt numbers for thermally developing Couette," *Journal of Heat Transfer,* vol. 136, no. 5, p. 051703, 2014.

[164] Y. Cheng, C. Teo and B. Khoo, "Microchannel flows with superhydrophobic surfaces: Effects of Reynolds number and pattern width to channel height ratio," *Physics of Fluids (1994-present),* vol. 21, no. 12, p. 122004, 2009.

[165] E. Sparrow and S. Lin, "Laminar heat transfer in tubes under slip-flow conditions," *Journal of Heat Transfer,* vol. 84, no. 4, pp. 363-369, 1962.

[166] J. Sestak and F. Rieger, "Laminar heat transfer to a steady couette flow between parallel plates," *International Journal of Heat and Mass Transfer,* vol. 12, no. 1, pp. 71-80, 1969.

[167] S.-S. Hsieh and C.-Y. Lin, "Convective heat transfer in liquid microchannels with hydrophobic and hydrophilic surfaces," *International Journal of Heat and Mass Transfer,* vol. 52, no. 1, pp. 260-270, 2009.

[168] R. Truesdell, "Modification of the Non-slip Boudnary Condition by Superhydrophobic Wall Patterning," 2006.

[169] S. Prakash, C. Brinker, A. Hurd, S. Rao and others, "Silica Aerogel Films Prepared at Ambient-Pressure by Using Surface Derivatization to Induce Reversible Drying Shrinkage (Vol 374, Pg 439, 1995)," *Nature,* vol. 375, no. 6530, pp. 431-431, 1995.

[170] W. Bigelow, D. Pickett and W. Zisman, "Oleophobic monolayers: I. Films adsorbed from solution in non-polar liquids," *Journal of Colloid Science,* vol. 1, no. 6, pp. 513-538, 1946.

[171] R. W. Smithwich, "Contact-angle studies of microscopic mercury droplets on glass," *Journal of colloid and interface science,* vol. 123, no. 2, pp. 482-485, 1988.

[172] A. Sklodowska, M. Wozniak and R. Matlakowska, "The method of contact angle measurements and estimation of work of adhesion in bioleaching of metals," *Biological procedures online,* vol. 1, no. 3, pp. 114-121, 1999.

[173] S. Brandon, N. Haimovich, E. Yeger and A. Marmur, "Partial wetting of chemically patterned surfaces: The effect of drop size," *Journal of colloid and interface science,* vol. 263, no. 1, pp. 237-243, 2003.

[174] R. J. Hunter, Foundations of colloid science, C. 6, Ed., Oxford University Press, 2001.

[175] A. Neumann, R. Good, R. Good and R. Stromberg, "Surface and Colloid Science," *Vol. 11Plenum, New York,* pp. 31-91, 1979.

[176] W. Fenrick, "Simple Tangentometer," 1964.

[177] I. Langmuir and V. J. Schaefer, "The effect of dissolved salts on insoluble monolayers," *Journal of the American Chemical Society,* vol. 59, no. 11, pp. 2400-2414, 1937.

[178] M. Phillips and A. Riddiford, "Dynamic contact angles. II. Velocity and relaxation effects for various liquids," *Journal of Colloid and Interface Science,* vol. 41, no. 1, pp. 77-85, 1972.

[179] K. Johnson and D. Shah, "Effect of oil chain length and electrolytes on water solubilization in alcohol-free pharmaceutical microemulsions," *Journal of colloid and interface science,* vol. 107, no. 1, pp. 269-271, 1985.

[180] J. Drelich, J. D. Miller and R. J. Good, "The effect of drop (bubble) size on advancing and receding contact angles for heterogeneous and rough solid surfaces as observed with sessile-drop and captive-bubble techniques," *Journal of Colloid and Interface Science,* vol. 179, no. 1, pp. 37-50, 1996.

[181] W. Zhang and B. Hallstr{\"o}m, "Membrane characterization using the contact angle technique I. Methodology of the captive bubble technique," *Desalination,* vol. 79, no. 1, pp. 1-12, 1990.

[182] W. Zhang, M. Wahlgren and B. Sivik, "Membrane characterization by the contact angle technique: II. Characterization of UF-membranes and comparison between the captive bubble and sessile drop as methods to obtain water contact angles," *Desalination,* vol. 72, no. 3, pp. 263-273, 1989.

[183] N. K. Adam and G. Jessop, "CCL - Angles of contact polarity of solid surfaces," *Journal of the Chemical Society Transactions,* vol. 127, pp. 1863-1868 , 1925.

[184] F. M. Fowkes and W. D. Harkins, "The state of monolayers adsorbed at the interface solid—aqueous solution," *Journal of the American Chemical Society,* vol. 62, no. 12, pp. 3377-3386, 1940.

[185] L. M. Lander, L. M. Siewierski, W. J. Brittain and E. A. Vogler, "A systematic comparison of contact angle methods," *Langmuir,* vol. 9, no. 8, pp. 2237-2239, 1993.

[186] B. Bezuglyi, O. Tarasov and A. Fedorets, "Modified tilting-plate method for measuring contact angles," *Colloid Journal,* vol. 63, no. 6, pp. 668-674, 2001.

[187] G. T. Smedley and D. E. Coles, "A refractive tilting-plate technique for measurement of dynamic contact angles," *Journal of colloid and interface science,* vol. 286, no. 1, pp. 310-318, 2005.

[188] F. Restagno, C. Poulard, C. Cohen, L. Vagharchakian and L. Leger, "Contact angle and contact angle hysteresis measurements using the capillary bridge technique," *Langmuir,* vol. 25, no. 18, pp. 11188-11196, 2009.

[189] L. Vagharchakian, F. Restagno and L. Leger, "Capillary Bridge Formation and Breakage: A Test to Characterize Antiadhesive Surfaces†," *The Journal of Physical Chemistry B,* vol. 113, no. 12, pp. 3769-3775, 2008.

[190] C. Cohen, F. Restagno, C. Poulard and L. Leger, "Wetting and dewetting transition: an efficient toolbox for characterizing low-energy surfaces," *Langmuir,* vol. 26, no. 19, pp. 15345-15349, 2010.

[191] R. Rioboo, M. Voue, H. Adao, J. Conti, A. Vaillant, D. Seveno and J. De Coninck, "Drop impact on soft surfaces: beyond the static contact angles," *Langmuir,* vol. 26, no. 7, pp. 4873-4879, 2009.

[192] L. Wilhelmy, "Ueber die Abhangigkeit der Capillaritats-Constanten des Alkohols von Substanz und Gestalt des benetzten festen Korpers," *Annalen der Physik,* vol. 195, no. 6, pp. 177-217, 1863.

[193] A. J. Milling, Surface characterization methods: principles, techniques, and applications, vol. 87, CRC Press, 1999.

[194] D. Kwok, D. Li and A. Neumann, "Capillary rise at a vertical plate as a contact angle technique," *Surfactant science series,* pp. 413-440, 1996.

[195] M. Shimokawa and T. Takamura, "Relation between interfacial tension and capillary liquid rise on polished metal electrodes," *Journal of Electroanalytical Chemistry and Interfacial Electrochemistry,* vol. 41, no. 3, pp. 359-366, 1973.

[196] C. Budziak and A. Neumann, "Automation of the capillary rise technique for measuring contact angles," *Colloids and surfaces,* vol. 43, no. 2, pp. 279-293, 1990.

[197] D. Kwok, C. Budziak and A. Neumann, "Measurements of static and low rate dynamic contact angles by means of an automated capillary rise technique," *Journal of colloid and interface science,* vol. 173, no. 1, pp. 143-150, 1995.

[198] D. Jordan and J. Lane, "A thermodynamic discussion of the use of a vertical-plate balance for the measurement of surface tension," *Australian Journal of Chemistry,* vol. 17, no. 1, pp. 7-15, 1964.

[199] F. Bashforth and J. Adams, An Attempt to Test the Theory of Capillary Action, London: Cambridge, 1892.

[200] B. E. Blaisdell, "The Physical Properties of Fluid Interfaces of Large Radius of Curvature. I. Integration of LaPlace's Equation for the Equilibrium Meridian of a Fluid Drop of Axial Symmetry in a Gravitational Field. Numerical Integration and Tables for Sessile Drops of Moderately Large Size," *Journal of Mathematics and Physics,* vol. 19, no. 1, pp. 186-216, 1940.

[201] N. Tawde and K. Parvatikar, "Unstable pendant drops in relation to drop-weight method of surface tension.," *Current science,* vol. 19, no. 5, p. 147, 1950.

[202] O. Mills, "Tables for use in the measurement of interfacial tensions between liquids with small density differences," *British Journal of Applied Physics,* vol. 4, no. 8, p. 247, 1953.

[203] P. Cheng, D. Li, L. Boruvka, Y. Rotenberg and A. Neumann, "Automation of axisymmetric drop shape analysis for measurements of interfacial tensions and contact angles," *Colloids and Surfaces,* vol. 43, no. 2, pp. 151-167, 1990.

[204] O. Del Rio and A. Neumann, "Axisymmetric drop shape analysis: computational methods for the measurement of interfacial properties from the shape and dimensions of pendant and sessile drops," *Journal of colloid and interface science,* vol. 196, no. 2, pp. 136-147, 1997.

[205] Y. Rotenberg, L. Boruvka and A. Neumann, "Determination of surface tension and contact angle from the shapes of axisymmetric fluid interfaces," *Journal of colloid and interface science,* vol. 93, no. 1, pp. 169-183, 1983.

[206] R. O. Duda, P. E. Hart and others, Pattern classification and scene analysis, vol. 3, C. 6, Ed., Wiley New York, 1973.

[207] F. Skinner, Y. Rotenberg and A. Neumann, "Contact angle measurements from the contact diameter of sessile drops by means of a modified axisymmetric drop shape analysis," *Journal of Colloid and Interface Science,* vol. 130, no. 1, pp. 25-34, 1989.

[208] E. Moy, P. Cheng, Z. Policova, S. Treppo, D. Kwok, D. Mack, P. Sherman and A. Neuman, "Measurement of contact angles from the maximum diameter of non-wetting drops by means of a modified axisymmetric drop shape analysis," *Colloids and surfaces,* vol. 58, no. 3, pp. 215-227, 1991.

[209] M. Cabezas, A. Bateni, J. Montanero and A. Neumann, "A new drop-shape methodology for surface tension measurement," *Applied surface science,* vol. 238, no. 1, pp. 480-484, 2004.

[210] M. Cabezas, A. Bateni, J. Montanero and A. Neumann, "A new method of image processing in the analysis of axisymmetric drop shapes," *Colloids and Surfaces A: Physicochemical and Engineering Aspects,* vol. 255, no. 1, pp. 193-200, 2005.

[211] M. G. Cabezas, A. Bateni, J. M. Montanero and A. W. Neumann, "Determination of surface tension and contact angle from the shapes of axisymmetric fluid

interfaces without use of apex coordinates," *Langmuir,* vol. 22, no. 24, pp. 10053-10060, 2006.

[212] A. Kalantarian, R. David and A. Neumann, "Methodology for High Accuracy Contact Angle Measurement†," *Langmuir,* vol. 25, no. 24, pp. 14146-14154, 2009.

[213] A. F. Stalder, T. Melchior, M. Muller, D. Sage, T. Blu and M. Unser, "Low-bond axisymmetric drop shape analysis for surface tension and contact angle measurements of sessile drops," *Colloids and Surfaces A: Physicochemical and Engineering Aspects,* vol. 364, no. 1, pp. 72-81, 2010.

[214] M. Yekta-Fard and A. Ponter, "Surface treatment and its influence on contact angles of water drops residing on teflon and copper," *The Journal of Adhesion,* vol. 18, no. 3, pp. 197-205, 1985.

[215] C. Extrand, "Contact angles and hysteresis on surfaces with chemically heterogeneous islands," *Langmuir,* vol. 19, no. 9, pp. 3793-3796, 2003.

[216] M. Shoji and X. Z. Yi, "Study of Contact Angle Hysteresis. In Relation to Boiling Surface Wettability," *JSME International Journal Series B Fluids and Thermal Engineering,* vol. 37, no. 3, pp. 560-567, 1994.

[217] G. Li, B. Wang, Y. Liu, T. Tan, X. Song, E. Li and H. Yan, "Stable superhydrophobic surface: fabrication of interstitial cottonlike structure of copper nanocrystals by magnetron sputtering," *Science and Technology of Advanced Materials,* vol. 9, 2008.

[218] G. Macdougall and C. Ockrent, "Surface energy relations in liquid/solid systems. I. The adhesion of liquids to solids and a new method of determining the surface tension of liquids," in *Proceedings of the Royal Society of London A: Mathematical, Physical and Engineering Sciences*, 1942.

[219] C. Extrand and Y. Kumagai, "Contact angles and hysteresis on soft surfaces," *Journal of colloid and interface science,* vol. 184, no. 1, pp. 191-200, 1996.

[220] C. Extrand and Y. Kumagai, "An experimental study of contact angle hysteresis," *Journal of Colloid and interface Science,* vol. 191, no. 2, pp. 378-383, 1997.

[221] S.-H. Xu, C.-X. Wang, Z.-W. Sun and W.-R. Hu, "The influence of contact line velocity and acceleration on the dynamic contact angle: An experimental study in microgravity," *International Journal of Heat and Mass Transfer,* vol. 54, no. 9, pp. 2222-2225, 2011.

[222] R. Tadmor, "Line energy and the relation between advancing, receding, and young contact angles," *Langmuir,* vol. 20, no. 18, pp. 7659-7664, 2004.

[223] W. Zisman, "Contact Angle, Wettability and Adhesion, ACS Advances in Chemistry Series," *Relation of the equilibrium contact angle to liquid and solid construction,* 1964.

[224] C. Ybert, C. Barentin, C. Cottin-Bizonne, P. Joseph and L. Bocquet, "Achieving large slip with superhydrophobic surfaces: Scaling laws for generic geometries," *Physics of Fluids (1994-present),* vol. 19, no. 12, p. 123601, 2007.

[225] R. S. Voronov, D. V. Papavassiliou and L. L. Lee, "Review of fluid slip over superhydrophobic surfaces and its dependence on the contact angle," *Industrial \& Engineering Chemistry Research,* vol. 47, no. 8, pp. 2455-2477, 2008.

[226] W. B. Russel, D. A. Saville and W. R. Schowalter, Colloidal dispersions, Cambridge university press, 1992.

[227] S. J. Pogorzelski, Z. Berezowski, P. Rochowski and J. Szurkowski, "A novel methodology based on contact angle hysteresis approach for surface changes monitoring in model PMMA-Corega Tabs system," *Applied Surface Science,* vol. 258, no. 8, pp. 3652-3658, 2012.

[228] N. A. Patankar, "Transition between superhydrophobic states on rough surfaces," *Langmuir,* vol. 20, no. 17, pp. 7097-7102, 2004.

[229] N. A. Patankar, "On the modeling of hydrophobic contact angles on rough surfaces," *Langmuir,* vol. 19, no. 4, pp. 1249-1253, 2003.

[230] D. E. McIntyre, "A study of dynamic wettability on a hydrophobic surface," 1969.

[231] C. Maze and G. Burnet, "Modifications of a non-linear regression technique used to calculate surface tension from sessile drops," *Surface Science,* vol. 24, no. 1, pp. 335-342, 1971.

[232] C. Maze and G. Burnet, "A non-linear regression method for calculating surface tension and contact angle from the shape of a sessile drop," *Surface Science,* vol. 13, no. 2, pp. 451-470, 1969.

[233] A. Marmur, "The lotus effect: superhydrophobicity and metastability," *Langmuir,* vol. 20, no. 9, pp. 3517-3519, 2004.

[234] J. Malcolm and H. Paynter, "Simultaneous determination of contact angle and interfacial tension from sessile drop measurements," *Journal of Colloid and Interface Science,* vol. 82, no. 2, pp. 269-275, 1981.

[235] K. K. Lau, J. Bico, K. B. Teo, M. Chhowalla, G. A. Amaratunga, W. I. Milne, G. H. McKinley and K. K. Gleason, "Superhydrophobic carbon nanotube forests," *Nano Letters,* vol. 3, no. 12, pp. 1701-1705, 2003.

[236] I. A. Larmour, S. E. Bell and G. C. Saunders, "Remarkably simple fabrication of superhydrophobic surfaces using electroless galvanic deposition," *Angewandte Chemie,* vol. 119, no. 10, pp. 1740-1742, 2007.

[237] A. Lafuma and D. Quere, "Superhydrophobic states," *Nature materials,* vol. 2, no. 7, pp. 457-460, 2003.

[238] D. Kwok, R. Lin, M. Mui and A. Neumann, "Low-rate dynamic and static contact angles and the determination of solid surface tensions," *Colloids and Surfaces A: Physicochemical and Engineering Aspects,* vol. 116, no. 1, pp. 63-77, 1996.

[239] H. E. Jeong, S. H. Lee, J. K. Kim and K. Y. Suh, "Nanoengineered multiscale hierarchical structures with tailored wetting properties," *Langmuir,* vol. 22, no. 4, pp. 1640-1645, 2006.

[240] H.-J. Hwang and S. Simon Song, "The effects of grooves on the flow rate in a microchannel," *Biochip J,* vol. 2, pp. 123-126, 2008.

[241] C. Huh and R. Reed, "A method for estimating interfacial tensions and contact angles from sessile and pendant drop shapes," *Journal of Colloid and Interface Science,* vol. 91, no. 2, pp. 472-484, 1983.

[242] B. He, J. Lee and N. A. Patankar, "Contact angle hysteresis on rough hydrophobic surfaces," *Colloids and Surfaces A: Physicochemical and Engineering Aspects,* vol. 248, no. 1, pp. 101-104, 2004.

[243] K. Hay, M. Dragila and J. Liburdy, "Theoretical model for the wetting of a rough surface," *Journal of colloid and interface science,* vol. 325, no. 2, pp. 472-477, 2008.

[244] S. Hartland and R. W. Hartley, Axisymmetric fluid-liquid interfaces: tables giving the shape of sessile and pendant drops and external menisci, with examples of their use, C. 6, Ed., Elsevier Scientific Publishing Company, 1976.

[245] L. Gao and T. J. McCarthy, "How Wenzel and Cassie were wrong," *Langmuir,* vol. 23, no. 7, pp. 3762-3765, 2007.

[246] A. Gajewski, "Contact angle and sessile drop diameter hysteresis on metal surfaces," *International Journal of Heat and Mass Transfer,* vol. 51, no. 19, pp. 4628-4636, 2008.

[247] F. Fowkes, W. Zisman, A. C. S. D. of Colloid and S. Chemistry, Contact angle, wettability and adhesion: the Kendall award symposium honoring William A. Zisman, Los Angeles, Calif., April 2-3, 1963, American Chemical Society, 1964.

[248] T. Fort and H. Patterson, "A simple method for measuring solid-liquid contact angles," *Journal of colloid science,* vol. 18, no. 3, pp. 217-222, 1963.

[249] L. R. Fisher and J. N. Israelachvili, "Experimental studies on the applicability of the Kelvin equation to highly curved concave menisci," *Journal of colloid and Interface Science,* vol. 80, no. 2, pp. 528-541, 1981.

[250] A. Dupuis and J. Yeomans, "Modeling droplets on superhydrophobic surfaces: equilibrium states and transitions," *Langmuir,* vol. 21, no. 6, pp. 2624-2629, 2005.

[251] O. del Rio, "On the generalization of axisymmetric drop shape analysis, University of Toronto, MA Sc," 1993.

[252] R. Daniello, P. Muralidhar, N. Carron, M. Greene and J. P. Rothstein, "Influence of slip on vortex-induced motion of a superhydrophobic cylinder," *Journal of Fluids and Structures,* vol. 42, pp. 358-368, 2013.

[253] P. W. P. Cheng, "Automation of axisymmetric drop shape analysis using digital image processing," 1990.

[254] J. Boyce, S. Schurch, Y. Rotenberg and A. Neumann, "The measurement of surface and interfacial tension by the axisymmetric drop technique," *Colloids and surfaces,* vol. 9, no. 4, pp. 307-317, 1984.

[255] J. B. Boreyko, Y. Zhao and C.-H. Chen, "Planar jumping-drop thermal diodes," *Applied Physics Letters,* vol. 99, no. 23, p. 234105, 2011.

[256] M. S. Bobji, S. V. Kumar, A. Asthana and R. N. Govardhan, "Underwater sustainability of the “Cassie” state of wetting," *Langmuir,* vol. 25, no. 20, pp. 12120-12126, 2009.

[257] S. Anastasiadis, J. Chen, J. Koberstein, A. Siegel, J. Sohn and J. Emerson, "The determination of interfacial tension by video image processing of pendant fluid drops," *Journal of colloid and interface science,* vol. 119, no. 1, pp. 55-66, 1987.

[258] W. Albring, "GK Batchelor, An Introduction to Fluid Dynamics. XVIII+ 615 S. m. Fig. Cambridge 1967. University Press. Preis geb. 75 s. net," *ZAMM-Journal of Applied Mathematics and Mechanics/Zeitschrift f{\"u}r Angewandte Mathematik und Mechanik,* vol. 48, no. 4, pp. 292-292, 1968.

[259] G. LI, B. Wang, Y. Liu, T. Tan, X. Song, E. Li and H. Yan, "Stable superhydrophobic surface: fabrication of interstitial cottonlike structure of copper nanocrystals by magnetron sputtering," *Science and Technology of Advanced Materials,* vol. 9, pp. 1-6, 2008.